Atomically-thin Al_2O_3 dielectric films for metal-insulator-metal tunnel junctions

By

Jamie S. Wilt

Submitted to the graduate degree program in Physics and the Graduate Faculty of the University of Kansas in partial fulfillment of the requirements for the degree of Doctor of Philosophy

Chairperson: Dr. Judy Wu

Dr. Cindy Berrie

Dr. Wai-Lun Chan

Dr. Siyuan Han

Dr. Stephen Sanders

Date Defended: November 20th, 2017

The Dissertation Committee for Jamie Wilt

certifies that this is the approved version of the following dissertation:

Atomically-thin Al_2O_3 dielectric films for metal-insulator-metal tunnel junctions

Chairperson: Dr. Judy Wu

Date Approved: November 20th, 2017

Abstract

Metal-Insulator-Metal tunnel junctions (MIMTJ) are a core building block for a variety of microelectronics including Magnetic Tunnel Junctions (MTJs) for magnetic memory and Josephson Junctions (JJs) for quantum computers. The performance of MIMTJ devices critically depends on the insulator which should have few defects and an atomic-scale thickness. However, the current state of the art insulators are both high-defect and atomic-scale (thermal or plasma assisted AlO_x), or low defect and ultrathin (epitaxial MgO or Al_2O_3). In this work, we develop a novel Atomic Layer Deposition (ALD) process which enables the growth of atomically-thin and low-defect density Al_2O_3 for MIMTJ devices. Exceptional control of the metal-insulator interface is required to achieve this end as any interfacial layer (IL) which develops is catastrophic, introducing defects and impairing the insulator growth. Specifically, two critical issues of pre-ALD IL formation and ALD nucleation on the metal surface were resolved by integrating ALD with sputtering *in situ* under High Vacuum (HV) along with a pre-ALD H_2O pulse to hydroyxlate the Al surface. *Ab-initio* molecular dynamics simulations were run to shed light on the mechanisms of IL formation in the HV environment and the hydroxylation of the metal surface using this pre-ALD H_2O pulse. In tandem, *in situ* Scanning Tunneling Spectroscopy (STS) quantified the quality of the Al_2O_3 as the IL was systematical reduced by optimizing the pre-ALD H_2O pulse, sample temperature, and pre-ALD heating time. After optimizations, STS revealed a remarkably high ALD Al_2O_3 tunnel barrier height which was constant down to the single monolayer scale of 1 ALD cycle with a band gap comparable to ultrathin epitaxial Al_2O_3. In addition, the highest known ALD Al_2O_3 dielectric constant, in the ultrathin thickness range, was measured in fabricated capacitors. Amazingly, capacitance fittings

along with STS imaging discovered that the IL thickness is sub-monolayer after our optimizations. Thus this work has achieved the first atomically-thin and low defect insulator for MIMTJ devices. Fabricated JJs show promise and preliminary tests reveal that this *in situ* ALD Al_2O_3 process can be grown on other metals such as Fe, which is essential for MTJ devices.

Acknowledgments

There are many people I must thank for helping me get to where I am today. First and foremost, my research advisor Dr. Judy Wu. I have changed so much since joining her group 3 ½ years ago, much more than can be put into words. She taught me an incredibly valuable lesson which is how to learn from my mistakes. No matter how many times I failed, especially early on, she never gave up on me and continued to push me to grow professionally. Eventually I did change and learn this lesson. For her patience and diligence, I am truly grateful. It is a lesson and a mindset that I will always take with me.

I would like to thank the other doctoral committee members: Dr. Cindy Berrie, Dr. Wai-Lun Chan, Dr. Siyuan Han, and Dr. Stephen Sanders for spending their valuable time and energy serving on my committee and reviewing my work. My former research advisor Dr. Matthew Antonik also deserves thanks for sharing his expertise in AFM and LabView with me. These skills have been instrumental in my research. I hope you success in wherever it is you ended up after your time at KU.

My coworkers and collaborators also deserve a great deal of credit and thanks. A PhD is truly a team effort. I would not be where I am today without the help of Dr. Alan Elliot who trained me, Dr. Ridwan Sakidja who's simulations and helpful discussions guided much of our work, and Jagaran Acharya whom I worked very closely with maintaining and fixing all the various problems and equipment in b078. Many other colleagues must also be thanked: Bo Liu, Ryan Goul, Melisa Xin, Brent Cook, Bibek Gautem, Allen Hase, Jeff Worth, and others not listed here.

Finally, I would like to thank my spouse Madison Alford for loving and supporting me during my PhD. Thank you so much for putting up with my late night fabrications, especially when I don't get ramen, and for my weekend writing sessions. I love you oodles!

Table of Contents

List of Figures

1 Introduction

In the past few years, the semiconductor industry has struggled to keep up with Moore's Law [1]. Moore's law states that the number of transistors in integrated circuits doubles roughly every 1-2 years [2, 3]. While this "law" is no more than an observation made by Gordon Moore in 1965, following it has become the quintessential goal of the semiconductor industry; especially for Intel which was co-founded by Gordon Moore. Nevertheless, Moore's law has held for the last 40 some years as transistor sizes decreased from 10 μm down to 10 nm today [1, 2, 4]. The 7 nm and 5 nm nodes will be soon to follow and are currently under intense research and development [5-8]. As Richard Feynman famously said during the 1959 annual meeting of the American Physical Society, "There is Plenty of room at the bottom" [9]. Indeed there is. Moore's law has taken us extraordinarily far however it cannot continue indefinitely. As transistor feature sizes approach the atomic-scale, quantum tunneling and defects become an increasingly significant concern. Transistor sizes below 5 nm may not even be possible. In this brave new world, radical manufacturing changes will be required to increase device performance [10, 11]. These manufacturing changes drastically increase the device fabrication complexity with each change bringing additional research and developmental challenges. For example, monolithic 3D chips expand the microprocessor into the 3rd dimension, shortening interconnect distances and increasing performance. However, these 3D chips will suffer from intense heat dissipation issues compared to planer chips due to their reduced surface area to volume ratio. Microfluidic cooling layers may need to be embedded within the 3D chips to dissipate this increased heat flux. These microfluidic layers will in turn severely impact the wiring interconnect design which will have to navigate through or around the microfluidic channels

[12]. This increased interconnect complexity may in turn cause problems for other steps of the microprocessor development.

Navigating this tsunami of manufacturing challenges leads to exponential growth of research and development costs without the usual corresponding improvement in chip performance due to an increased transistor density. The end of Moore's law is near (and may already be here). In their latest 14 nm node, Intel had to drop their long held tick-tock cycle of processor development where the tick refers to a new, smaller fabrication process, and the tock refers to architecture changes. The new norm is now tick-tock-tock, with the 2nd tock dedicated towards optimization of the processor architecture [13]. Additionally, to combat these increased development costs, wafer sizes are increasing from 300 mm to 450 mm for more economical processor production. These changes will temporarily hold back the rising tide of increased development costs but new materials and technologies are desperately needed to combat this intense economic pressure as computing technology approaches the end of Moore's law and beyond. In this world, size, defect density, and uniformity is paramount as our transistors and memory devices approach the atomic scale.

1.1 Metal-Insulator-Metal Tunnel Junctions

The Metal-insulator-metal tunnel junction (MIMTJ) is a fundamental structure for many microelectronic devices including Magnetic Tunnel Junctions (MTJs) for spintronics and fast access nonvolatile magnetic memory and Josephson Junctions (JJs) for particle detectors, magnetic field sensors, and qubits for quantum computers [14, 15]. MIMTJs are formed by sandwiching an ultrathin (less than about 2 nm in thickness) insulator between two metal electrodes (Figure 1.1a). Quantum tunneling is the dominant current transport mechanism between the two electrodes at this ultrathin scale. In the simplest approximation, Quantum tunneling in can be described by the 1-D finite potential barrier problem (Figure 1.1b). Through a simple undergraduate derivation, found in [16], the tunneling transmission function can be derived as Eq. 1.1.

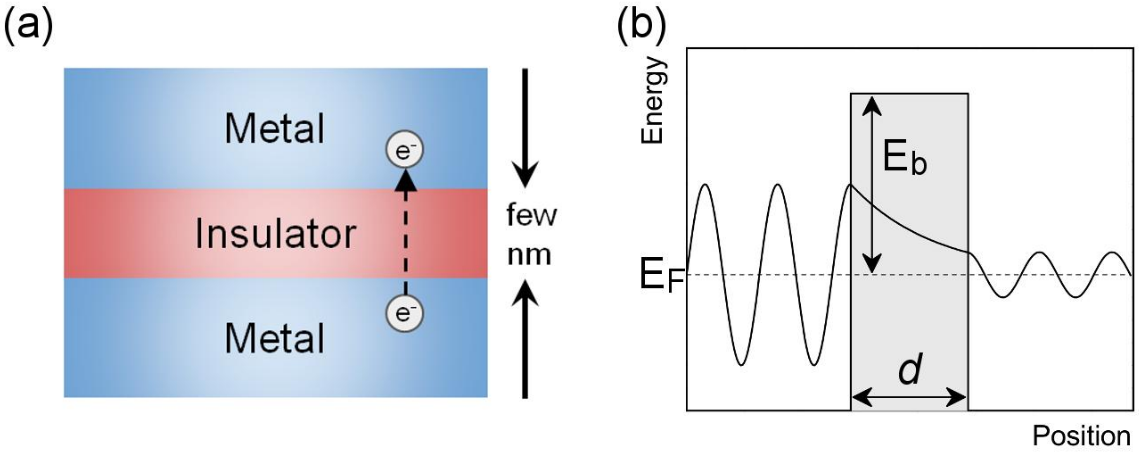

Figure 1.1: An illustration is shown for (a) the trilayer structure for MIMTJ devices and (b) quantum tunneling for electrons with the Fermi energy E_F through a 1D potential barrier of height E_b and thickness d.

$$T = \frac{16E_F E_b}{(E_F + E_b)^2} e^{-2d\sqrt{\frac{2m}{\hbar^2}E_b}} \qquad \text{Eq. 1.1}$$

Where E_F is the electron energy at the Fermi level, $E_b$is the barrier height relative to the electron energy, d is the barrier thickness, and $T$is the transmission function. The tunneling current through the barrier will be proportional to this transmission factor. Two critical insights can be understood from Eq. 1.1: (1) the tunneling current is exponentially dependant on the barrier thickness, $I \propto e^{-d}$, and (2) the tunneling current depends on the effective height of the barrier, $I \propto e^{\sqrt{E_b}}$. Thus to maximize tunneling current, it is essential that the barrier thickness (or distance between the metal electrodes) is minimized. A lower barrier height will also increase the tunneling current to a lesser extent, however a disproportionally higher leakage current will result. A high tunneling current is typically desired to both reduce device power consumption and increase performance in MIMTJ devices [17, 18].

1.1.1 The Josephson Junctions

One prime example of an MIMTJ is the Josephson Junction (JJ). The JJ, first described by Brian Josephson in 1962 [19], is a type of MIMTJ with the two metal layers replaced with superconducting layers. A diagram of this superconductor-insulator-superconductor trilayer structure is shown in Figure 1.2. When the superconducting layers are brought to within a few nanometers of each other, the superconductor wavefunctions couple together, allowing Cooper pairs to tunnel through the junction [20].

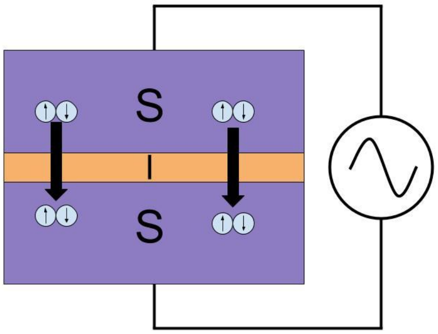

Figure 1.2: A simple schematic is shown depicting the Superconductor-insulator-superconductor trilayer structure of the Josephson Junction with Cooper pairs tunneling through the ultrathin tunnel barrier.

In his 1962 seminal paper [19], Brian Josephson derived the following two Josephson equations:

$$I = I_c \sin \varphi \qquad \text{Eq. 1.2}$$

$$V = \frac{\Phi_0}{2\pi} \frac{\partial \varphi}{\partial t} \qquad \text{Eq. 1.3}$$

Where I is the supercurrent through the JJ, I_c is the critical current of the JJ, φ is the phase difference between the two superconductor wavefunctions, V is the voltage across the junction, and Φ_0 is the magnetic flux quanta which is $\Phi_0 = {}^{h}/_{2e}$. h is Planck's constant and e is the elementary charge. Eq. 1.2 is the DC Josephson effect where a DC tunneling current occurs with zero voltage (constant phase) and Eq. 1.3 is the AC Josephson effect where an AC current develops at a finite voltage (time dependant phase). When Eq. 1.3 is combined with the time derivative of Eq. 1.2, we see that the JJ behaves as a non-linear inductor with the JJ inductance given by Eq. 1.4 [21].

$$L_{JJ} = \frac{\Phi_0}{2\pi I_c \cos\varphi} \qquad \text{Eq. 1.4}$$

Using the equation for the energy stored in the inductor ($U = \int IV\,dt$), the energy stored in the JJ can be calculated in Eq. 1.5.

$$U_{JJ} = \frac{-I_c \Phi_0}{2\pi} \cos\varphi \qquad \text{Eq. 1.5}$$

This potential is known as the “washboard potential” and is shown in Figure 1.3 [22].

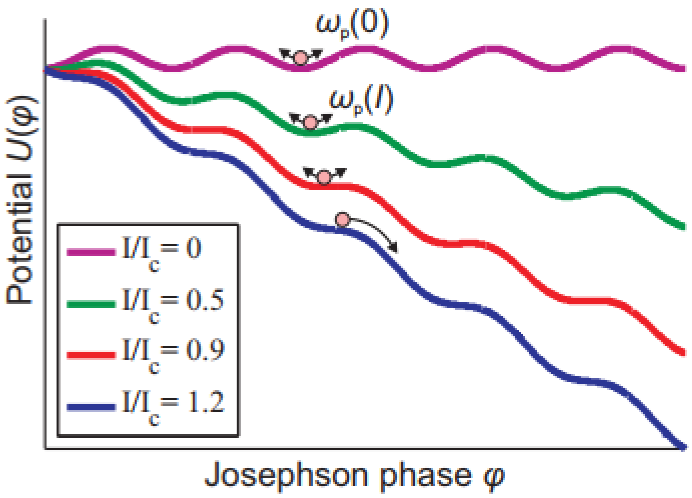

Figure 1.3: The stored energy in the JJ has been plotted against the phase of the JJ. Biasing the JJ with tunneling current tilts the washboard potential. The plot was taken from [22].

The JJ is confined within a trough of this washboard potential. When I is increased beyond I_c, the Cooper pairs break apart and the JJ transitions to the "normal" state with a finite resistance, R_N. For an un-shunted JJ, this transition occurs at the gap voltage given by $V_{gap} = {}^{2\Delta}/_{e}$ where Δ is the superconductor gap energy [21]. For Niobium, $2\Delta = 2.91 - 2.99\ \mathrm{meV}$ at typical measurement temperatures of about 4.2 K [22, 23]. If the current is dropped below I_c, quasiparticle transport remains dominant and a large, voltage dependant resistance, R_{sg}, develops (around 2 mV for Nb JJs). Eventually at the retrapping current I_r, the quasiparticles re-condense into Cooper pairs [22]. This behavior is shown in an example JJ I-V curve in Figure 1.4. The values of these parameters I_c, R_N, and R_{sg} can be used to judge the quality of the JJ. The I_cR_N product reflects the Cooper pair tunneling in the JJ. Cooper pair scattering and excess quasiparticle current typically reduces the I_cR_N product from the theoretical value of 2.24 mV (when measured at 4.2 K) to values around 1.8 mV. The R_{sg}/R_N ratio is another parameter which is used to judge the leakage current. Typical high quality JJs (when measured at 4.2 K) have R_{sg}/R_N ratios greater than about 10 [22, 24].

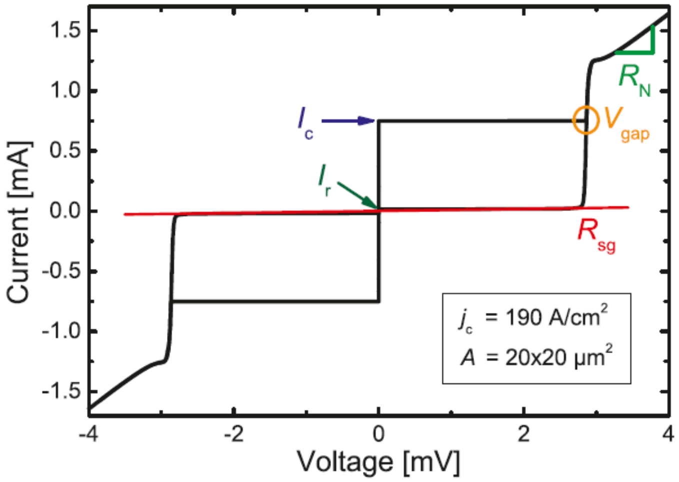

Figure 1.4: An example I-V curve is shown for a Josephson Junction from [22].

When a magnetic field is applied parallel to the plane of a JJ, the magnetic flux,Φ, modulates the JJ phase to include a magnet and spatial component which suppresses I_c. The junction area and insulator uniformity in thickness can be judged by measuring I_c vs. Φ and comparing the resulting Fraunhofer pattern with the theoretical one shown in Figure 1.5 for a square and circular junction [22, 25]. In particular, incomplete I_c suppression at the minima or I_c suppression at minima offsets are indicators of a non-uniform tunneling barrier [26].

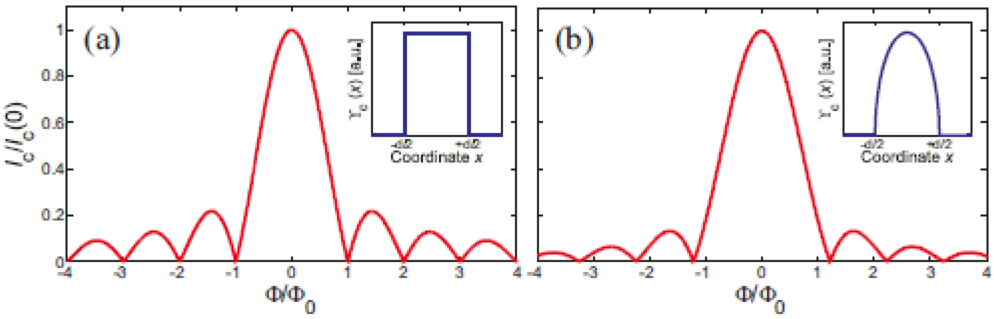

Figure 1.5: A Fraunhofer pattern is shown for a JJ with an ideal (a) square-shaped junction and a (b) circular-shaped junction. The figure was taken from [22].

1.1.2 Superconducting phase Qubits and Quantum Decoherence

A quantum computer is a macroscopic quantum system of entangled qubits. Quantum computers are particularly advantageous over traditional CMOS computing for quantum mechanical simulations, decryption, and database searching [27]. One of the most promising types of qubit is the superconducting qubit which is highly scalable and compatible with existing integrated circuit technology [28]. Superconducting phase qubits are among the most scalable of the three types of superconducting qubits (flux, phase, and charge) and are formed by integrating one large-area JJ in a superconducting ring which is coupled to a bias inductor [22, 29]. The large JJ capacitance has the advantage of reduced sensitivity to stray wire capacitance however the large junction area leaves the qubit vulnerable to defects within the JJ [29].

The classical analog to the superconducting phase qubit circuit is a nonlinear LC oscillator which has a characteristic resonant frequency ω_p[30]. Discrete energy levels are present in this potential well, as shown in Figure 1.6a. The energy difference between the ground and first excited state, E_{01}, is a function of both the frequency and the potential barrier, ΔU. Resonant microwave flux of frequency $\omega_{01} = {}^{E_{01}}/_{\hbar}$ can excite the qubit from the ground state to the first excited state. To measure the qubit, a bias current is applied to lower the potential barrier such that the first excited state has a high probability to tunnel to the other side of the potential barrier, whereas the ground state has a low probability. This behavior is shown in Figure 1.6b and Figure 1.6c. Tunneling through the potential barrier means that a voltage develops across the JJ [29].

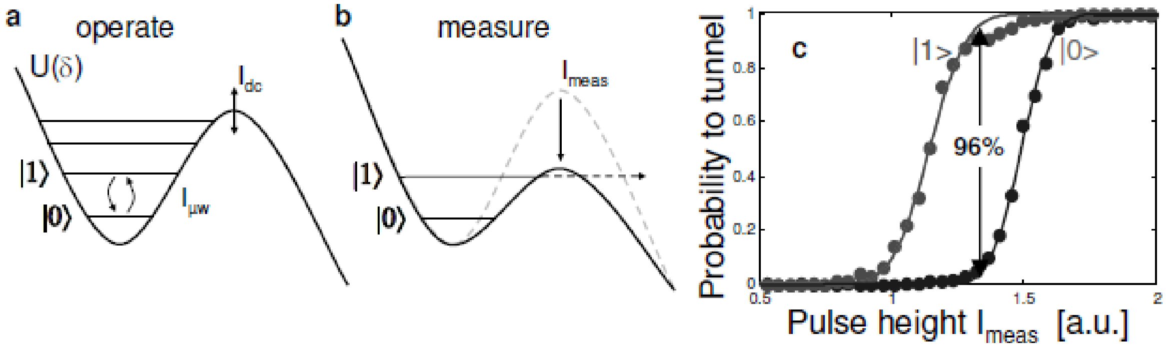

Figure 1.6: The operation and measurement of a superconducting phase qubit is shown. (a) The phase qubit has discrete energy levels in the washboard potential. Resonant microwave flux can be used to excite the qubit from the ground state $|0\rangle$ to the first excited state $|1\rangle$. (b) To measure the qubit, a bias current is applied to lower the potential barrier and increase the tunneling probability for the first excited state. (c) The tunneling probability is shown vs. the bias current for the ground and excited state. This plot was taken from ref [29].

In an ideal superconducting phase qubit, the probability of tunneling through the potential is 100% and 0% for the excited and ground state respectively. A plot of the tunneling probability as function of the microwave excitation frequency ω and Φ should be zero everywhere except for singular ω values for a given Φ. In reality, forbidden ω regions are observed (see Figure 1.7). These forbidden energy regions correspond to interactions between the qubit and a defect energy state. This decoherence can occur when the defect has comparable excitation energies between two discrete states, also known as a Two Level System (TLS). Qubits with large area JJs have many defect TLS which makes coherence difficult to achieve as plots like Figure 1.7 can be saturated with forbidden energy regions [29]. Quantum decoherence is a significant problem for qubits as all quantum computations must finish before decoherence. While superconducting qubits have excellent potential for their compatibility with current semiconductor fabrication technology their coherences times are currently too short for advanced quantum computations [22, 29, 31]. Therefore understanding the source of and reducing the density of TLS in superconducting qubits is essential to improve this technology.

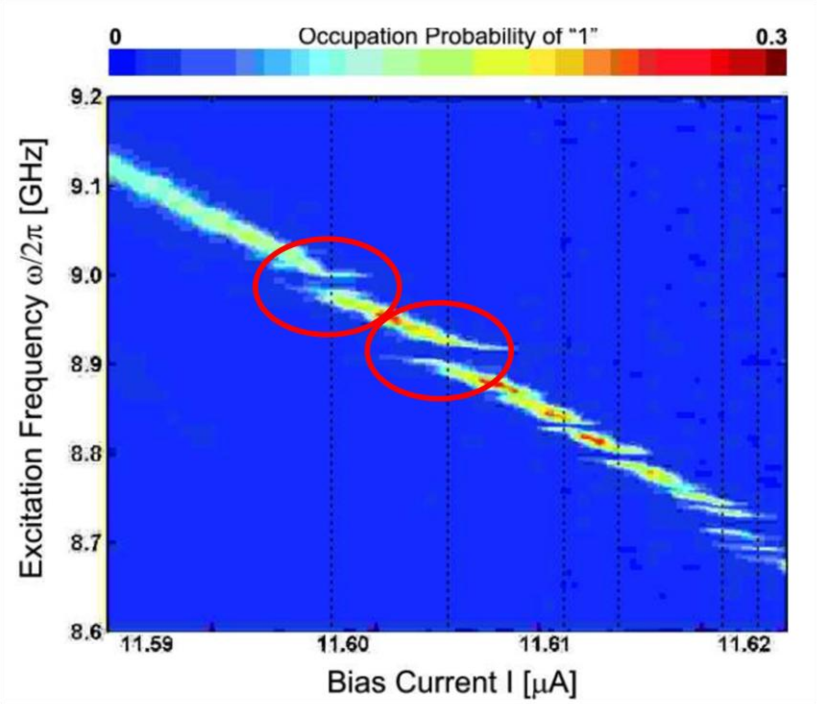

Figure 1.7: The qubit excitation frequency is shown against the bias current (or equivalently magnetic flux) in the qubit. The color scale denotes the probability that the qubit switches to the finite voltage state and the two red circles indicate forbidden energies. The plot was taken from [30, 32].

Defect TLS, also known as two-level-defects (TLDs) are typically found within amorphous dielectrics such as SiO_2 and AlO_x which are used for the superconducting wire insulation and the JJ trilayer respectively; although TLDs can also be present in the substrate [31, 33-35]. Defects with charge may switch randomly between two states, leading to telegraph noise in I_c which can push $I/I_c > 1$, leading to decoherence [30, 34]. Defects with dipole moments can also lead to I_c noise [31, 33-35]. Oxygen vacancies and OH groups are some examples of TLDs. To advance superconducting qubit technology further, these TLDs must be reduced. New insulating materials with low-defect densities are therefore highly desirable for the next generation of JJs and superconducting qubits.

1.1.3 Magnetic Tunnel Junctions

Magnetic Tunnel Junctions (MTJs) are another type of MIMTJ which is particularly sensitive to defects within the insulating layer and/or the interface with the insulating layer. In MTJs, the metal layers of the MIMTJ are replaced with ferromagnetic layers. Spin-polarized electrons tunnel through the tunnel barrier. When the magnetizations of the two ferromagnetic layers are aligned, many tunneling states are available whereas few tunneling states are available when the ferromagnetic layers are anti-aligned. This magnetization alignment is shown schematically in Figure 1.8(top). The percent change in resistance between these two alignments is defined as the tunneling magneto resistance (TMR) in Eq. 1.6 [15].

$$TMR = \frac{R_{AP} - R_P}{R_P} \quad \text{Eq. 1.6}$$

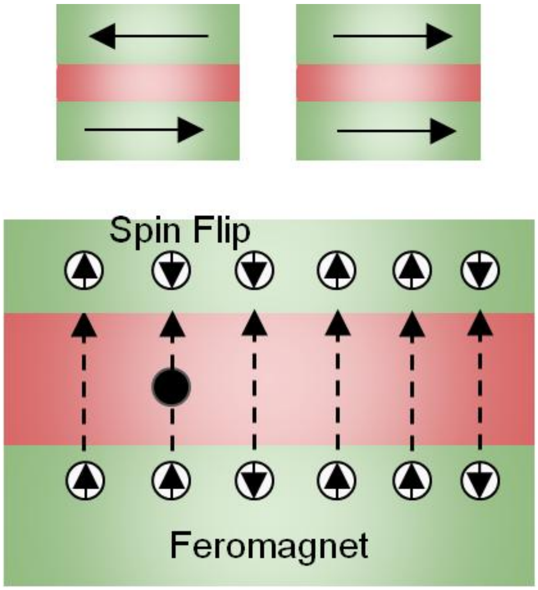

Figure 1.8: (top) A brief diagram of the ferromagnetic–insulator-ferromagnetic structure of the MTJ is shown. The diagram on the left shows the anti-parallel state of the MTJ where the magnetizations of the ferromagnetic layers in opposite directions. The right diagram shows the parallel state of the MTJ. (bottom) Spin polarized electron tunneling through the MTJ is schematically shown. In this diagram the majority carrier is denoted with the up arrow and the minority with the down arrow. The magnitude of the spin-polarized electron current is denoted as the number of “up” and “down” atoms. “up” is the majority state and “down” is the minority state. Defects within the insulator may cause some majority state carriers to flip to the minority state which will reduce the magnitude of the spin-polarized current and the TMR.

R_{AP} is the resistance of the MTJ when the ferromagnetic layers are anti-aligned (anti-parallel), and R_P is the resistance when the ferromagnetic are aligned (parallel). High TMR values are desirable for a greater signal to noise ratio, lower power consumption, higher speed, and large design margins for device fabrication [36]. To achieve a high TMR, R_{AP} must be maximized and R_P minimized. The tunneling properties of the dielectric layer are critically important for these parameters. Pinholes disproportionally reduce R_{AP} via non-spin-polarized electron current and defects within the insulator or at the ferromagnetic-insulator interfaces increase R_P due to scattering of the spin-polarized electron current (spin flipping), which is shown schematically in Figure 1.8 (bottom). Therefore to maximize the TMR, the MTJ must have a low RA product while maintaining a low defect and pinhole density within the insulator. These desires are in conflict with one another as thick tunnel barriers reduce pinholes and the effect of defects whereas thin tunnel barriers have low RA products. What is critically needed is an insulator which has a low defect and pinhole density in the sub-ultrathin thickness range of < 1nm.

1.2 Current Tunnel Barriers in MIMTJ devices

One current industry standard insulator for Josephson Junctions, as well as other MIMTJs such as MTJs, is thermal AlO_x [15, 37]. Thermal AlO_x is created through a controlled oxygen diffusion into an Al wetting layer. The AlO_x thickness is determined by the sample temperature during oxidation, the oxygen pressure, and the time in which the Al is exposed to the oxygen [38]. Typically, the oxidation is carried out around or below room temperature with active cooling to keep the temperature constant [18]. The oxidation pressure is typically held constant as the oxidation time is varied to grow thermal AlO_x at different thicknesses, The reason for this can be seen in Figure 1.9 which shows the measured AlO_x thickness as a function of oxygen exposure time for various oxygen pressures in the vacuum chamber [39]. As opposed to metals such as Fe which can oxidize completely upon exposure to oxygen, aluminum oxidation ceases after only a few nanometers since alumina acts as an oxygen diffusion barrier [40]. A higher oxygen pressure (or temperature) will increase this limiting thickness.

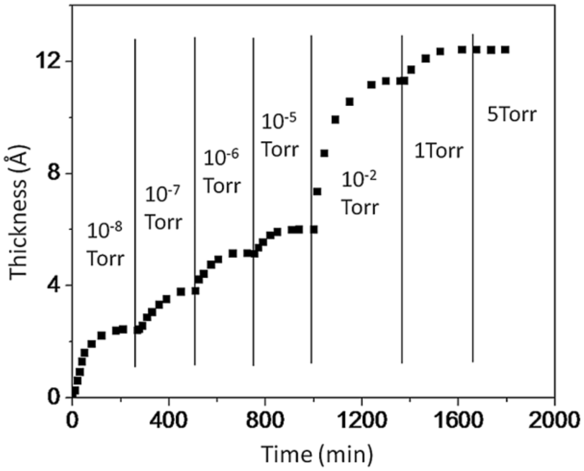

Figure 1.9: The thickness of the AlO_x is shown as a function of exposure time at different O_2 pressures. Plot taken from ref [39].

The alumina growth rate is exponential with the oxygen exposure (pressure * time), as shown in Figure 1.10.

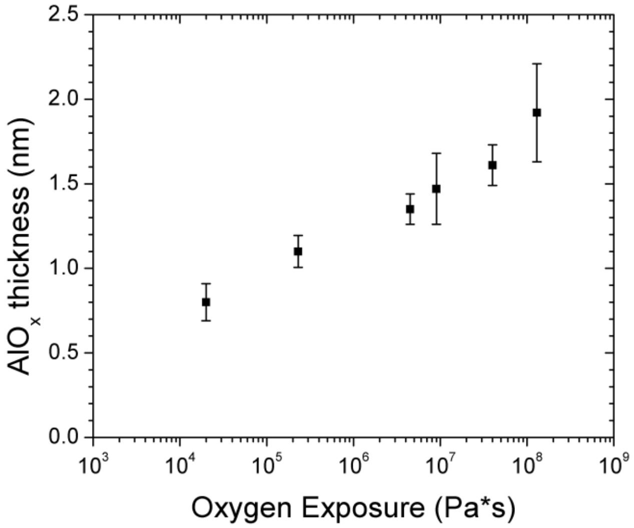

Figure 1.10: The experimentally measured thermal AlO_x thickness is plotted vs. the Al surface's exposure to oxygen at room temperature. Figures 2 and 5 from [41] have been combined, eliminating J_c, to generate this figure.

Since the AlO_x thickness can be difficult to measure directly, most groups experimentally calibrate the MIMTJ tunneling current density, J, (J_c for JJs) with the oxygen exposure. A plot of J_c vs. oxygen exposure is shown in Figure 1.11 [20]. What is particularly interesting about this figure is that there is an abrupt change in the J_c trend with oxygen exposure. A change in the apparent slope (on the log-log scale) occurs for a thermal AlO_x thickness of around 0.4 nm [20, 41]. Above this thickness, the slope is constant which implies that E_b is constant with thickness. This is the low J_c region where the oxidation is dominated by diffusion into the Al film. The high J_c region, below about 0.4 nm, corresponds to the early stages of AlO_x nucleation and growth [18, 20, 39]. Thermal AlO_x films grown in this range do not create useful tunnel barriers due to the presence of defects, such as oxygen vacancies, and pinholes [20, 35]. These defects provide additional tunneling states which reduce the effective E_b, increasing the transmission through the barrier (see Eq. 1.1). As the thermal AlO_x is grown thicker, pinholes become less prevalent and the overall quality of the tunnel barrier increases [20, 41].

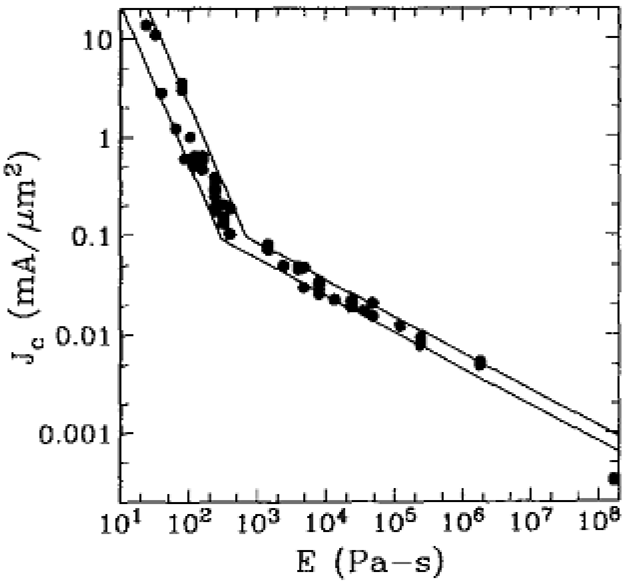

Figure 1.11: The JJ J_c is plotted as a function of Al exposure to oxygen (pressure * time). The plot was taken from ref [20].

Plasma assisted oxidation can significantly improve the density of the alumina and reduce the defect density. The E_b of plasma assisted oxidation is significantly higher than un-assisted thermal oxidation with an E_b value of around 1-3 eV [15, 42, 43] compared to 0.6-1eV [15, 41]. However the interface issues remain and pinhole-free and low-defect growth is not possible when the thickness is pushed down to just a few Ås. Al_2O_3 sputtering and e-beam evaporation suffer from similar problems with island-based growth [20, 44, 45].

Epitaxial Al_2O_3 growth is a possible alternative to thermal oxidation and can be achieved with a high temperature post anneal following thermal oxidation [46] or by Molecular Beam Epitaxy [47]. JJs with epitaxial Al_2O_3 have been achieved on a Re base electrode [48]. They reported a TLD density which was lower than thermal AlO_x tunnel barriers by a factor of 5. However these epitaxial growth methods are limited by strict lattice matching requirements and require very high temperature depositions or post-anneals. This severely limits the choice of materials which are compatible with epitaxial Al_2O_3 growth and is generally unappealing to the semiconductor industry as thermal budgets can easily be exceeded [49]. In addition, due to the possibility of defective grain boundaries, epitaxial insulators with thicknesses below 1 nm are not feasible for tunnel junctions.

1.3 Atomic Layer Deposition

Atomic Layer Deposition (ALD) is another alternative to thermal oxidation. ALD is an offshoot of chemical vapor deposition (CVD) which breaks CVD up into a series of reactant vapor pulses separated by a low vacuum purge [50, 51]. Although in some industry applications, this purge step is replaced by a stream of precursor gas separated with layers of nitrogen gas. The wafer is then continuously moved through the chamber [52]. In either case, separating the reactants ensures that the ALD growth is well-defined with each cycle of reactant exposure resulting in one atomic monolayer of deposition [53]. One of the most well known and studied

ALD reactions is the Trimethylaluminum (TMA) - H_2O process for Al_2O_3 growth [51, 54]. Figure 1.12 shows a conceptual illustration of this method and equations Eq. 1.7 and Eq. 1.8 show the chemical reaction [53].

$$AlOH_{ad} + Al(CH_3)_3 \rightarrow AlOAl(CH_3)_2 + CH_4 \qquad \text{Eq. 1.7}$$

$$AlCH_3 + H_2O \rightarrow AlOH + CH_3 \qquad \text{Eq. 1.8}$$

Were "*ad*" denotes adsorbed surface species.

The first step of ALD is a short pulse of TMA into the ALD reactor (Figure 1.12a) using solenoid values controlled by a computer. A nitrogen carrier gas is sometimes added to enhance the pulse height, or else longer pulses are used [53]. The TMA reacts with adsorbed hydroxyl groups, $\mathrm{OH_{ads}}$, on the sample's surface to form Dimethylaluminum and the release of methane CH_4 (Figure 1.12b). Next, after a quick purge, H_2O is pulsed into the ALD reactor (Figure 1.12c). H_2O completes the reaction, releasing the remaining CH_4 and preparing the top surface with OH (Figure 1.12d). This top OH provides a nucleation site for the next ALD cycle, enabling ALD to be deposited for as many cycles as desired [51, 53, 54].

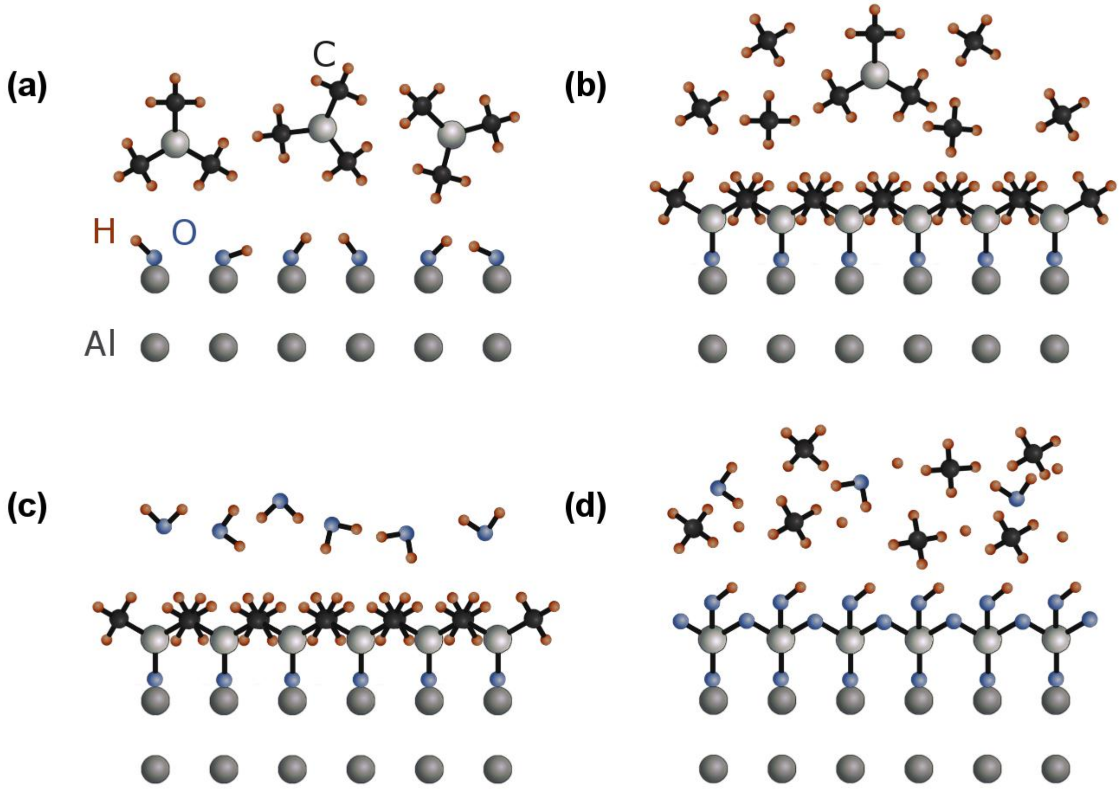

Figure 1.12: The processing steps for an ALD Al_2O_3 reaction are shown in a simple cartoon. (a) First a TMA pulse enters the vacuum chamber, (b) the TMA reacts with hydroxyl groups on the surface, releasing CH_4, (c) then after a purge step, a H_2O pulse is introduced into the vacuum chamber, (d) this H_2O complete the ALD Al_2O_3 reaction, releasing CH_4 TMA and preparing the top surface with Hydroxyl groups.

The principle strength of the ALD process is that the reactions given in Eq. 1.7 and Eq. 1.8 go to completion. Completion means that each available reaction site on the surface becomes filled after each reactant pulse, after which no additional reactions take place. This completion nature provides ALD films will three significant advantages: (1) the growth rate is well defined with each cycle depositing exactly one monolayer of Al_2O_3 with a thickness of around 1.1-1.2 Å [51, 55, 56], (2) highly conformal growth is possible even on high aspect ratio structures such as nanotubes [53] which is a property coveted for industry applications such as gates for FinFet transistors[57], and (3) ALD films have a low-defect density with few oxygen vacancies which may lead to a reduced TLD density in JJs [33]. Additionally, ALD is a very flexible deposition method which can deposit a huge variety of films [50, 51] in a wide temperature window of typically (100-350 °C) which is compatible with many thermal budgets in microchip processing [58, 59].

1.3.1 ALD Nucleation and Interfacial Layer Formation

However there are two significant challenges that must be overcome for ALD to grow high quality Al_2O_3 dielectrics for the next generation of MIMTJ devices. The first is oxidation of the metal layer ***before*** ALD. ALD is typically a low vacuum process whereas the metal layers in MIMTJs are typically grown using Physical Vapor Deposition (PVD) methods such as sputtering or e-beam evaporation which require high-vacuum (HV) pressures to reduce defects within the deposited films [60]. To integrate with these metal depositions, the sample must traverse these two vacuum environments. The most straightforward method of doing this is to remove the sample from the PVD vacuum chamber and carry it over to the ALD chamber *ex situ*. This has actually been attempted by other groups for ALD Al_2O_3 on $Si/SiO_2/Au/Al$ substrates which had an exposure to atmosphere of about 1 min after Al deposition [61]. They found an extremely large junction resistance of 18 $M\Omega\mu m^2$ for only 18 cycles of ALD which is rather unsurprising since they neglected to consider that at typical ALD deposition temperatures Au and Al form a well known resistive intermetallic, known as “White Plague”, which can be micrometers thick [62]. Additionally, their “1min” exposure to atmosphere has an oxygen exposure on the order of 10^6 Pa*s which, as can be seen in Figure 1.10, gives a thermal AlO_x thickness of about 1.2 nm; which is a little over half of the expected ALD Al_2O_3 thickness for 18 ALD cycles. As is evident from this example, pre-ALD oxidation is a major problem. This thick and defective IL from this very short exposure to atmosphere is enough to completely destroy and negate the advantages that ALD has to offer [63, 64]. Pushing below ultrathin thicknesses is simply impossible with an ultrathin-scale IL. However even *in situ* sample transportation, under low-vacuum, can create an IL which is greater than 0.5 nm in thickness [56, 65]. This problem or pre-ALD IL formation must be thoroughly addressed for ALD to grow useful dielectrics demanded by the next generation of MIMTJs.

The second significant challenge that must be overcome to integrate ALD into MIMTJ fabrication is how to provide a hydroxylated metal surface for TMA nucleation. As can be seen in Figure 1.12, the surface below ALD must have available $\mathrm{OH_{ads}}$ for TMA nucleation to occur [53, 66]. ALD nucleation on metal surfaces is particular challenging since hydroxyl groups are not readily available and any exposure to atmosphere may result in a significant IL, making chemical treatments to hydroxylate the surface difficult [67, 68]. Inert metal surfaces, such as Pt and Au, may be safely taken out of vacuum without IL growth however hydroxylation of these metals is extremely difficult. ALD growth will eventually occur but only after about 30-50 cycles of ALD as an ultrathin IL gradually forms [69]. Sticking with reactive metal surfaces such as Al will not innately solve the problem as an AlO_x IL can still form with a thickness on the order of 2 nm [65, 69, 70]. To achieve atomically-thin ALD Al_2O_3 growth on a metal surface without IL formation, both of these equally significant problems of pre-ALD IL formation most be resolved. A method to hydroxylate a metal surface which is compatible with an *in situ* PVD-ALD system is therefore required.

1.4 Approach of this Work

The next generation of MIMTJ devices demands a new insulator which maintains a low pinhole and defect density all the way down to the atomic-scale. ALD shows great promise to grow insulators which satisfy this demand due to it's self-limited and complete chemical reactions. However careful incorporation of ALD into MIMTJ fabrication must be taken as the bottom electrode can oxidize prior to ALD and without careful control of the metal surface, ALD can nucleate with a defective IL. In this work we resolve these two critical issues by integrating ALD with PVD *in situ* under HV along with a pre-ALD H_2O pulse to hydroxylate the aluminum surface.

The grand goal of this work was to develop and optimize this *in situ* PVD-ALD process to grow high-quality and atomic-scale Al_2O_3 tunnel barriers for MIMTJ devices. Understanding the mechanisms of IL formation, even under HV, and it's impact on the ALD Al_2O_3 growth quality was essential to achieve this end. This understanding was acquired using *Ab-initio* Molecular Dynamics (AIMD) simulations in tandem with experimental study. Numerous AIMD simulations were run to shed light on the mechanisms of IL formation and on the chemistry of the pre-ALD H_2O pulse. The atomic-scale of the Al_2O_3 and IL excluded standard experimental characterization methods such as ellipsometry, X-ray photoelectron spectrometry and transmission electron microscopy. Capacitor and JJ device fabrication was occasionally used to quantify the ALD Al_2O_3 quality but the bulk of the characterization was done using *in situ* Scanning Tunneling Spectroscopy (STS). STS is a scanning probe microscopy technique which is particularly well-suited for studying atomic-scale insulators for it’s fast turnaround time and ability to measure the insulator density of states locally with atomic-scale precision. This capability allowed STS to measure the impact the IL had on electron tunneling.

With our synergetic approach of AIMD to measure the mechanisms of IL formation and STS to measure the impact the IL had on electron tunneling we were able to optimize the *in situ* ALD deposition process (pre-ALD H_2O pulse, temperature, and heating time) to minimize the IL growth. We find that monolayer ALD Al_2O_3 can be achieved on Al with a sub-monolayer IL. This claim was verified with fabricated capacitors and an *in situ* STS and AFM study. This extremely fine IL control enabled us to grow ALD Al_2O_3 which was atomically-thin with a very high surface coverage and high tunnel barrier height. Finally we did some preliminary studies on the quality of MIMTJ devices with this atomically thin ALD Al_2O_3 insulator and expand our *in situ* ALD Al_2O_3 process to be suitable for MTJ devices.

2 Experimental

2.1 Chapter Overview

In this chapter we discuss the *in situ* MIMTJ fabrication method, the HV sample transfer to the Scanning Probe Microscopy (SPM) chamber, STS for *in situ* sample measurement, and the JJ device fabrication procedure. This unique machine integrates sputtering, ALD, and SPM together with HV *in situ* sample transport to enable the fabrication of MIMTJ devices with highly minimized IL growth and to measure the impact of any remaining IL *in situ* before the deposition of the top metal electrode.

2.2 In Situ MIMTJ fabrication

The *in situ* PVD-ALD system was developed by prior students. Additional details can be found in [71] and some photos are shown in Figure 2.1. To summarize briefly, samples are loaded into the load lock chamber and then moved between all chambers (Figure 2.1a) using the transport rod and a rail system shown schematically in Figure 2.1b. The sample stage has a rail which inserts into a precisely aligned socket found in the sputtering chamber (Figure 2.1c), load lock (Figure 2.1d), and the ALD chamber (Figure 2.1e). The transfer rod has a threaded end when screws onto the sample stage to enable transport between all chambers using a single transfer rod.

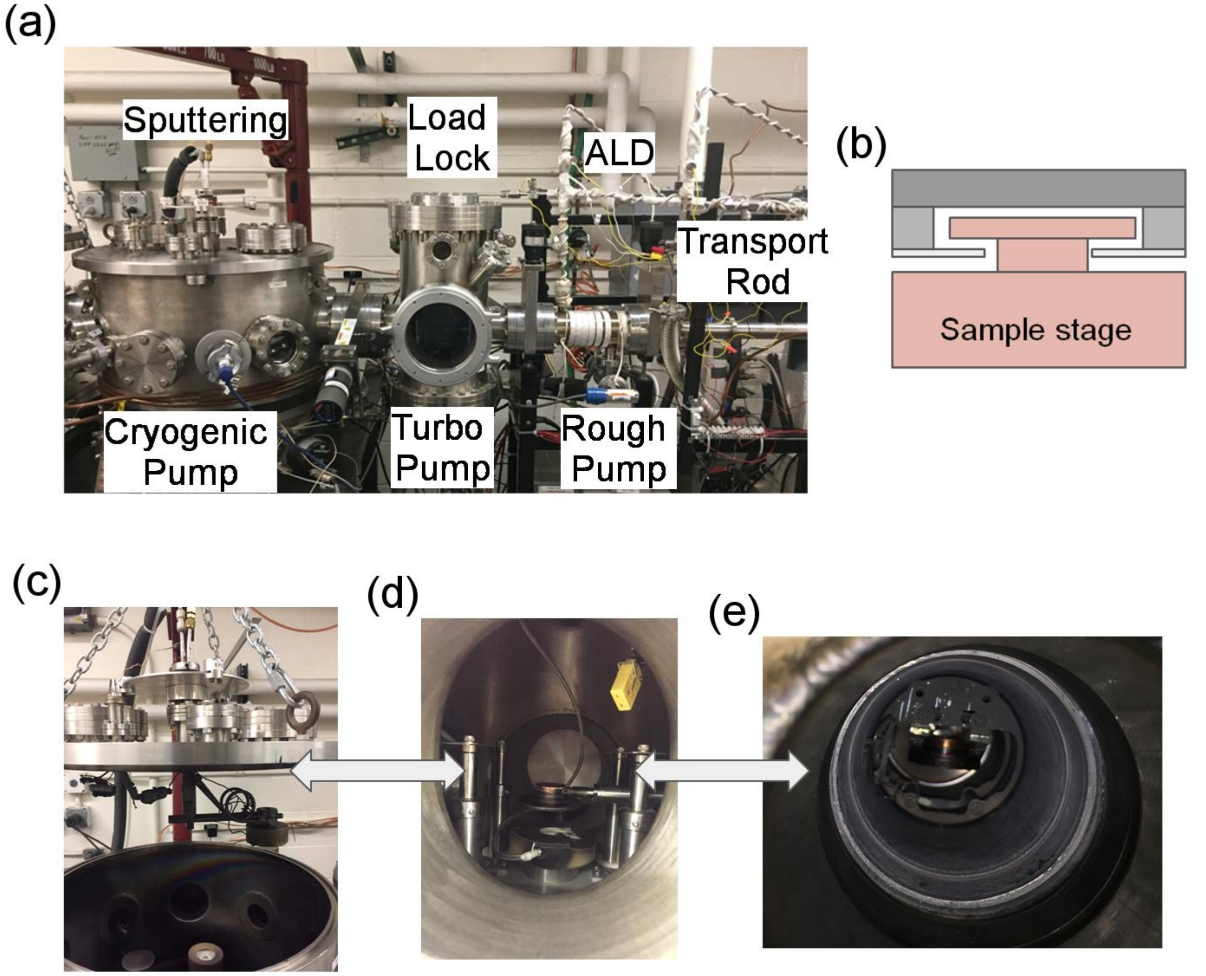

Figure 2.1: Some photos of the MIMTJ deposition system are shown along with a simple schematic of the sample transport rail system. (a) The three major chambers are shown. (b) A rail system is used to allow for the transport rod, to move the sample stage between the vacuum chambers. (c) The sputtering chamber is shown (with the top off), (d) The load lock is shown with a sample stage on the transport rod, and (e) a sample stage is shown inside the ALD chamber.

To fabricate the MIM structure, samples were transferred to the sputtering chamber where a bilayer of Nb and Al was magnetron sputtered at a rate of 1.7 nm/s and 0.5 nm/s with a wattage of 330 W and 90 W respectively. The Ar pressure during sputtering was 14 mTorr and the Nb and Al targets were presputtered for 5 min each. To reduce oxidation during sputtering the sputtering chamber was pumped to a base pressure of around 10^{-7} Torr. Before ALD, the ALD source lines were purged with a roughening pump and the ALD chamber was preheated and pumped with the load lock turbo pump to ensure a good HV pressure in the chamber. After Nb/Al sputtering, the samples were transferred to the ALD chamber and heated in preparation for ALD. Immediately following sample heating, the ALD chamber was isolated, a roughing pump took over the pumping, and ALD began. The reactants H_2O and Trimethylaluminum were pulsed into the ALD chamber for 1-3 s along with a 5 sccm N_2 carrier gas with a purge step between pulses. Immediately following the last pulse of ALD, the gate to the load lock was re-opened and the turbo pump restarted to return the sample to a HV environment as soon as possible. Then the transfer rod was re-threaded to the stage and the sample was returned to the sputtering chamber where a top layer of Nb was sputtered for MIMTJ devices.

2.3 *In Situ* Transport to Scanning Probe Microscopy Chamber

To measure the ALD Al_2O_3 quality with STS, the sample was transferred to the SPM chamber immediately after ALD. To achieve this transfer, an SPM chamber, SPM Load lock, and two transfer arms were added to the system. A sputtering chamber for magnetic materials was also added for MTJ device fabrication. Photos of this expanded system are shown in Figure 2.2. To get to the SPM chamber from the sputtering chamber, the sample had to move through the magnetic sputtering chamber (Figure 2.2a), switch from the long transfer arm to the short

SPM transfer arm (Figure 2.2b), and finally into the SPM chamber for tunnel barrier measurement (Figure 2.2c).

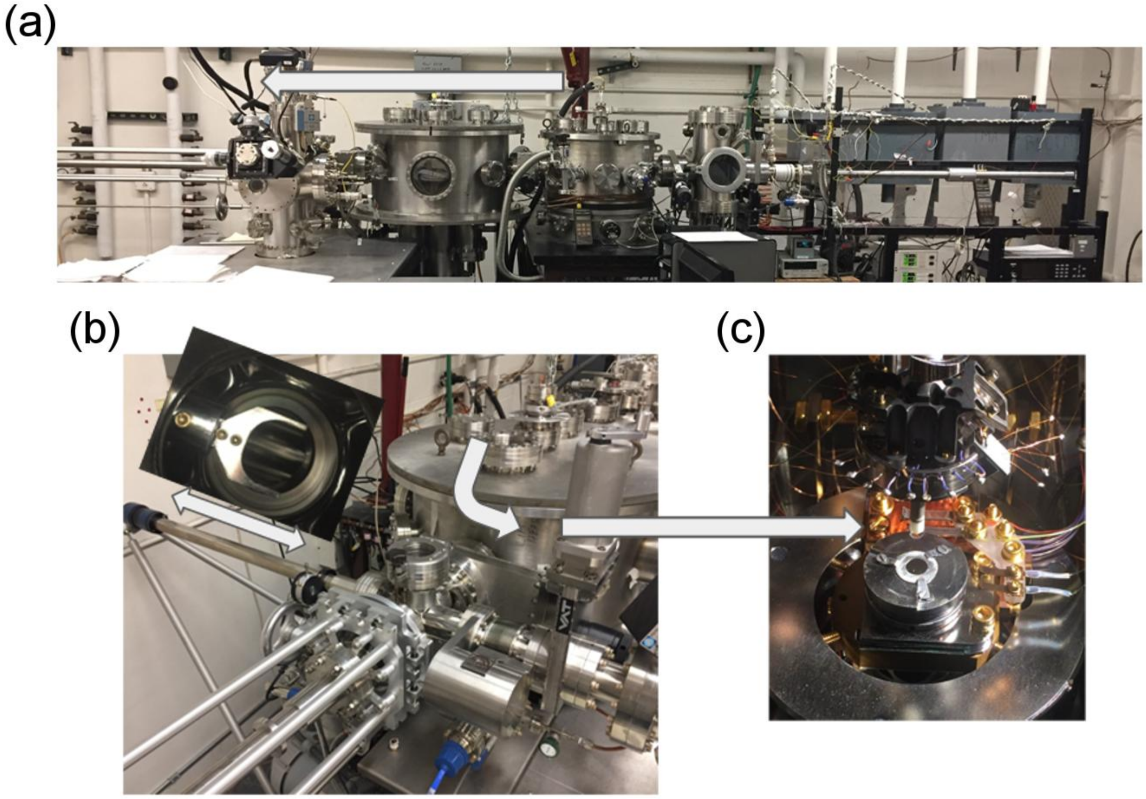

Figure 2.2: Photos are shown for the *in situ* transport path from the sputtering chamber to the SPM chamber. A photo is shown of the (a) entire PVD-ALD-SPM system, (b) junction between the magnetic material sputtering chamber, SPM chamber, and SPM load lock where the SPM stage had to be moved to the short transfer rod, and (c) sample inside the SPM chamber. The arrows depict the direction the samples had to travel through the vacuum chambers.

One significant technical challenge that had to be overcome to transfer samples from the sputtering to the SPM chamber was that the sample stage had to maintain compatibility with the MIM fabrication system. To maintain this compatibility, an adaptor stage was designed and fabricated (shown in Figure 2.3a) with an identical rail setup as the old MIM fabrication stage. The SPM stage slides into a socket on this adaptor stage, shown in Figure 2.3b. As can be seen in these photos, this SPM stage has a small about 1-2 mm grove cut along its circumference. A grabber arm, shown in Figure 2.3c, can slide into this grove and close to grab the SPM stage. When retracted, this grabber arm pulls the SPM stage and adaptor apart. A simple schematic for this transfer strategy is shown in Figure 2.3d.

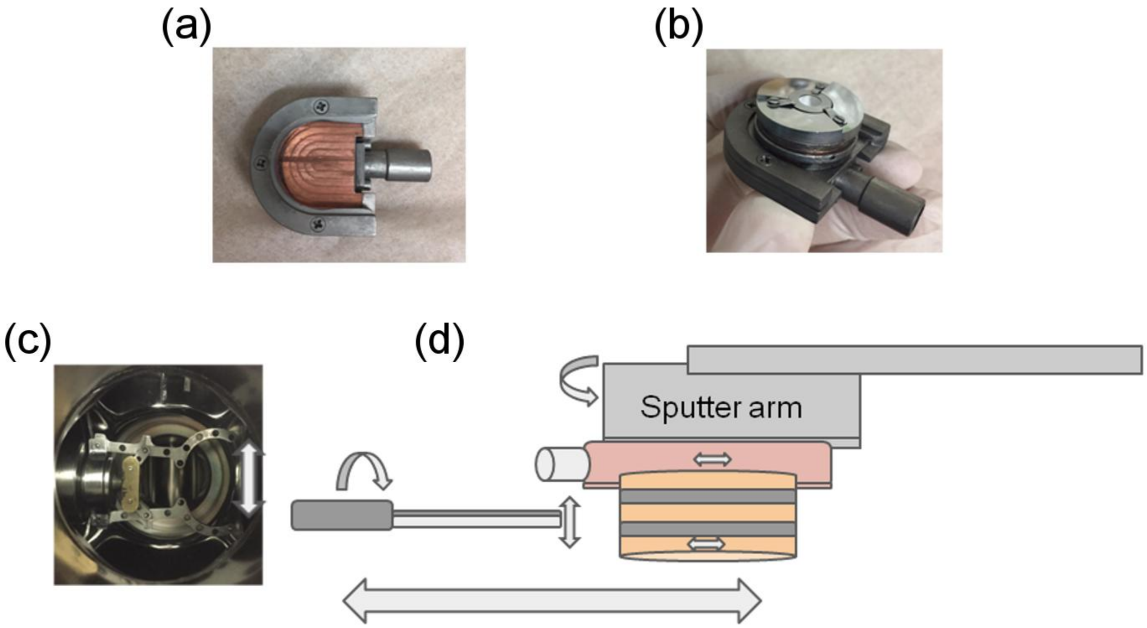

Figure 2.3: Photo and diagrams are shown for (a) the adaptor stage, (b) the SPM stage inserted into the adaptor stage, (c) the long grabber arm, and (d) a diagram is shown for the transfer process from the sputtering chamber to the grabber arm. The small arrows depict the degrees of freedom each piece had and the large arrow depicts the direction of travel during the transfer.

There were two significant challenges with this transfer: (1) the friction between the SPM stage and the adaptor was extremely sensitive and (2) there were 6 degrees of freedom during the transfer, all of which had to be aligned in the vacuum chamber with poor visibility. If the friction between the two stages was too high then the two parts would not easily come apart during the transfer. This often resulted in the adaptor stage been brought along with the SPM stage, which was un-compatible with the SPM chamber. If the friction was too low, then the SPM stage would fly off during sputtering as the sputtering arm was rotated over the Nb/Al targets, or even during the ALD transfers. Compounding these problems was that over repeated transfers, the rail on the SPM stage wore down slightly, reducing the friction with the adaptor. SPM stages which fell off the adaptor required a chamber venting for retrieval and significant down time on the system as HV was restored; particularly if the stage was dropped in the ALD chamber. The solution to this problem was to periodically abrade the adaptor stage using fine-grit sandpaper to reduce the gap in the rail socket. Frequent testing with the SPM stage ensured that not too much copper was removed.

The 2nd challenge of degrees of freedom was resolved with careful visual inspection in the chamber window, a step-by-step sample transfer protocol, and some clever engineering. To allow for grabber arm height and position adjustment, the long transfer arm was connected to a set of bellows and rigged to a custom designed adjustment system shown in Figure 2.4. The transfer arm was adjusted as the three adjustment wheels were turned: one for height, one for horizontal movement, and one for the angle of the transfer arm in the horizontal plane. This adjustment wheel setup is shown in Figure 2.4a. A small dial was connected to the vertical offset to record the height of the transfer arm (Figure 2.4b). Since the long transfer arm was only connected at one end, there was significant droop on the end with the grabber arm. This meant that different transfer arm heights were needed depending on the weight at the grabber end. Several dial positions were calibrated to enable transfers into and out of the sputtering chamber (with/without sample stage). After successfully transferring the sample to the SPM load lock, the long transfer arm height was adjusted to switch to the short transfer arm which moved the sample to the SPM chamber to complete the process.

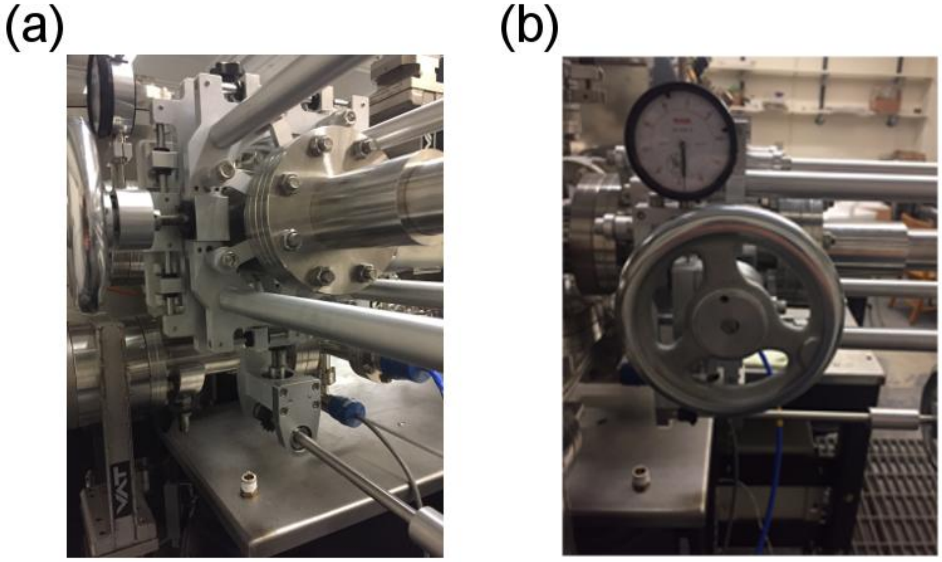

Figure 2.4: Some photos are shown for the long transfer arm adjustment setup in our system. (a) When the adjustment wheels are turned, threaded rods shift the transfer arm vertically and horizontally. (b) A dial records the vertical offset of the transfer arm.

2.4 Scanning Tunneling Spectroscopy

STS is a scanning probe microscopy method which utilizes an atomically sharp metallic tip to study the local electronic structure of the surface below the tip. Atomically-sharp means that when the tip is brought to within a few nanometers of the sample's surface electrons predominantly tunnel between the sample and the closest atoms on the tip, allowing for atomic resolution imaging and spectroscopy of the sample's surface.

The atomically sharp metallic tip is typically either a mechanically cleaved Pr-Ir wire or an electrochemically etched tungsten wire [72]. Scanning Electron Microscopy (SEM) images for these two types of Scanning Tunneling Microscopy (STM) tips are shown in Figure 2.5. As is clear from these photos, etched tungsten tips are significantly sharper than cut Pt-Ir tips. Most groups which do atomic resolution STM imaging at liquid helium temperatures use etched tungsten tips. Etching polycrystalline W wire to create a W tip is fairly straightforward with a KOH or NaOH electrochemical etch. However when exposed to atmosphere, a ~20 nm thick insulating layer of WO_3 forms which must be removed before STS measurement. This can be done by heating the tip above 800 °C using resistive heating, electron beam bombardment or self-sputtering. Great care is required as excess heating can dull the tip [72, 73]. The sharpness achieved in these W tips makes them excellent for STM imaging, however this high temperature anneal, required for STS with these tips, adds many technical challenges.

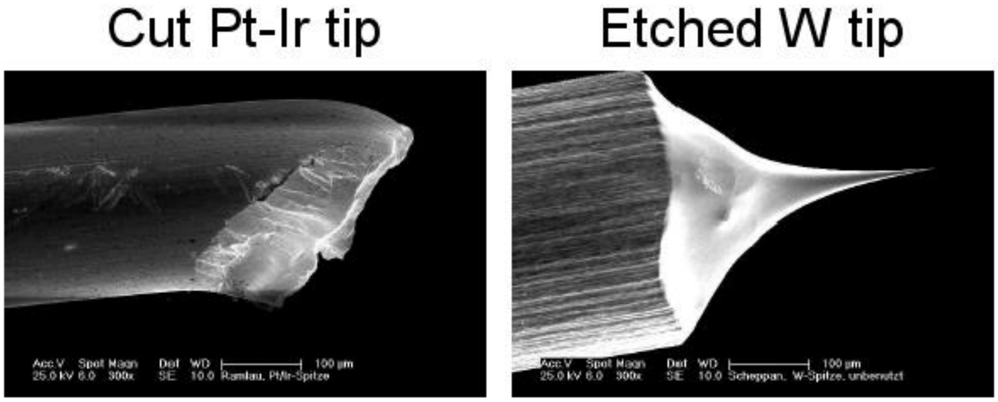

Figure 2.5: SEM images are shown for a cut Pt-Ir wire (left) and an electrochemically etched Tungsten wire (right). Images were taken from [72].

Instead in this work, we focused on mechanically cut Pt-Ir tips. Pt-Ir tips are formed, with a little luck, by cutting a Pt-Ir wire. Since the Pr-Ir alloy does not oxidize easily, these tips are well suited for STS studies [73]. Different group have their own preferred method of cutting these tips. Our method for producing Pt-Ir tips is shown schematically in Figure 2.6a along with an example of one of our sharp tips in Figure 2.6b. We used a sharp, TiN-coated, pair of scissors to do the cutting. We had the most success when this cut was performed at a very sharp angle with the scissors moving quickly upwards in one smooth motion. Typically several attempts were required before a satisfactory cut was achieved. A tip was considered sharp when STS spectra on a well-known sample had low noise.

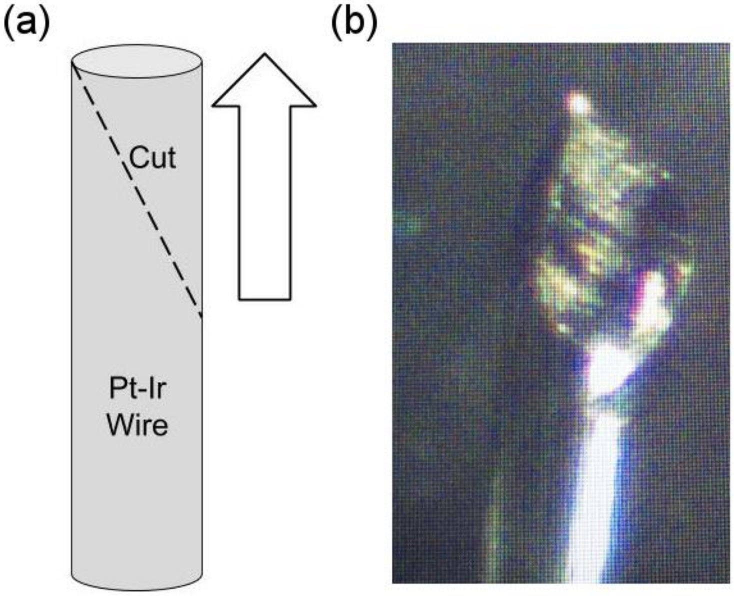

Figure 2.6: Our procedure for producing Pt-Ir tips is shown. (a) A sharp pair of scissors cuts a Pt-Ir wire along the dashed line at a sharp angle while being moved upwards away from the tip in one fast motion. (b) An optical image of a sharp Pt-Ir tip is shown.

2.4.1 Tunneling for STS

When this sharp, metallic tip is brought to within a few nanometers of the sample's surface, electrons can tunnel across the vacuum gap between the tip and the surface. The local electronic structure on the surface beneath the tip can be probed as the bias voltage between the tip and sample is varied and the tunneling current measured. Figure 2.7a shows the tip-sample setup with the bias voltage applied. Electron tunneling through the vacuum gap between the metallic tip and metallic sample surface is similar to the 1-D tunneling model from Figure 1.1 and is shown in Figure 2.7b were z is the tip-sample distance. An trapezoidal tunneling barrier arises in the usual case of different tip and sample work functions (ϕ_{tip} and ϕ_{sam}) [74]. The Wentzel-

Kramers-Brillouin (WKB) approximation can be applied to analytically solve this trapezoidal barrier shape (integrating with infinitesimally thin square barriers), however this level of precision is not needed for STS as other noise sources will dominate, especially for room temperature STS measurements [75, 76]. Instead, the average barrier height, defined in Eq. 2.1, may be used to define an approximate 1-D square barrier.

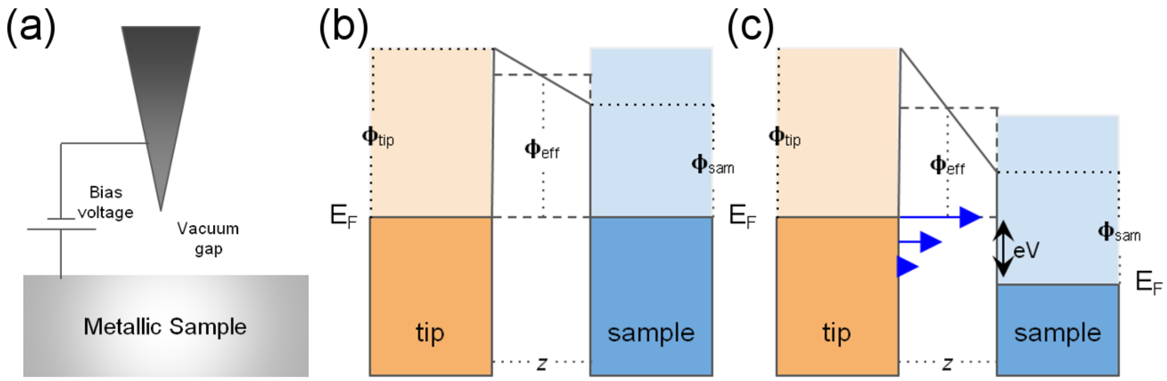

Figure 2.7: Schematic diagrams for STS are shown including (a) the STM tip and sample layout, (b) the tunnel barrier for electrons in the tip, and (c) the energy structure when a bias voltage is applied between the tip and sample.

$$\bar{\Phi} = \frac{\Phi_{tip} + \Phi_{sample}}{2} \qquad \text{Eq. 2.1}$$

When a voltage is applied between the tip and the sample, the barrier shape changes slightly (Figure 2.7c). A positive bias voltage raises the tip Fermi level by $\frac{1}{2}eV$ and lowers the sample Fermi level by $\frac{1}{2}eV$. This energy, $E = eV$, given to the electron by the bias voltage lowers the effective barrier height, Φ_{eff}, for an electron in the STM tip with energy E, as shown in Eq. 2.2.

$$\Phi_{eff} = \overline{\Phi} + \frac{1}{2}eV - E \qquad \text{Eq. 2.2}$$

This effective barrier height, Φ_{eff}, takes the place of E_b from Eq. 1.1, giving rise to a new transmission function which is proportional to Eq. 2.3.

$$T \propto e^{-2d\sqrt{\frac{2m}{\hbar^2}\left(\overline{\Phi}+\frac{1}{2}eV-E\right)}} \qquad \text{Eq. 2.3}$$

2.4.2 STS of Insulators

STS can also be used to study the electronic structure of insulators provided the bias voltage is applied to a conductive surface below the insulator. For our STS studies on ALD Al_2O_3, we sputtered a bilayer of Nb/Al onto a Si/SiO_2 substrate which had a 50 nm layer of Au on the surface. This setup allowed a bias contact washer to be clamped to the sample *ex situ* without worry of IL formation as Au is resistant to oxidation. This sample mounting scheme is shown in Figure 2.8.

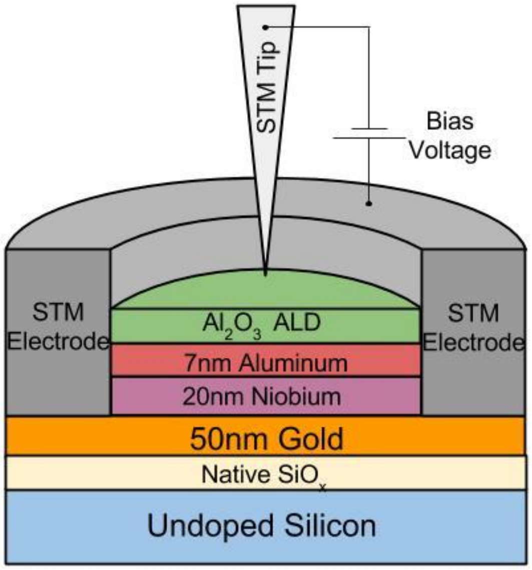

Figure 2.8: A schematic diagram is shown for the sample mounting scheme for the STS experiments.

The insulator, adds a second tunneling barrier to the electronic structure, shown in Figure 2.9a [74, 75]. The height and width of this second tunneling barrier is determined by the insulator band gap in relation to the Fermi level and the insulator thickness. Tunneling through this double barrier structure is highly dependent on the insulator barrier height and thickness. When a bias voltage is applied, the sample M-I electronic structure lowers together similarly to Figure 2.7c. When the insulator conduction band is lowered to the STM tip Fermi level, as shown in Figure 2.9b, electrons tunnel into the insulator conduction band then ballistically transport to the metal layer beneath [77]. There is substantially more tunneling current in this case. The onset of this transition is defined as the Conduction band minimum (CBM), also known as the insulator barrier height, E_b.

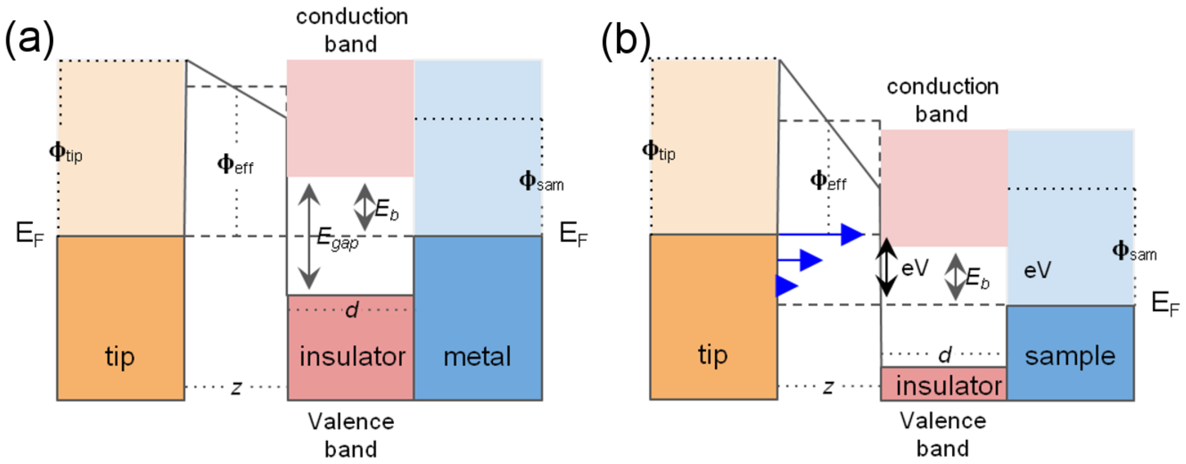

Figure 2.9: The electronic structure is shown for (a) tunneling from the STM tip through a meal-insulator structure (b) the modified structure when a bias voltage is applied to the sample.

2.5 STS *dI/dV* Measurement and Analysis

Tunneling current can also be described by the Berdeen Model. In the Energy-Dependant approximation, the tunneling current for a 1D square potential barrier is given by Eq. 2.4 [74, 78, 79].

$$I = \frac{4\pi e}{\hbar}\int_0^{eV} \rho_{tip}(E - eV)\rho_{sample}(E)T(E,V,z)\, dE \qquad \text{Eq. 2.4}$$

Where $\rho_{tip}(E - eV)$ and $\rho_{sample}(E)$ are the local density of states for the tip and sample respectively as a function of the tunneling electron energy and the transmission function is $T(E, V, z)$. The partial $(\frac{d}{dV})$ derivative of this equation can be taken. Since the majority of the tunneling current will be from electrons with energy $E = eV$ relative to the sample Fermi level (at tip Fermi level), this integral in Eq. 2.4 can be differentiated with the approximation that $E = eV$ ($dV = {}^{dE}/_{e}$) [74]. The result of this differentiation is shown in Eq. 2.5.

$$\frac{dI}{dV} \approx \frac{4\pi e^2}{\hbar} \rho_{tip}(0)\rho_{sample}(eV)T(eV, V, z) \qquad \text{Eq. 2.5}$$

dI/dV is proportional to the local density of states of the sample. Thus by measuring *dI/dV* as a function of the bias voltage, the band structure of the sample surface can probed including the insulator band gap, CBM, and the Valence Band Maximum (VBM). The advantage of using STS over tunnel junction methods such as fitting the simmonds equation [80, 81] is that STS probes the electronic structure locally as opposed over the tunnel junction area. When combined with STM imaging, individual surface species can be identified. While this level of detailed chemical identification is beyond the scope of this work, the ability to measure the ALD Al_2O_3 barrier height and band gap locally is extremely useful for our purpose of growing ALD Al_2O_3 down at the atomic scale of a single monolayer.

To experimentally measure *dI/dV*, the STM tip is first brought to within a few nanometers to a few Angstroms of the sample's surface. Our SPM system (RHK technologies) uses the beetle head design where three piezoelectric legs walk the STM tip down a precisely machined ramp on the sample stage. This type of STM has excellent mechanical stability, which is essential for vibration minimization and has excellent depth resolution on the order of 10s of picometers. Vibration isolation is critical for accurate tip-sample distance control as a small Δz oscillations lead to exponential oscillations in the tunneling current. To dampen vibrations, the SPM system was placed on an optical table with active air vibration isolation and a bellows was installed at the connection to the SPM load lock. While this setup worked fine for STS which freezes the tip-sample distance during *dI/dV* acquisition, the connection to the rest of the vacuum chamber produced too much vibration for decent, atomic-resolution STM imaging at room temperature using either a Pt-Ir or a W tip. As a result, the focus of this work was primarily STS.

dI/dV is most commonly experimentally measured using the lock-in amplifier method which can measure *dI/dV* in parallel with I-V. In the lock-in amplifier method, a small AC modulation voltage is added to the bias voltage $(V + V_M \cos \omega t)$. A Taylor expansion of the tunneling current around the bias voltage V leads to the expression in Eq. 2.6 [74].

$$I = \sum_{n=0}^{\infty} \frac{V_M^n}{n!} \frac{d^n I(V)}{dV^n} cos^n \omega t \qquad \text{Eq. 2.6}$$

Eq. 2.7 can be derived after re-arranging and neglecting a few higher order terms.

$$I \approx I(V) + V_M \cos \omega t \frac{dI(V)}{dV} + \frac{1}{4} V_M^3 \cos 2\omega t \frac{d^2 I(V)}{dV^2} + \cdots \qquad \text{Eq. 2.7}$$

The n^{th} derivative of the tunneling current is therefore proportional to the tunneling current measured at n-times the modulation frequency. If the tunneling current is multiplied by $V_M \cos n\omega t$ and integrated over time much longer than the period, the n^{th} derivative of the tunneling current can be picked out due to the orthonomality of sinusoidal functions. The result is a DC $\frac{d^n I(V)}{dV^n}$ signal. A phase shift is added to the modulation frequency to match any phase shift in the tunneling current and a low pass filter attenuates out of phase components to the signal and any remaining AC noise in the current signal. These properties give the lock-in amplifier technique an excellent signal to noise ratio compared to simple differentiation of the current which will amplify both the signal and the noise components of the signal.

2.5.1 Barrier Height Fitting using LabView

Various *dI/dV* normalization and fitting methods exist to produce a more accurate measure of the local density of states of the sample surface [82, 83]. However, these methods are less reliable for ultrathin insulators which have considerably more noise and dynamics than their metal or semiconducting counterparts. Ultrathin insulators, especially defective amorphous ones, such as thermal AlO_x have an abundance of oxygen clusters and oxygen vacancies which respond dynamically under the high local electric field generated by the STM tip. Fast switching between two states produces telegraph noise in the tunneling current. Many surface species can also lead to this noise, including hydroxyl and H_2O monomers and dimmers. Some excellent reviews on this massive topic can be found in [75, 84, 85]. In addition, dielectric breakdown of the insulator during *dI/dV* spectroscopy is a significant concern because the bias voltage produces an electric field which is typically comparable to the breakdown field of the insulator [86]. These dynamic features in the STS spectra mean that most groups who measure ultrathin insulators using STS opt for simpler, less accurate methods of analysis which better handle the noise in I-V and *dI/dV* spectra. We estimated the CBM and VBM as the intersection of two bisquare-method linear fits to ln(*dI/dV*) similar to the method reported in [87]. One line fits the band gap and the other fits the conduction band (or valence band). The endpoints for these linear fits were determined by eye as automated chi-squared minimization methods were unreliable due to occasional telegraph noise and dielectric breakdown in the STS spectra. Intelligence was required to identify noise and choice which STS spectra to analyze over that scanned spot. An example of our fit method is shown in Figure 2.10. At room temperature, STS measurements have a low energy resolution on the order of several hundred meV from both thermal broadening and the modulation amplitude of the lock-in amplifier during *dI/dV* measurement [74]. Therefore variance in the linear fit endpoints chosen by eye in the analysis, our approximation of linear *dI/dV* on the log scale, as well as our choice for which *dI/dV* spectra to analyze for that sample position produce errors on a comparable scale with this energy resolution.

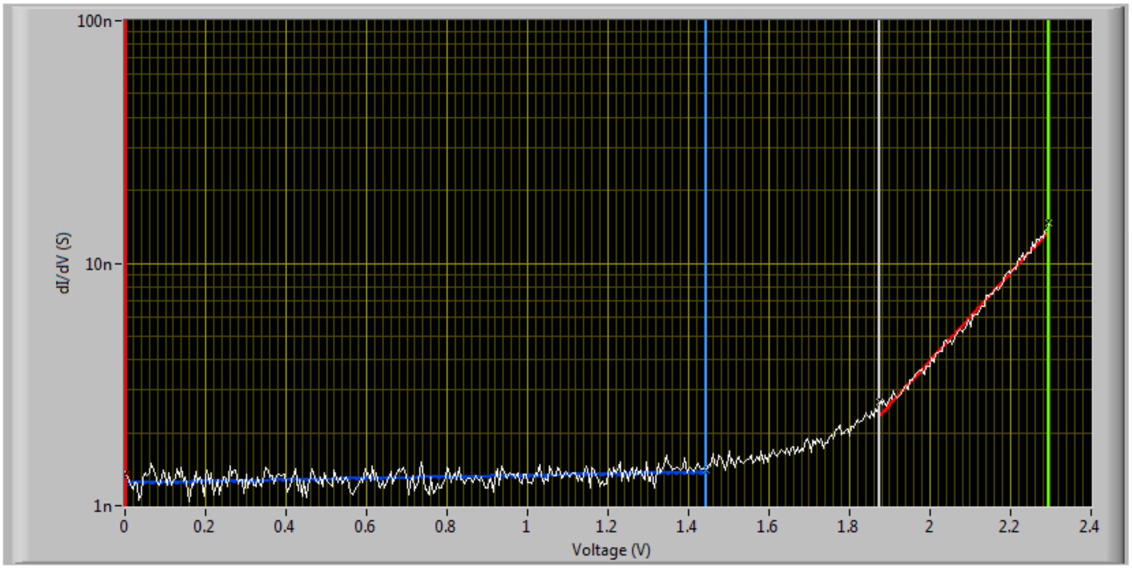

Figure 2.10: A *dI/dV* spectrum is shown for a ALD Al_2O_3 tunnel barrier on aluminum, as analyzed using a LabView program. The observed spectrum is indicated by the white trace. A band gap fit is shown by the blue line and a conduction band fit is shown by the red line. The red, blue, white, and green cursers indicate the endpoints of the fitted regions. The intersection of the two fit lines was taken as the ALD Al_2O_3 barrier height.

Approximately 50-150 locations were randomly chosen for STS measurement for each sample with a measurement separation distance greater than 100 nm. At each location, the STM tip height was stabilized with a current set point of 200 pA and a bias of typically 2 V. Then immediately after stabilization, the tip height was frozen and the bias voltage was ramped up and down 20-30 times to examine dielectric breakdown during measurement. A voltage modulation of 100 mV at 1 kHz or 30mV at 5kHz was used. After data acquisition, *dI/dV* spectra from each of the measured locations on the sample surface were analyzed.

2.6 Josephson Junction fabrication

Nb/Al/ALD-Al_2O_3/Nb and Nb/Al/AlO_x/Nb trilayers were also fabricated using our PVD-ALD system. The bottom Nb was 150 nm, and the top Nb was 50 nm in thickness. Samples with ALD tunnel barriers were transferred *in situ* to the preheated ALD chamber, and heated for 75 min under HV. After trilayer fabrication, photolithography was used to define the wiring pattern for the JJs. The diagram of the photomask is shown in Figure 2.11. The portion of the wafer which was not coated in photoresist needed to be etched to define the JJ wiring. This was achieved using Reactive Ion Etching (RIE) with SF_6 gas to etch through the top layer of Nb, a H_3PO_4 wet etch of the Al_2O_3 and Al layers, and a 2nd RIE of the bottom Nb.

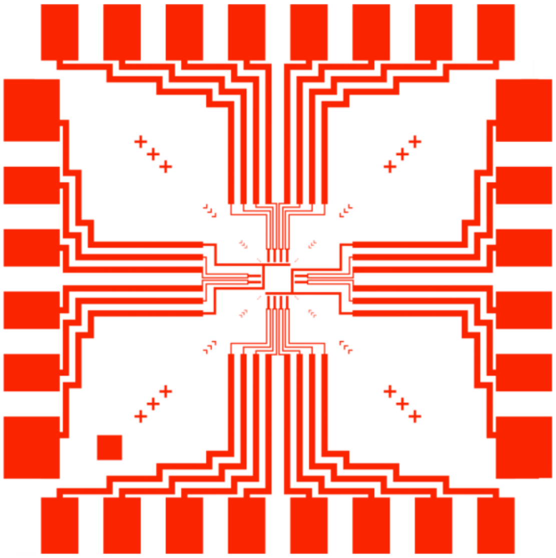

Figure 2.11: The photolithography mask is shown for the JJ device fabrication.

Next, Electron Beam lithography (EBL) defined the junction sizes which were typically 5 µm x 5 µm, 7 µm x 7 µm, and 10 µm x 10 µm. A mesa of resist was left behind with these dimensions surrounded by a square with no resist, as shown in Figure 2.12a-I. A 3rd RIE step etching through the top Nb to create the top Nb mesa (Figure 2.12a-II) and about 300 nm of SiO_2 was e-beam evaporated to electrically isolate the top of the junction (Figure 2.12a-III). The e-beam resisted was then lifted off to complete the junction definition as shown in Figure 2.12b (the green squares are the SiO_2). To connect the top contact mesa to the wiring lines, a 2nd EBL defined a square area, shown in Figure 2.12c-I. The wafer was then re-introduced to the vacuum chamber where a top 300 nm layer of Nb was sputtered after a 2 x 2min Ar plasma treatment to remove any NbO_x on the Nb mesa surface (Figure 2.12c-II). Finally, the EBL resist was removed to complete the Josephson Junctions (Figure 2.12d)

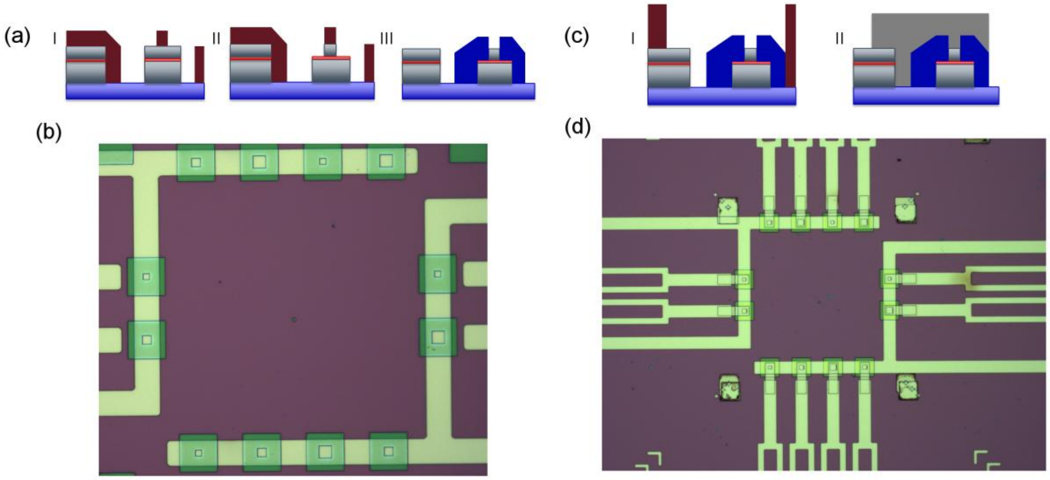

Figure 2.12: Schematic diagrams and photos are shown for the JJ device fabrication including (a-I) EBL, (a-II) RIE of the top Nb, (a-III) SiO_2 evaporation and EBL resist liftoff to define the junctions area, shown in (b). Then a (c-I)

2^{nd} EBL and (c-II) Nb deposition connected the top of the junction to the wiring layer for the (d) completion of the device fabrication.

For redundancy, after photolithography 6 subwafers were cut from the deposited trilayer. Each subwafer had 4-6 photoresist patterns. Each of those chips had 12 JJ devices with 6 devices sharing one bottom electrode contact. A probe station meassured the junction resistances at room temperature on all devices on typically 1-2 subwafers. Optical micrograph photos and resistance-area (RA) products were compared against expected or referance values to determine if there were issues in the JJ device fabrication. Chips which had JJs with the most consistant and reasonable RA values was chosen for low temperature meassurement. After dicing, the chip was glued to a chip holder and wirebonded, as shown in Figure 2.13. The JJ's I-V curve was meassured in a liquid helium dewar at a temperature of 4.2 K. Additional information on our JJ device fabrication and meassurement may be found in refs [88, 89].

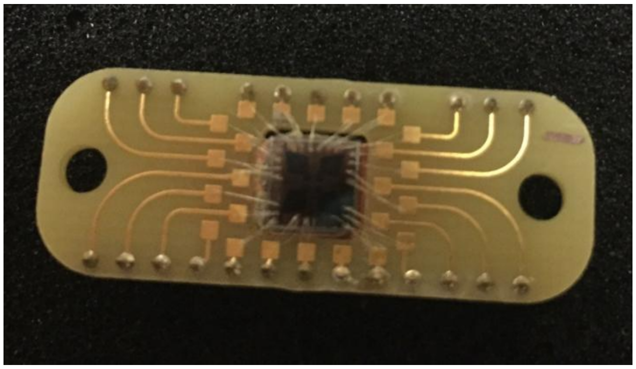

Figure 2.13: A photo is shown depicting a chip with 12 JJs which is glued to a chip holder and wired for low temperature measurement.

3 In situ ALD Al_2O_3 Growth and Nucleation on Aluminum

3.1 Chapter Overview

In this chapter, we use our method of HV, *in situ* sample transport along with a pre-ALD H_2O pulse to hydroxylate the aluminum surface in order to resolve the two issues of ALD growth for MIMTJs discussed earlier; that is, pre-ALD IL formation and ALD nucleation on metal substrates. In this proof of concept study, an atomically-thin Al_2O_3 dielectric for MIMTJ devices is realized. Interestingly, the pre-ALD heating conditions were found to have a significant impact of the quality of ALD Al_2O_3 achieved, as measured with *in situ* STS. With some preliminary optimizations, Al_2O_3 films were grown on Al with a thickness of just one ALD cycle. A high tunnel barrier height was measured which was constant with Al_2O_3 thickness, indicating that IL formation was avoided.

3.2 0 ALD cycle IL growth

While HV *in situ* sample transport should minimize the exposure of aluminum to trace gases in the vacuum chamber and hence IL formation, the sample must still bridge the temperature difference between sputtering at 10-14 ºC and ALD at roughly 200 °C. Bridging this temperature divide inevitably takes some time, during which the sample sits in the ALD chamber which has as a pressure on the order of 10^{-4}-10^{-5} Torr. Given a long exposure time at an elevated temperature, thermal oxidation of the aluminum is a possibility. To address this challenge and preliminarily address this risk of pre-ALD IL formation, the samples were inserted into a preheated ALD chamber for different times and dynamically heated to roughly 200 °C. Dynamic heating means that the sample temperature was not constant during ALD. Specifically, two dynamic heating times of 75 min and 15 min are presented to illustrate the importance of controlling this procedure in order to achieve a clean interface between the Al and ALD Al_2O_3 tunnel barrier.

To examine this possibility of pre-ALD IL formation, 0 cycle ALD samples were deposited on an Nb/Al bilayer structure and then investigated with *in situ* STS. 0 cycle means that the sample went through the entire pre-ALD heating procedure without being exposed to any ALD reactant pulses. In Figure 3.1, STS *dI/dV* spectra were taken on samples which were exposed to these two dynamic heating times without ALD. The spectrum for the 75 min heated sample (Figure 3.1a) resembles that of a highly defective tunnel barrier. In fact, it has characteristics similar to the thermal AlO_x tunnel barrier (discussed later in Figure 3.6) [90, 91]. In contrast, the spectrum for the 15 min heated sample (Figure 3.1b) closely matches the conductive spectrum measured from a calibration sample that was directly transferred to the STM chamber after Al sputtering without going through any heating (Figure 3.1b insert). Evidently, a significant amount of thermal oxidation occurred on the Aluminum surface during the extended heating time of 75 min. These spectra suggest that HV and short exposure between PVD and ALD are critical to minimize IL formation.

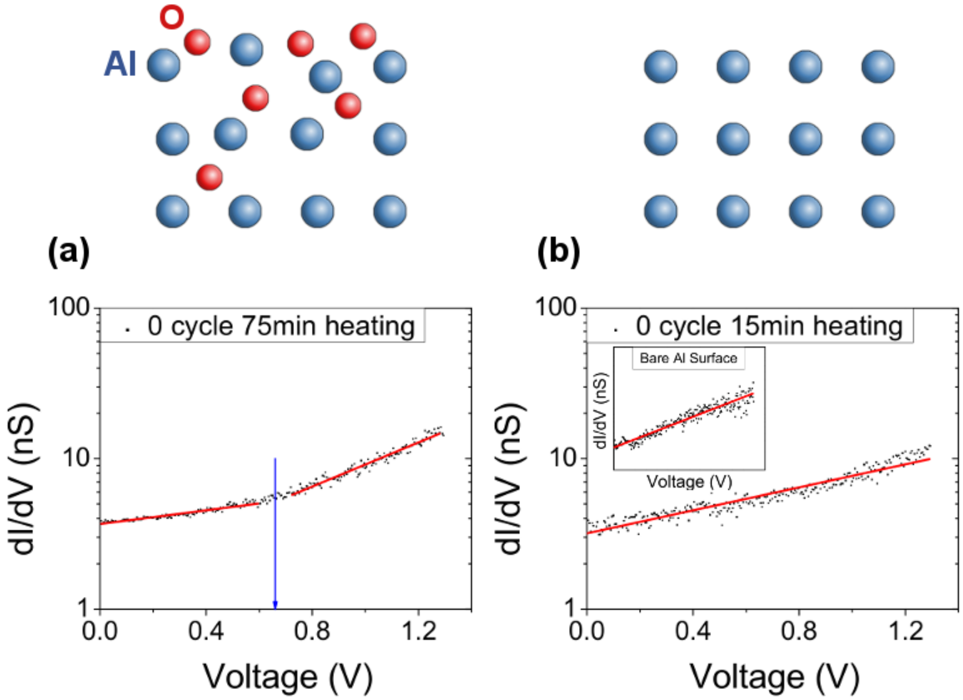

Figure 3.1: Exemplary STS *dI/dV* spectra are plotted for an Al sample after (a) 75 min heating in the ALD chamber and (b) after 15 min of heating. The arrows (blue) depict the tunnel barrier height, calculated as the intersection of the fit lines (red). Diagrams (top) illustrate the expected surface as seen by the STM tip. The insert in (b) is the *dI/dV* spectrum of a sample that was directly transferred to the STM chamber after Al sputtering.

3.3 Aluminum Surface Hydroxylation

To provide a suitable surface for ALD Al_2O_3 nucleation, the Al wetting layer was exposed to a pre-ALD H_2O pulse to create adsorbed hydroxyl molecules (OH_{ads}) on the Al surface. In order to understand the kinetics of this hydroxylation process, the behavior of adsorbed H_2O molecules on the Al surface (H_2O_{ads}) was investigated by our collaborator Ridwan Sakidja using AIMD simulations with a 2x2 supercell of face-centered cubic Al (111) under constant equilibrium volume and temperature. Bohn-Oppenheimer molecular dynamics were adopted as implemented in VASP [92, 93]. We find that when only one $\mathrm{H_2O_{ad}}$ (i.e. without $\mathrm{H_2O_{ads}}$ in proximity) is present on the Al surface, $\mathrm{H_2O_{ad}}$ dissociation into $\mathrm{OH_{ad}}$ is thermodynamically unfavorable, as shown in Figure 3.2a and Figure 3.2b. However, when multiple $\mathrm{H_2O_{ads}}$ are in close proximity, dissociation occurs after just a few ps (Figure 3.2c and Figure 3.2d). The mechanism for this process is a proton transfer between nearby $\mathrm{H_2O_{ads}}$ which creates an $\mathrm{OH_{ad}}$ and an $\mathrm{H_3O_{ad}}$. $\mathrm{H_3O_{ad}}$ dissociation into $\mathrm{H_2O_{ad}}$ and H soon follows. The, now free, H atom will leave the surface and join up with another H atom to form H_2 gas.

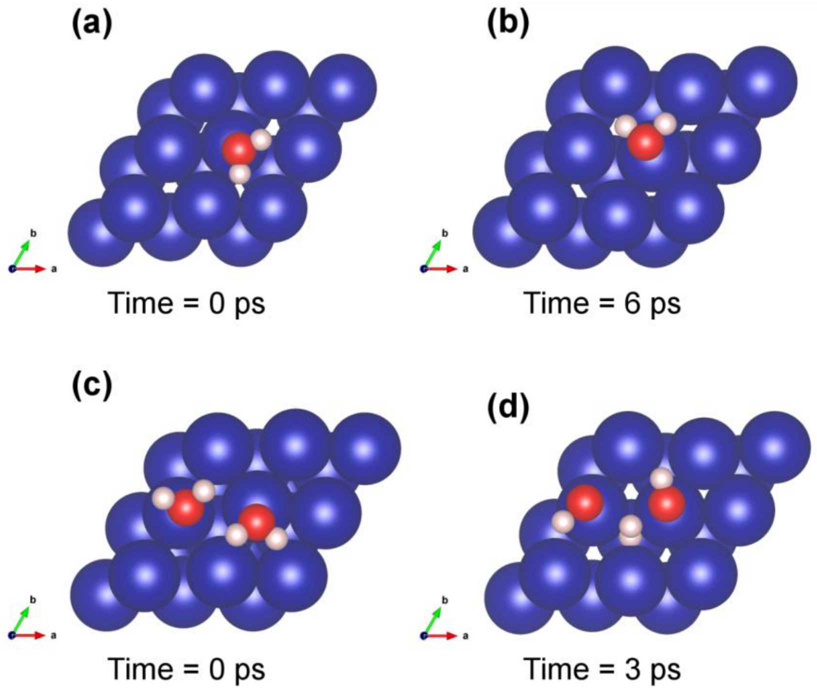

Figure 3.2: AIMD simulations are shown for H_2O adsorption onto an Al (111) surface. When only one H_2O_{ad} is present on the Al surface, dissociation is thermodynamically unfavorable (a, b). However, when H_2O_{ads} are in close proximity, dissociation into OH_{ads} and H is nearly instantaneous (c, d).

To further substantiate these AIMD simulations, the energy barrier and reaction pathways associated with this dehydrogenation process were investigated using the Climbing-Image-Nudge Elastic Band method [94] as implemented in the Quantum Espresso code [95]. The simulations employed the London dispersion correction using the vdW-DF functional of Langreth and Lundqvist [96] with a high plane wave energy cut-off of 450 eV to ensure a high precision. The electronic and ionic convergence criteria used were 10-4 eV and 10-3 eV respectively. The reaction, illustrated in Figure 3.2b, is initiated with the release of hydrogen from an adsorbed water to a nearby water molecule and is terminated with the surface diffusion of hydrogen on the Al (111) surface and eventual release as molecular hydrogen gas. Figure 3.3

shows the energy barrier plot of the transition states that were detected along this reaction pathway. This reaction is overall net exothermic, as evident by the reduction of the total energy, shown in Figure 3.3, and agrees with the AIMD simulations in that the use of saturated water offers a thermodynamic advantage. It is also quite clear from that there is an accompanying energy barrier (first peak ~ 0.5 eV) associated with this protonation reaction. This energy barrier implies that diffusion kinetics will play a role in achieving complete $\mathrm{OH}_{\mathrm{ad}}$ coverage on the Aluminum surface. It should be noted that all of the remaining transition states have either a very small energy barrier or none at all. Thus once the energy barrier for the protonation process is overcome, the remaining transition states will take place without any significant difficulty.

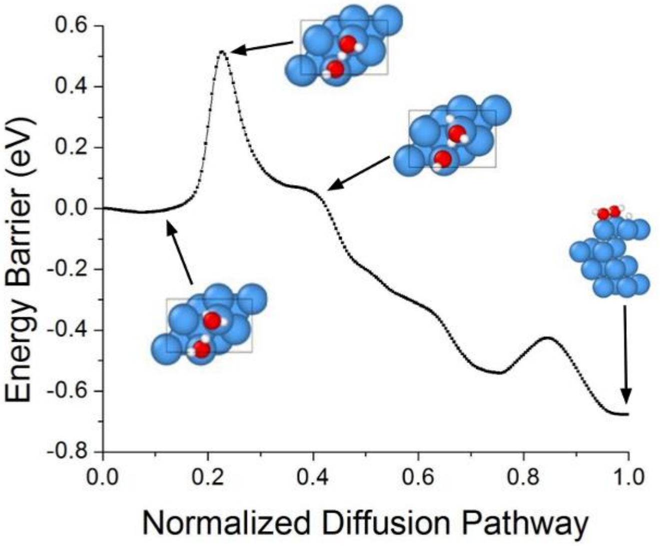

Figure 3.3: Climbing-image-nudge elastic band simulations are shown for H_2O_{ads} on an Al (111) surface. The energy barrier plot for the protonation reaction to form OH_{ads} along with AIMD snapshots depict the dehydrogenation of an H_2O_{ad} to a nearby water molecule and the surface movement of H^+ on the Al (111) surface.

In order to experimentally probe this hydroxylation process, one cycle of ALD Al_2O_3 was deposited on an Al wetting layer. Figure 3.4 depicts a representative *dI/dV* spectrum for a 1-cycle ALD Al_2O_3 tunnel barrier with an initial H_2O pulse of 2 s in duration. The insert shows the corresponding I-V curve. This *dI/dV* spectrum has a well-defined tunnel barrier an E_b, of about 1.56 eV. This spectrum indicates that an atomically-thin tunnel barrier (Figure 3.4, schematic) can be obtained using this UHV PVD-ALD approach on a clean Al wetting layer (Figure 3.1b, schematic) through careful control of the ALD growth in order to minimize IL formation (Figure 3.1a, schematic).

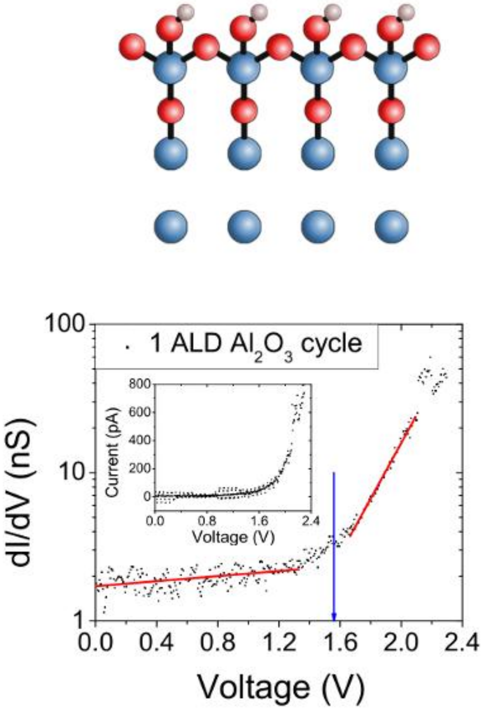

Figure 3.4: An exemplary STS *dI/dV* spectra is plotted for an Al sample after one ALD Al_2O_3 cycle. The insert is the corresponding I-V curve taken simultaneously with *dI/dV*. The arrows (blue) depict the tunnel barrier height, calculated as the intersection of the fit lines (red). Diagrams (top) illustrate the expected surface as seen by the STM tip.

The simulations in Figure 3.2 and Figure 3.3 suggest that the H_2O areal density from the H_2O pulse is crucial to facilitate an efficient hydroxylation reaction which will form a uniform monolayer of OH_{ads} on the Al surface. To investigate if this is the case, additional 1 cycle ALD Al_2O_3 samples were fabricated with a varying initial H_2O pulse duration. Figure 3.5 reveals the one-cycle ALD Al_2O_3 coverage on the Al wetting layer as the initial H_2O pulse duration was varied from 1-3 s. The ALD Al_2O_3 coverage was defined as the percentage of STS spectra, taken from random locations on the sample, which showed a sharp conduction band onset and an E_b consistent with ALD samples of higher cycle number (see Figure 3.6). The ALD Al_2O_3 surface coverage increased from ~54% at 1 s pulse duration to ~93% at 2 s duration. These experimentally observed time frames suggest that long initial H_2O pulses, on the order of seconds, are required for H_2O molecules, adsorbed to the Al surface, to reach a high enough areal molecular density for an efficient dissociation into $\mathrm{OH_{ads}}$ to occur. Interestingly, longer H_2O pulses led to a reduced ALD Al_2O_3 surface coverage. The remaining, non-ALD, spectra on the Al surface were either conductive or had very high noise and were unstable under the STM electric field. While the nature of these non-ALD, non-conductive spectra remains to be a topic of further investigation, we speculate that very long H_2O pulses may lead to H_2O clusters instead of monolayer formation on the Al surface. These clusters may possibly slow down or prohibit uniform surface hydroxylation. Additional simulations and STS experiments would be needed to confirm both the loss in ALD Al_2O_3 coverage and if H_2O clusters are the cause.

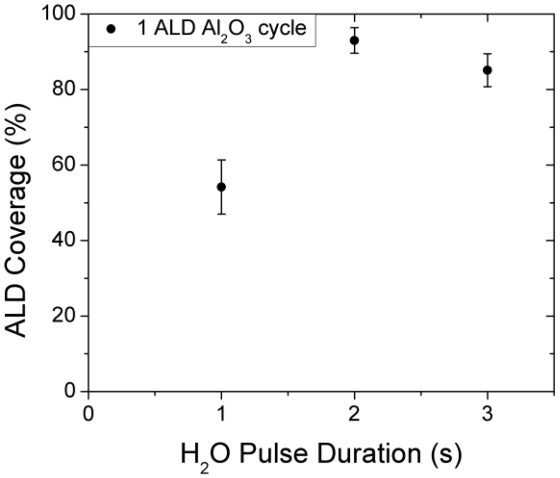

Figure 3.5: The percentage of the Al surface which had a barrier height consistent with ALD Al_2O_3 after one ALD Al_2O_3 cycle is shown verses a variable initial H_2O pulse duration.

3.4 ALD Al_2O_3 vs. Thermal AlO_x Tunnel Barriers

In addition to its paramount role in nucleation, the hydroxylation of the Al wetting layer prevents oxygen from diffusing into the Al to form an IL during the ALD process. This argument is supported by the *dI/dV* characteristics and E_b observed for the thermal AlO_x and the ALD Al_2O_3 tunnel barriers. The *dI/dV* spectra for a thermal AlO_x tunnel barrier of ~1.3 nm, in estimated thickness [41], is shown alongside a 10-cycle ALD Al_2O_3 tunnel barrier with a comparable thickness of ~1.2 nm in Figure 3.6a. The ALD Al_2O_3 spectrum has a significantly sharper conduction band onset than the thermal AlO_x spectrum, suggesting that the ALD Al_2O_3 tunnel barrier has a much more ordered and less-defective internal structure [29, 41, 90, 91]. This improved internal structure is corroborated by the higher ALD Al_2O_3 E_b shown in Figure

3.6b. Specifically, E_b values of ~1.00 eV and ~1.42 eV were observed for the ALD Al_2O_3 tunnel barriers with 75 min heating and 15 min heating respectively whereas the thermal AlO_x counterpart was just ~0.67 eV. Other groups have reported similar thermal AlO_x E_b values [41].

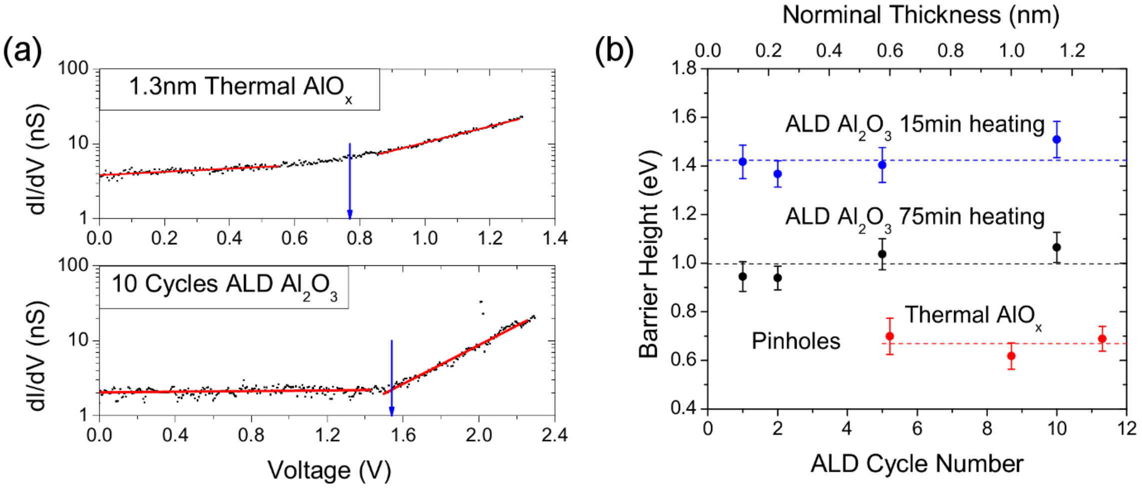

Figure 3.6: A comparative STS study of ALD Al_2O_3 vs. thermal AlO_x tunnel barriers. (a) Exemplary constant height *dI/dV* spectra were taken on a 1.3 nm thermal AlO_x tunnel barrier (top) and a 10 cycle (1.2 nm) ALD Al_2O_3 tunnel barrier (bottom) with 15 min heating. The arrows (blue) depict the tunnel barrier height calculated as the intersection of the fit lines (red). (b) The average tunnel barrier height (dashed lines) for thermal AlO_x (red) and the ALD Al_2O_3 (blue-15 min and black-75 min heating,) tunnel barriers plotted as function of tunnel barrier thickness respectively.

The ALD Al_2O_3 E_b value was maintained as the number of ALD cycles, *N*, varied from 1 to 10 (Figure 3.6b). This trend is particularly demonstrated in the ALD Al_2O_3 samples with 15 min heating (blue) and further indicates that a significant metal-insulator IL is not present-as an IL would have disproportionately affected the samples with smaller *N's* by lowering their E_b values. For the ALD Al_2O_3 samples with 75 min heating (black), an IL was confirmed by the slight E_b reduction of 0.11 eV as N was reduced to 1 and 2 from larger values. An additional effect of this IL is demonstrated by the E_b improvement as the sample heating time was reduced from 75 min (black line) to 15 min (blue line). Nevertheless, this overall ALD Al_2O_3 E_b consistency with thickness is remarkable because it illustrates that the ALD process can produce high quality Al_2O_3 down to the atomically-thin limit. In contrast, the thermal AlO_x E_b has a significant thickness dependence in the lower nominal thickness range, although a value of 0.67 eV is maintained at 0.6-1.3 nm thickness. This E_b thickness dependence is reflected by the dramatic increase in critical current density, J_c, observed in JJs with thermal AlO_x tunnel barriers as the oxygen exposure drops below ~10^3 Pa-s, or ~0.4 nm in thickness [20, 41]. Furthermore, a complete tunnel barrier is not even formed in this regime as the tunneling current is dominated by pinholes.

The band gap is another good indicator for the quality of the insulator. A representative STS *dI/dV* spectrum is shown in Figure 3.7. The band gap region of the STS *dI/dV* curve is nearly flat, indicating a low leakage current through the insulator [97]. The VBM and CBM were calculated to be about -1.0 eV and 1.6 eV respectively, giving an ALD Al_2O_3 band gap value of 2.63 eV +/- 0.30 eV. This band gap value is actually comparable to the ultrathin (1.3 nm) epitaxial Al_2O_3 band gap of 2 – 4 eV [97, 98]. What's incredible about this band gap value is that it's maintained (constant with thickness) all the way down to the atomically-thin limit of a single monolayer of Al_2O_3 (1 ALD cycle).

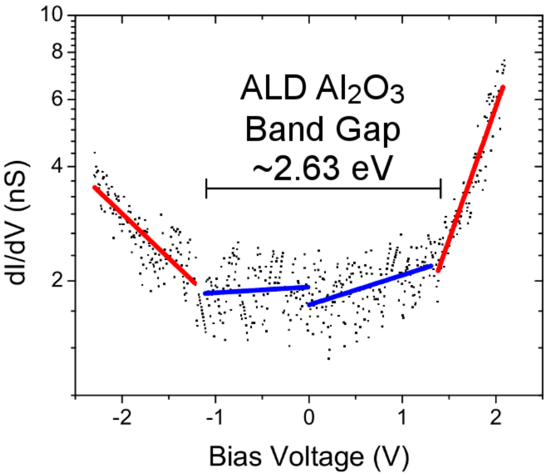

Figure 3.7: A representative *dI/dV* spectra is shown with blue fit lines to the band gap and red fit lines to the valence and conduction band. The ALD Al_2O_3 band gap was estimated using the intersection of the red and blue fit lines to calculate the VBM and CBM.

3.5 Conclusions

In summary, an *in situ* STS study has been carried out to understand the nucleation mechanisms of ALD Al_2O_3 on an Al wetting layer. We have found that a well-controlled hydroxylation of the Al wetting layer, through a carefully controlled first H_2O pulse, is the key to enable the creation of an atomically-thin ALD Al_2O_3 tunnel barrier which is of significantly higher quality than the industrial standard thermal AlO_x tunnel barrier. Specifically, the ALD Al_2O_3 tunnel barrier has a high E_b of 1.4-1.5 eV which is maintained as the barrier thickness is varied in the range of 0.12-1.2 nm. In contrast, the thermal AlO_x tunnel barrier has a low E_b of

~0.67 eV only in the barrier thickness range exceeding 0.6 nm. Furthermore, this ALD Al_2O_3 tunnel barrier has an extraordinarily high band gap of about 2.6 eV which is comparable to epitaxial Al_2O_3 ultrathin films. This result demonstrates for the first time, to our knowledge, the viability of the ALD process to create an atomically-thin Al_2O_3 tunnel barrier which has a significantly denser, less defective internal structure than thermal AlO_x-as demanded for the next generation of high performance MIMTJs.

4 Interfacial Layer Formation and it's Impact on the Tunnel Barrier

4.1 Chapter Overview

In the prior chapter we found that the quality of the Al_2O_3 is highly dependent on the sample heating conditions prior to the start of ALD. This is evidence that an IL may have formed even under HV. To be suitable for MIMTJ applications, it is critical that the IL formation mechanisms are well understood. This understanding gives critical insight to both why the tunnel barrier height increased with reduced heating time and if it can be increased further. In this work, we probe the nucleation of the first ALD Al_2O_3 monolayer on the Al wetting layer using AIMD and STS while the pre-ALD heating process was systematically varied in both heating temperature and time. This strategy is illustrated in Figure 4.1. With this knowledge gained, we optimized these heating conditions to minimize the IL growth. Finally, we examine this optimized monolayer ALD Al_2O_3 film using *in situ* STM and AFM and *ex situ* capacitance measurements to see the impact of our optimizations and determine if any IL remains.

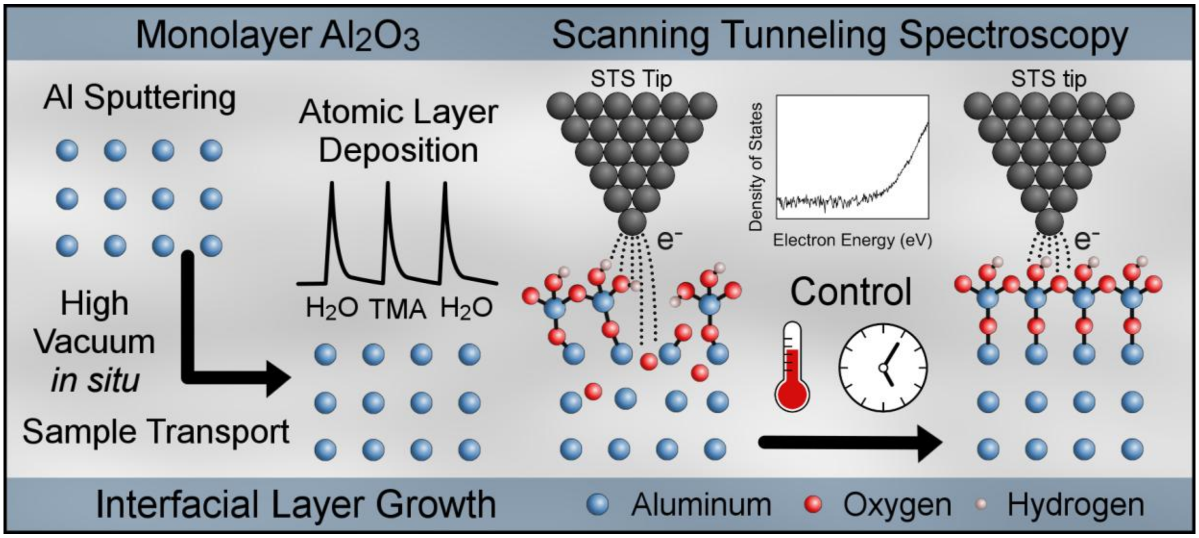

Figure 4.1: An illustration of the strategy employed in this work to study and minimize IL formation. Al was magnetron sputtered and transferred, under high vacuum, to the ALD chamber where an initial H_2O pulse hydroxylated the Al surface just prior to the ALD reactant pulses (TMA and H_2O). In situ STS studied the electron tunneling properties of the insulator to observe the significance and effect of the IL on the ALD Al_2O_3. Then with insight gained from AIMD simulations, the pre-ALD heating conditions (temperature and time) were varied to optimize ALD conditions to minimize the IL.

4.2 Thermal AlO_x IL Formation Mechanisms

Trace O_2 or H_2O originating from the ALD reactor during the pre-ALD heating step may form an IL on Al via the thermal oxidation process. To shed light on the microscopic mechanisms of this possible IL formation, a number of AIMD simulations were performed under constant temperature and volume with 1 fs for each trajectory step. Figure 4.2a-I shows the atomic trajectory of adsorbed oxygen molecules, O_{ads}, on an Al (111) surface at a temperature of 80 K (-193°C). After 1.5 ps, trace O_{ads} have distorted the topology of the Al surface lattice. The Al atoms are spontaneously “extracted” from their original surface positions, and a rough topology is created. A very similar phenomenon has been observed by a previous theoretical study [99] based on ground state Density Functional Theory calculations. Al extraction during the early stages of oxidation has been attributed to the strong propensity to form AlO_x clusters on the Al surface, whereby the Al ions spontaneously move to the center of each cluster. Our AIMD simulations demonstrate that this process can occur at a temperature as low as 80 K (-193 °C). Higher temperatures will accelerate this process. Thus it is conceivable that any trace oxygen impurities in the ALD chamber present during the pre-ALD sample heating, may initiate thermal oxidation to form an AlO_x IL.

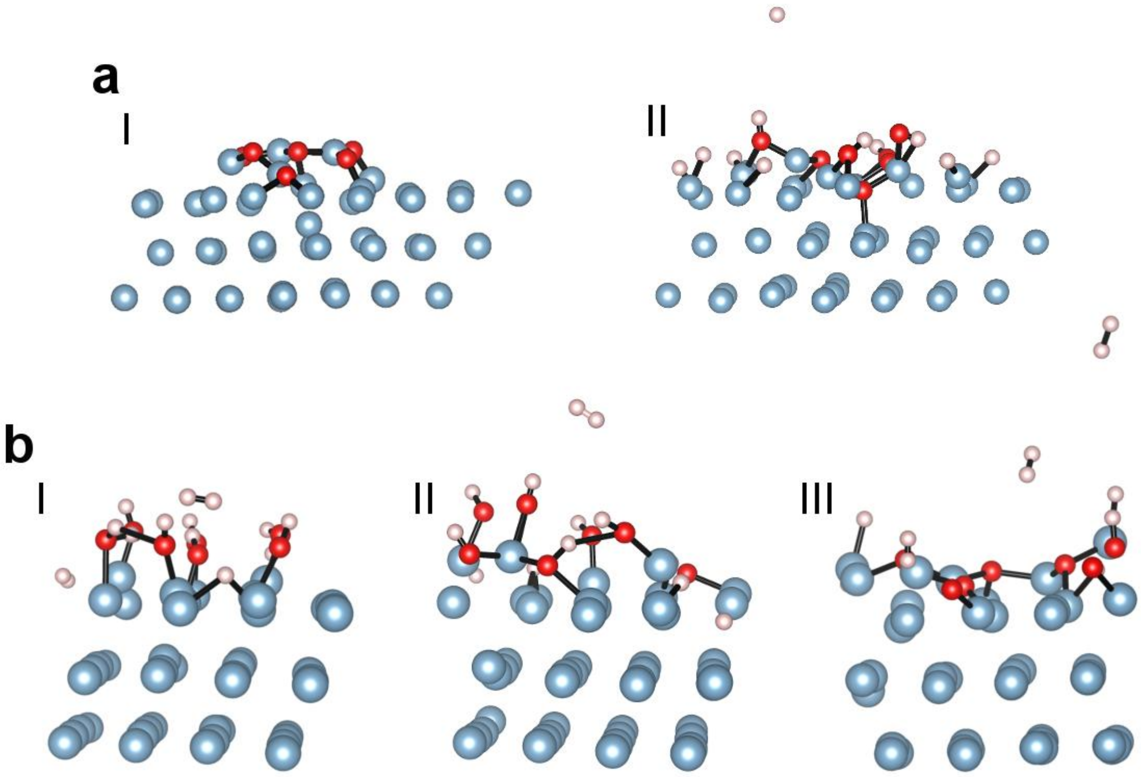

Figure 4.2: Snapshots from AIMD simulations are shown for (a) the proposed thermal AlO_x IL formation mechanisms on Al. (I) thermal oxidation from exposure to trace oxygen. The temperature was 80 K (-193 °C) and

the simulation was run for 1.5 ps. (II) thermal oxidation from exposure to H_2O and it's subsequent dissociation into O_{ads}. The temperature was 600K (327 °C) and the simulation was run for 0.5 ps. (b) a simulated H_2O pulse on the Al wetting layer. The temperature was (I) 300 K (27 °C), (II) 423 K (152 °C) and (III) 473 K (200 °C). The simulations was run for 1.5 ps, 3 ps, and 2 ps respectively. All AIMD simulations were run with 1 fs step sizes.

Aside from O_2, a thermal AlO_x IL may also form indirectly upon exposure to H_2O, originating from either the initial H_2O pulse or from trace H_2O originating in the ALD reactor during the pre-ALD sample heating. Figure 4.2a-II depicts the trajectory of H_2O_{ads} on an Al(111) surface at 600 K after only 0.5 ps. An elevated sample temperature can dissociate the resulting OH_{ads} into O_{ads} and H. The O_{ads}will oxidize the Al in a manner similar to Figure 4.2a-I. This dissociation of H_2O_{ads} into O_{ads} is quite temperature dependant, becoming more prevalent with higher temperatures. This sensitivity to temperature is demonstrated in Figure 4.2b which shows the simulated trajectories of H_2O_{ads} on Al with a temperature of 300 K (27 °C), 423 K (152 °C) and 473 K (200 °C). When the sample temperature is too low, (e.g. at 300 K shown in Figure 4.2b-I), dissociation of H_2O_{ads} into OH_{ads} does not occur efficiently so some H_2O_{ads} remain on the Al surface. When the temperature is just right (e.g. near 423 K (152 °C), shown in (Figure 4.2b-II), the majority of the H_2O_{ads} dissociate into OH_{ads} without much dissociation into O_{ads} and H. However when the temperature is too high, (e.g. near and greater than about 473 K (200 °C), shown in Figure 4.2b-III), the dissociation of H_2O_{ads} into OH_{ads}occurs with a subsequent dissociation of OH_{ads} into $O_{ads}$and H. The H leave the surface to form H_2 gas, and the O_{ads} remain behind to form a thermal AlO_x IL, as is the case of Figure 4.2a-II. This process is more clearly visualized from the isomorphic perspective at larger temperature extrema, as shown in Figure 4.3 for temperatures of 80 K (-193 °C), 473 K (200 °C), and 600 K (327 °C). Overall, these AIMD simulations suggest that the sample temperature during the pre-ALD H_2O pulse should be maintained within the range of 423-473 K (152-200 °C) to favor a hydroxylated Al surface with minimal dissociation of $\mathrm{OH_{ads}}$ into $\mathrm{O_{ads}}$.

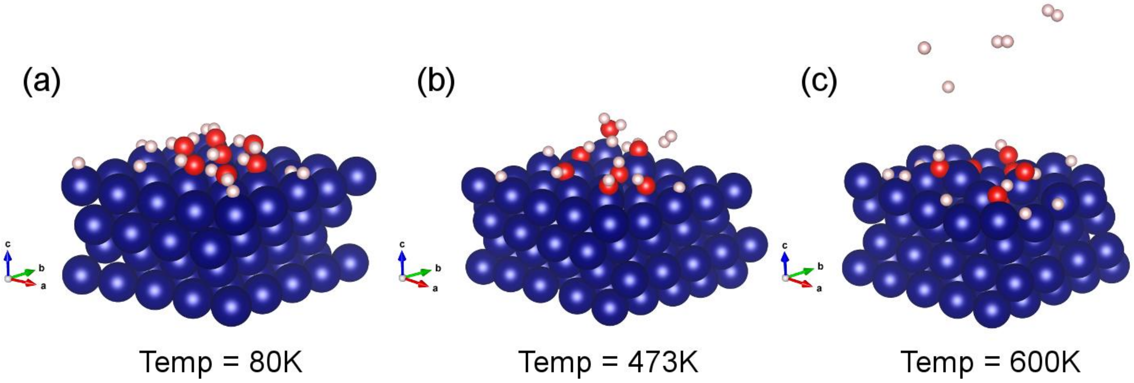

Figure 4.3: Snapshots from AIMD simulations of water molecular pools which were placed on an Al (111) surface at a temperature of (a) 80 K, (b) 473 K and (c) 600 K. These snapshots depict the simulation after 1000 steps (1ps) of run time.

4.3 How the Interfacial Layer effects ALD growth

To understand how an IL may affect the ALD Al_2O_3 growth, we first must understand the ideal case of ALD growth on a hydroxylated Al surface without an IL. In Figure 4.4, we evaluated the interaction of TMA with a hydroxylated Al (111) surface. We set up this simulation by placing a horizontally aligned TMA molecule on top of a pool of seven $\mathrm{OH_{ads}}$ on the Al (111) surface (Figure 4.4a). The first step of this TMA-OH interaction is the adsorption of the TMA's Al cation onto an $\mathrm{OH_{ad}}$. This adsorption partially elevates the hydroxylated Al surface and slightly distorts the TMA molecule with a slight change in the bond angle between the Al and the three methyl ligands. This interaction can be seen in Figure 4.4b and Figure 4.4c. Evidentially there is a strong preference for an Al-O bond. This finding is consistent with the results from a previous study on the interaction between TMA and a hydroxylated surface which found that the Al-O adsorption process has a highly energetically favorable exothermic reaction [100].

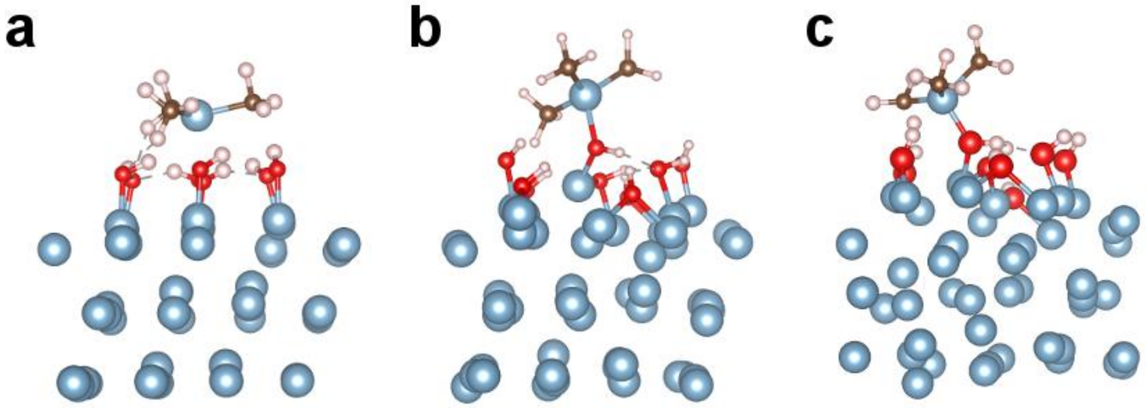

Figure 4.4: Snapshots from AIMD simulations at 432 K (159 °C) up to 7 ps (1fs for each step) are shown for (a) the initial setup of adsorbed TMA on a well-hydroxylated Al (111) surface, (b) the TMA interaction after 1ps with an $\mathrm{OH_{ad}}$, and (c) the subsequent formation of an Al-O bond and H release from an $\mathrm{OH_{ad}}$.

Throughout the AIMD simulations, we observed intermolecular hydrogen bonds present amongst the $\mathrm{OH_{ads}}$; as evident by the frequent re-alignments of the hydrogen atoms. The $\mathrm{OH_{ad}}$ intermolecular bond length laterally is quite short, in the range of 1.4 Å to 2.0 Å. A hydrogen bond between two close $\mathrm{OH_{ads}}$, results in a horizontal $\mathrm{OH_{ad}}$ alignment, shown schematically in Figure 4.5a. This horizontal alignment can only be achieved with a high surface-packing density of $\mathrm{OH_{ads}}$ on the Al (111) surface. As a consequence of this horizontal alignment, the O anion in the $\mathrm{OH_{ad}}$ is exposed towards the Al cation from the TMA. A vertically-aligned $\mathrm{OH_{ad}}$, on the other hand (Figure 4.5b), has significant steric hindrance for TMA adsorption onto the $\mathrm{OH_{ad}}$ (Figure 4.4). Thus horizontal alignment of the $\mathrm{OH_{ads}}$ is critical to enable an efficient TMA adsorption on the hydroxylated Al wetting layer. While it has been well-established that ALD reactions, particularly with respect to TMA are self-terminating, that is *not* the case for the hydroxylation process of the Al (111) surface. It is hence reasonable to assume that rougher Al surface topology, created by the ingress of oxygen from a thermal AlO_x IL, would lead to a reduced $\mathrm{OH_{ad}}$ surface density. The additional steric hindrance from the resulting vertically aligned $\mathrm{OH_{ads}}$ will likely lead to a reduced TMA density in the first ALD cycle which will, in turn, lead to defects in the ALD Al_2O_3 tunnel barrier.

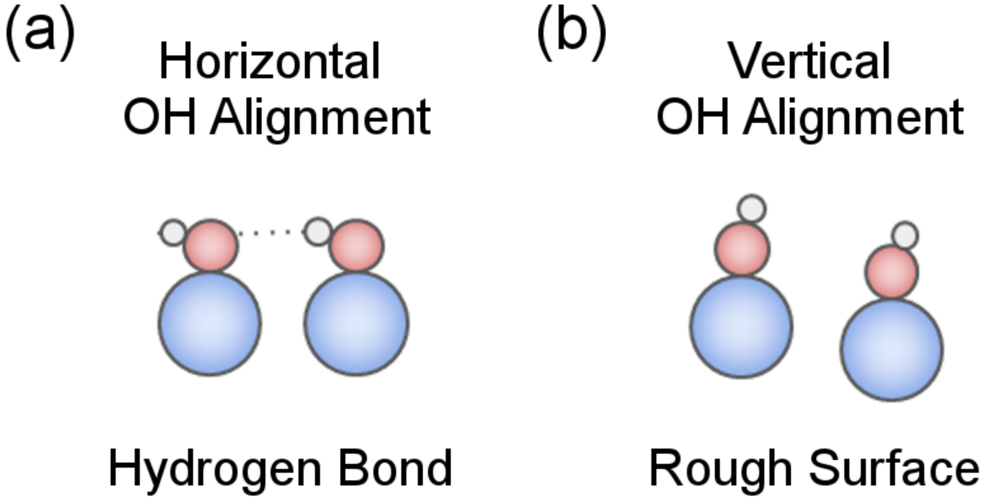

Figure 4.5: A simple illustration is shown for our definition of horizontal and vertical $\mathrm{OH_{ad}}$ alignment. (a) When two $\mathrm{OH_{ads}}$ are in close proximity, a Hydrogen bound forms between the two Hydrogen atoms, constraining them horizontally. (b) If the two $\mathrm{OH_{ads}}$ are too far away than a hydrogen bond will not form and the Hydrogen molecule in the $\mathrm{OH_{ad}}$ will be free to move about, hindering TMA adsorption.

To look beyond the initial TMA adsorption, we ran further AIMD simulations that depict the release of CH_4 from the TMA molecule following the reaction shown in Eq. 4.1.

$$\|\text{-OH} + \|\text{-O-Al-}(CH_3)_3 \rightarrow \|\text{-O} + \|\text{-O-Al}(CH_3)_2 + CH_4(g) \qquad \text{Eq. 4.1}$$

where ||-OH stands for hydroxylated Al (111) surface and ||-O-Al-$(CH_3)_3$ is the adsorbed TMA with the reaction yielding the adsorbed dimethylaluminium or ||-O-Al$(CH_3)_2$ and the methane gas CH_4(g). AIMD snapshots for the simulation at 432K (159°C) are shown in Figure 4.6. A previous theoretical work has shown that the first CH_4 dissociation process is characterized by an activation energy in the range of 0.35-0.9 eV [100, 101]. This wide range of energy is due to the varying degree of steric hindrance for the protonation onto the methyl ligands.

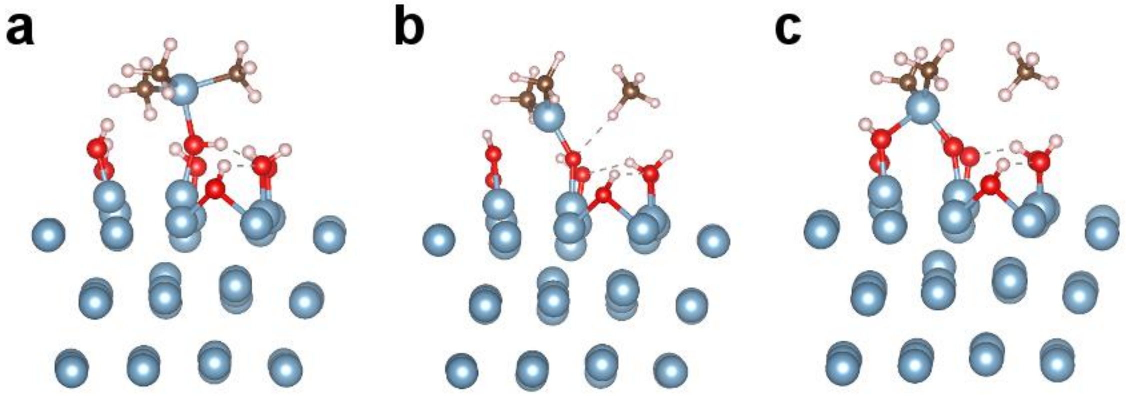

Figure 4.6: Snapshots from AIMD simulations at 432 K (159 °C) up to 7 ps (1fs for each step) are shown for the reactions of the attached TMA molecule on the hydroxylated Al surface; including the (a) initial simulation setup, (b) the proton exchange between nearby $\mathrm{OH_{ads}}$ and one of the CH_3 groups of the TMA, and (c) the final release of the CH_4 molecule.

To examine the energetics of this first CH_4 dissociation on the hydroxylated aluminum surface, Nudged Elastic Band (NEB) analysis was used using the methods outlined in [102-105]. The Transition State Tools (TST) for VASP [101, 105, 106] were also used to generate a total of 13 images depicting the reaction. For a comparison, this same reaction was examined for the hydroxylated alumina surface. The overall reaction on hydroxylated Al is exothermic and similar to those observed one the alumina substrate. The dH value (-1.9 eV) is higher than those reported for alumina substrate (-1.2 eV to -0.7 eV) suggesting that the reaction on hydroxylated Al is more favorable. A closer examination on the the last part of the reaction based on our NEB analysis in Figure 4.7 shows that the remaining dimethylaluminium forms a new bond with the oxygen as a result of the release of CH_4 gas (see arrow). This is not the case with that of Dimethylaluminum in the case of alumina. We postulate that this additional chemical bond adds more thermodynamic stability to the final configuration and thus leads to a more negative enthalpy. A further detailed study is certainly warranted to fully assess the comparison between the hydroxylated Al and the alumina substrate. This analysis however, is predicated upon a simplistic assumption that there are always going to be nearby hydrogen atoms on the hydroxylated Al surfaces to remove the CH_3 ligand. We expect that the presence of an IL will make this reaction more difficult due a distorted Al lattice and low $\mathrm{OH}_{\mathrm{ad}}$ density on the surface.

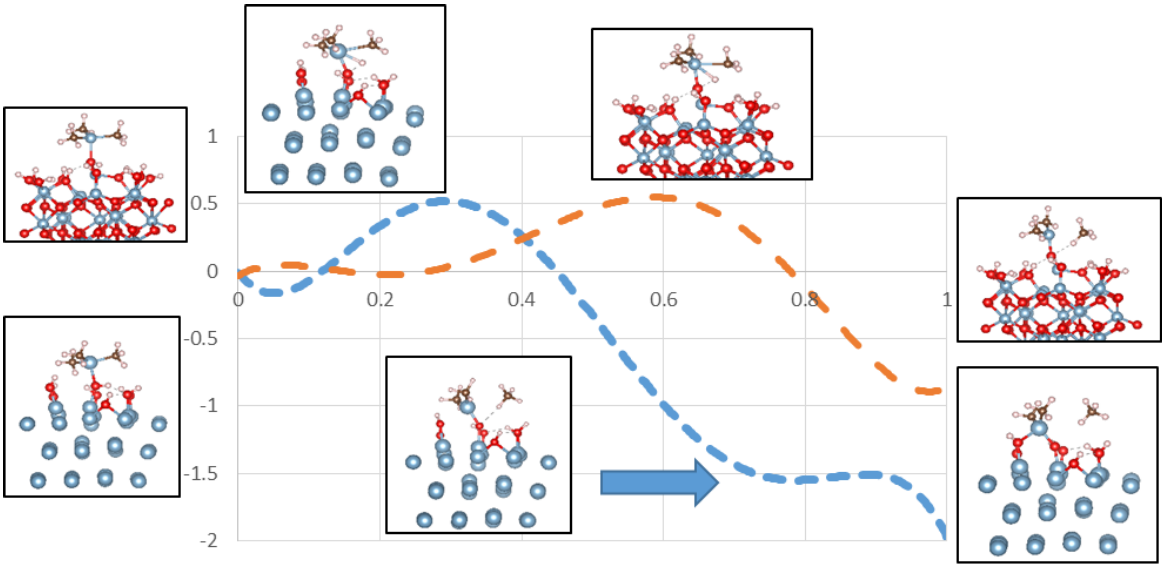

Figure 4.7: Plot of the minimum energy path associated with the release of methane gas based of NEB analysis using 13 images.

The possible impact of the IL on the quality of the ALD Al_2O_3 tunnel barriers is schematically illustrated in Figure 4.8. As we have discussed in Figure 4.4 and Figure 4.6, the defective structure of an IL may perturb the hydroxylated surface sufficiently to impair TMA nucleation and the overall ALD Al_2O_3 growth (Figure 4.8a). Gaps in the TMA coverage due to steric hindrance from an AlO_x IL may lead to pinholes or localized locations of low quality alumina (Figure 4.8a-I). Eventually, once the initial alumina layer is established, the ALD process should proceed normally Figure 4.8a-II). This means that in order to achieve a high-quality ALD Al_2O_3 tunnel barrier with atomic-scale thickness precision, as depicted Figure 4.8b, it is crucial that the IL is eliminated through precise control of the pre-ALD heating conditions to avoid defective ALD Al_2O_3 growth on an IL. Without an IL, the Al_2O_3 density and resulting tunnel barrier quality should be constant with ALD cycle number from one ALD cycle (Figure 4.8b-I) to any number of ALD cycles Figure 4.8b-II.

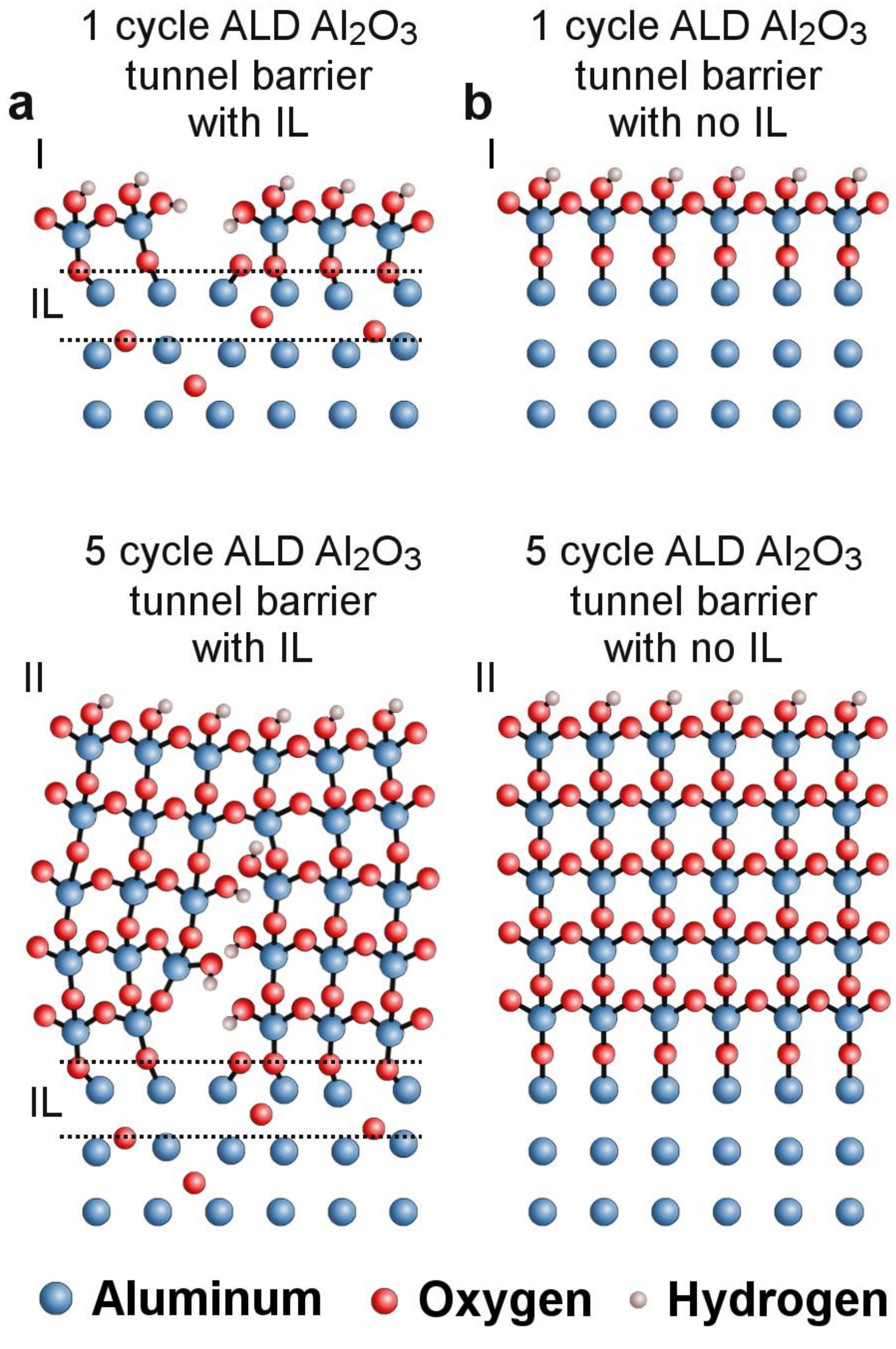

Figure 4.8: A simple two-dimensional illustrative diagram of the hypothetical internal structure for (a) an amorphous ALD Al_2O_3 tunnel barrier with an IL which is (I) 1 ALD cycle and (II) 5 ALD cycles in thickness and (b) a ALD Al_2O_3 tunnel barrier without an IL which is (I) 1 ALD cycle and (II) 5 ALD cycles in thickness.

4.4 Dynamic Heating Method

Based on these simulations, it is clear that the thermal budget of ALD must be controlled in order to minimize the Al surface's exposure to $\mathrm{O_{ads}}$. This exposure is especially critical to ALD Al_2O_3 growth during the first ALD cycle as any disruption to TMA nucleation will prevent full Al_2O_3 coverage on the Al (Figure 4.8a-I). To understand the effect of the heating parameters (temperature and time) on the tunnel barrier quality, we developed a dynamic pre-ALD heating strategy which allowed us to probe both parameters independently. Figure 4.9a shows the sample's temperature as a function of exposure time in a preheated ALD reaction chamber. Three different blackbody heater powers for the ALD chamber were explored in this dynamic heating strategy: 156 W, 220 W, and 304 W. As our ALD reactor is cylindrically shaped [71], a little under half of this wattage was directed inwards towards the sample. Fits to the data of the form given in Eq. 4.2 found the sample's steady-state temperature to be 187 °C, 220 °C, and 267 °C as time, t, goes to infinity and the time constant, τ, was 17.2 min, 15.0 min, and 12.6 min for the three powers respectively.

$$T(t) = T_i + (T_f - T_i)(1 - e^{-t/\tau}) \qquad \text{Eq. 4.2}$$

where T_i is the sample temperature prior to heating and T_f is the steady-state temperature. As expected, increasing the blackbody heater power led to a significantly reduced τ and an increased T_f. This dynamic heating strategy has the advantage of bringing the sample's temperature to the ALD suitable window quickly at the expense of a non-constant temperature during ALD. Depending on the heater power and time position on Figure 5a, the sample temperature can change at a rate as high as 10 °C/min. Thus this dynamic heating strategy is best suited for growth of the ALD tunnel barriers of only a few Å thick so the growth can be completed within a few minutes.

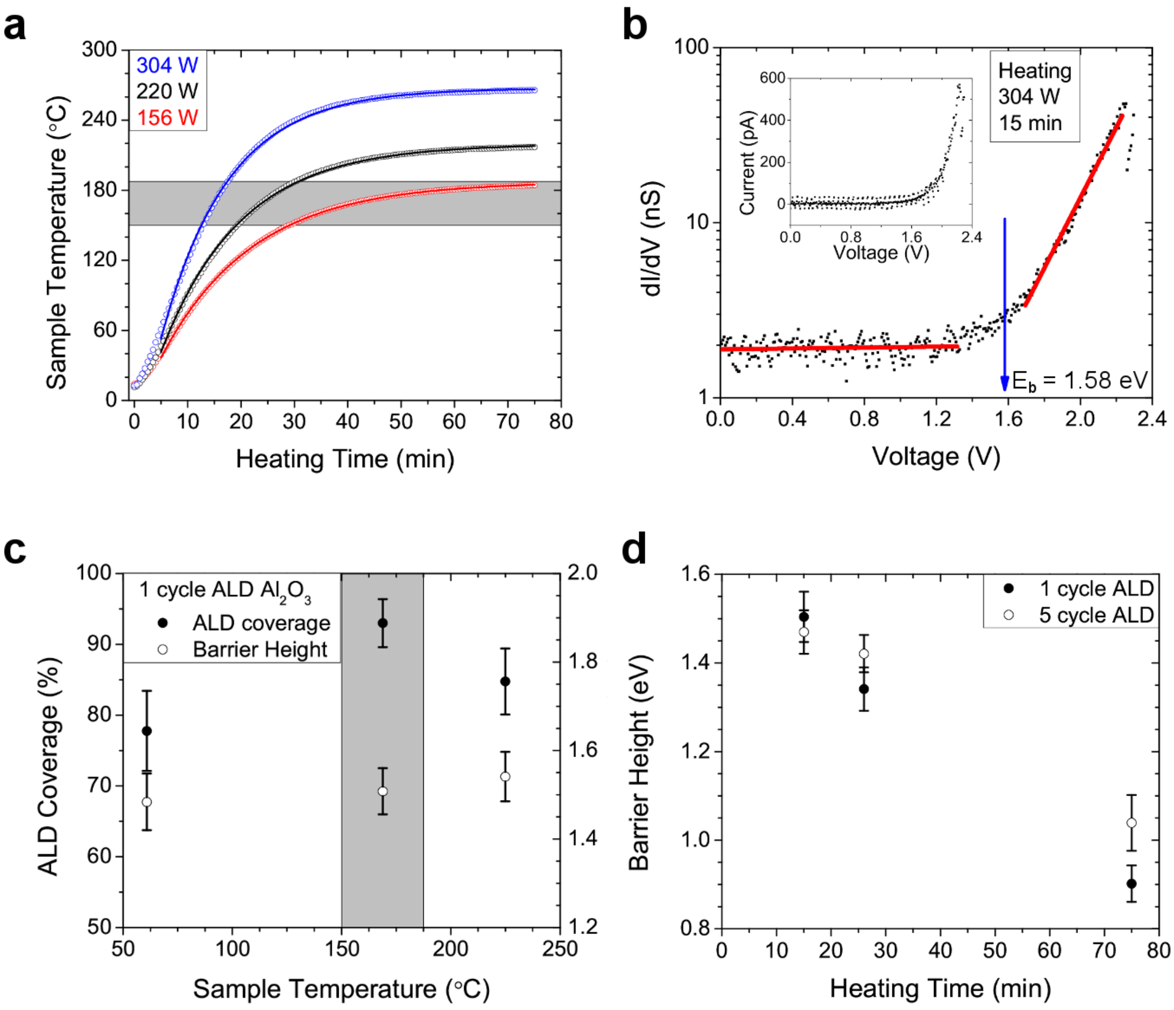

Figure 4.9: *dI/dV* STS spectroscopy and the optimization of the heating conditions for the ALD Al_2O_3 process in order to minimize the formation of an IL. (a) The measured Sample temperature is shown as a function of exposure time in an ALD reaction chamber which has been preheated at the given wattages. The solid lines are fits to the data. (b) A Representative *dI/dV* spectra and corresponding I-V spectra (insert) is shown for a 1 cycle ALD Al_2O_3 tunnel barrier. The barrier height, denoted by the position of the blue arrow, was determined by the intersection of two linear fits (shown in red) for the band gap and conduction band respectively. (c) The ALD Al_2O_3 Coverage on the Al surface is shown for a 1 cycle of ALD Al_2O_3 tunnel barrier as a function of the sample temperature during the start of ALD (solid circles). The corresponding barrier heights are shown with the open circles. The grayed out Area in (c) and (a) is a rough estimate for the ideal temperature window required to have high ALD surface coverage on

the Al after only 1 ALD cycle. (d) The measured Barrier heights are shown for both 1 cycle and 5 cycle ALD samples as function of heating time. All samples were within the temperature window from (c).

4.5 The Effect of the IL on Tunneling

The quality of the ALD Al_2O_3 tunnel barriers grown using this dynamic heating strategy was studied using *in situ* STS on 1 cycle ALD Al_2O_3 tunnel barriers. A representative *dI/dV* and I-V STS spectra is shown in Figure 4.9b for a 1 cycle ALD Al_2O_3 tunnel barrier that was heated for 15 min at a power of 304 W to a temperature of about 169 °C. The E_b from Figure 4.9b was 1.58 eV which is typical for our ALD Al_2O_3 tunnel barriers with values in the range of 1.0-1.6 eV. The ALD Al_2O_3 coverage was then estimated as the percent of STS spectra which showed evidence of a tunnel barrier with an $E_b > 1$ eV and is shown in Figure 4.9c. E_b values less than 1 eV were considered to be thermal AlO_x or pinholes. The average ALD Al_2O_3 E_b was constant with temperature with an average value of about 1.5 eV. Interestingly there is a maximum of ALD coverage with a value of about 93 % in Figure 4.9c for temperatures between 150 °C and 190 °C. This temperature range, noted with a grey box in Figure 4.9c and Figure 4.9a, roughly corresponds to the ideal temperature range for the hydroxylation of the Al wetting layer using the pre-ALD H_2O pulse and matches the results from our AIMD simulations earlier in Figure 4.2b. In the lower temperature range of 60-150 °C, the ALD coverage drops down to ~78%. Although we did not fully exhaust the reaction sequences between TMA and $\mathrm{H_2O_{ads}}$ on the Al surface, we postulate that the TMA did not nucleate successfully on areas of the Al surface which were covered by the water molecules. As a result of poor or no TMA nucleation, Al_2O_3 did not grow. However when the TMA does find $\mathrm{OH_{ads}}$ on an Al surface, it nucleates and the tunnel barrier is still of high quality (high E_b). In the higher temperature range of 190-225 °C, the ALD coverage reduces to ~85 %. One explanation for this drop in coverage may be that some $\mathrm{OH_{ads}}$ have dissociated into $\mathrm{O_{ads}}$ and H. A slight thermal AlO_x IL may result. As already discussed in Figure 4.2 and Figure 4.4, this thin IL will provide additional steric hindrance for TMA nucleation, accounting for the drop in coverage. However, this dissociation of $\mathrm{OH_{ads}}$ must not be too severe as E_b did not decrease in this temperature range.

In Figure 4.9d, E_b was measured for both 1 cycle ALD Al_2O_3 and 5 cycle ALD Al_2O_3 tunnel barriers as a function of heating time with temperatures within the ideal window from Figure 4.9c. The three heating powers of 156 W, 220 W, and 304 W were used for heating times 75 min, 26 min, and 15 min respectively. The ALD coverage was constant with sample heating time with values greater than 90%. Due to it's thicknesses relative to any IL, 1 cycle ALD Al_2O_3 tunnel barriers are affected more significantly by an IL than 5 cycle ALD Al_2O_3 tunnel barriers. Thus, assuming a defective IL with a low E_b, such as thermal AlO_x, the value of E_b can be correlated with the presence of an IL. The 1 cycle ALD Al_2O_3 E_b values in Figure 4.9d drop at a roughly linear rate of about 10 meV/min, from a value of about 1.5 eV to 0.9 eV, over the course of one hour of extra heating (15 min to 75 min). This confirms our earlier suspicion in Figure 3.6 that the IL in our ALD Al_2O_3 tunnel barriers grows thicker with increased pre-ALD exposure time through exposure to trace O_2 or H_2O at elevated temperatures.

When these tunnel barriers are grown thicker, the contribution of the IL to tunneling reduces. Therefore at 5 cycles ALD (~0.6 nm) in thickness, the STS dI/dV spectra are primarily probing the Al_2O_3 density rather than the disorder at the Al-Al_2O_3 interface. As can be seen in Figure

4.9d, the 5 cycle ALD Al_2O_3 E_b did not decrease significantly between 15 min and 26 min heating in the ALD chamber with a rate of only -4.5 meV/min. However between 26 min and 75 min heating, this rate was about -7.8meV/min. Evidently, there must have been some IL that formed, during the long heating time of 75 min that was significant enough to impact the overall ALD Al_2O_3 growth and density similar to the schematic in Figure 4.8a-II. This trend of IL formation is also evident in the E_b differences between 1 and 5 ALD Al_2O_3 cycles for these three heating times. When only heated for 15 min, the 1 cycle ALD E_b was about the same as the corresponding 5 cycle ALD E_b. Beyond 15 min heating, the 1 cycle ALD Al_2O_3 E_b was consistently lower than the corresponding 5-cycle ALD Al_2O_3 E_b. The constancy of E_b with Al_2O_3 thickness when the sample was only heated for 15min prior to ALD implies that the IL may be negligibly small for these samples. Shortening the heating time further may improve E_b slightly although it's unlikely to increase E_b more than a factor of about 10%. This possible minor E_b improvement is likely insufficient to warrant the engineering efforts required to heat large wafers for MIMTJs through a temperature differential of about 150 °C in only a few minutes.

4.6 Dielectric Breakdown

The behavior of tunnel barriers under intense dielectric stress (>10 MV/cm) can provide additional insights as to the nature and significance of the IL. Dielectric breakdown (BD) may be initiated by the high local electric field generated by the STS tip as the bias voltage is ramped up and down many times during subsequent *dI/dV* spectra. Figure 4.10 shows representative BD behavior observed for three insulating tunnel barriers. That is, a thermally oxidized AlO_x tunnel barrier which was about 0.3 nm in thickness (Figure 4.10a), a 1-cycle ALD Al_2O_3 tunnel barrier which was heated for 75 min (Figure 4.10b), and a 1-cycle ALD Al_2O_3 tunnel barrier which was heated for 15 min (Figure 4.10c). As we can observe in Figure 4.10a, thermal AlO_x breaks down under the STM tip in a gradual, soft manner as disorder increases within the tunnel barrier through defect migration. Eventually the STS spectrum becomes linear (metallic) [86, 90, 91, 107-109]. Interestingly, this soft BD was also observed in the 1-cycle ALD Al_2O_3 tunnel barrier which was heated for 75 min. (with an AlO_x IL). Although this spectra (Figure 4.10b) does not show complete soft BD, the zero voltage conductance, defined as the slope of the *dI/dV* spectra in the band gap regime, did increase with subsequent spectra similar to the case of thermal AlO_x (Figure 4.10a). This soft BD behavior observed for 1 cycle ALD Al_2O_3 with 75 min heating indicates that defects are present within the tunnel barrier and/or at the M-I interface.

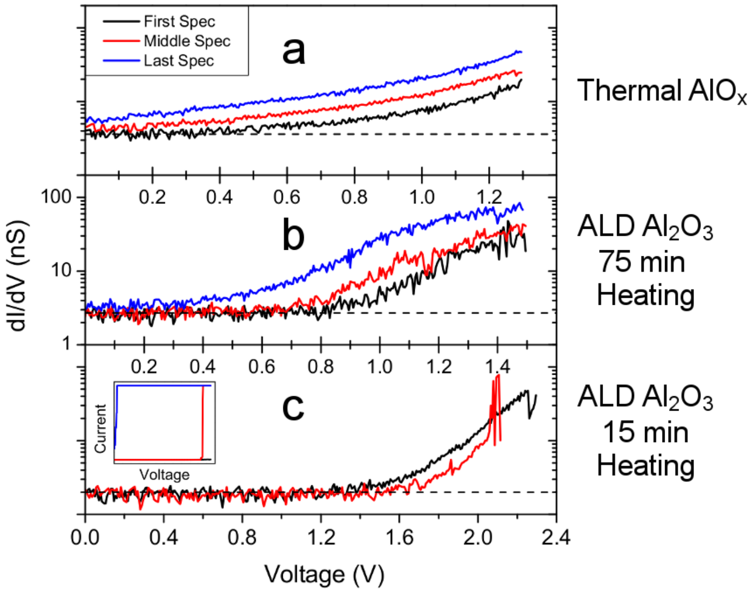

Figure 4.10: Representative STS *dI/dV* spectra are shown to illustrate the type of breakdown behavior observed. The types of dielectric breakdown behavior observed as the STM bias voltage is ramped up and down are shown for (top) the thermal $AlO_{x,}$ tunnel barrier (middle) a 1-cycle ALD Al_2O_3 tunnel barrier which was headed for 75 min, and (bottom) a 1-cycle ALD Al_2O_3 tunnel barrier which was heated for 15 min. The insert shows the I-V curve for a hard breakdown event (bottom).

When there was not a significant IL present in the ALD Al_2O_3 tunnel barrier, hard BD was observed. As shown in Figure 4.10c, there was a massive, sudden increase in the tunneling current (Figure 4.10c insert). After this traumatic BD event, the insulator becomes metallic with linear STS spectra. This form of dielectric BD is typical for crystalline insulators (>10s of nm thick) in capacitors [110]. In the ultrathin regime of 1-2 nm, hard BD is primarily observed by STS for epitaxial Al_2O_3 [86]. Rather than gradual defect migration within the barrier, hard BD represents the breaking of the Al_2O_3 bonds in the insulator [111]. Therefore, the presence of hard BD in our 1-cycle ALD Al_2O_3 tunnel barriers in Figure 4.10c confirms a low-defect atomically thin Al_2O_3 tunnel barrier which does not have a significant IL.

Finally, while it is difficult to calculate the magnitude of the breakdown field using STM (as the tip-sample distance is difficult to determine without crashing the tip), we can estimate the rough bounds for this breakdown field. Hard BD events typically occurred around 2 V in STS spectra for 1-cycle ALD Al_2O_3 tunnel barriers with 15 min heating. The thickness of this Al_2O_3 is expected to be 1.1-1.2 Å. If the tip-sample distance is estimated as somewhere between 1 Å and 1 nm, then the breakdown field is on the order of 16-100 MV/cm. This estimated breakdown field is rather high, considering that epitaxial Al_2O_3 has a value of about 11 MV/cm [86]. However, this large breakdown field is consistent with MIMTJ measurements for ALD Al_2O_3 on GaAr [112], suggesting that ALD Al_2O_3 tunnel barriers are significantly more robust than their thermal AlO_x counterparts.

To confirm this high breakdown field, capacitors with ALD Al_2O_3 tunnel barriers were fabricated with thicknesses in the range of 1.1-4.4 nm (10-40 ALD cycles). These Al_2O_3 tunnel barriers were fabricated with the optimal heating settings. In Figure 4.11, the measured breakdown field is shown versus the thickness of the Al_2O_3. The breakdown field was calculated as the voltage in which hard breakdown was observed divided by the expected Al_2O_3 thickness. Only one device per thickness was chosen for breakdown measurement. These breakdown field values agree well with our estimate from STS. A sudden rise in the breakdown field occurs as the Al_2O_3 thickness is reduced below about 2 nm. This increased breakdown field is due to an increased contribution of tunneling current to the total current, which reduces the number of ballistic collisions and therefore heating within the insulator [112, 113]. Overall, this resilience to dielectric stress may in turn lead to higher MIMTJ yields per wafer and can possibly allow for reduced gate dielectric thicknesses in CMOS devices [114].

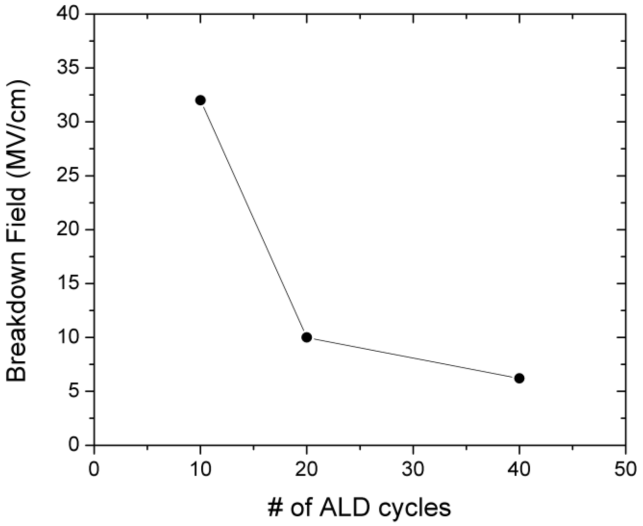

Figure 4.11: The Al_2O_3 dielectric breakdown field is shown as a function of the number of ALD cycles. The line is to guide the eye.

4.7 The ALD Al_2O_3 Dielectric constant

In addition to band gap, barrier height, and breakdown field, the dielectric constant is an important parameter for the quantification of the insulator quality. The dielectric constant of the ALD Al_2O_3 tunnel barrier was investigated using ex situ capacitance-voltage (C-V) characterization. The dielectric constant is particularly sensitive to the presence of an IL because an IL will have a capacitance in series with the Al_2O_3 capacitance. The dielectric constant can be calculated using the capacitance (C), junction area (A), and dielectric thickness (*t)* in Eq. 4.3.

$$\varepsilon_r = \frac{Ct}{\varepsilon_o A} \qquad \text{Eq. 4.3}$$

ε_o is the permittivity of free space. The measured dielectric constant of Al_2O_3 is known to reduce significantly as the insulator thickness approaches the ultrathin regime due to (1) quantum tunneling which increases the capacitor leakage current, lowering the capacitance and dielectric constant and (2) the contribution from a defective IL which contributes a small capacitance in series with the insulator capacitance. Case (2) is typically the most significant reason for the reduction in ε_r. The reason for this can be seen in Eq. 4.4.

$$\frac{1}{C_T} = \frac{1}{C_{ALD}} + \frac{1}{C_{IL}} \qquad \text{Eq. 4.4}$$

The total capacitance, C_T, will be strongly influenced by the presence of a small IL capacitance, C_{IL}, which can dominate over a large ALD Al_2O_3 capacitance, C_{ALD}. This property makes the dielectric constant an excellent parameter to examine the significance of the IL.

Figure 4.12a compares the calculated ε_r of the ALD Al_2O_3 films made with the optimal ALD and non-optimal conditions (15 min heat at 304 W and 75 min heat at 156 W) described earlier in Figure 4.9. ε_r was only 2.5-3.3 for 4.4 nm of Al_2O_3 deposited under non-optimal ALD heating conditions, whereas with optimal conditions ε_r was about 8.9. This difference in dielectric constant clearly illustrates the importance of controlling the IL. With optimal conditions, ε_r is remarkably high for ALD Al_2O_3 in this thickness range. For reference, the bulk Al_2O_3 dielectric constant is only 3% higher with a value of 9.2. Dielectric constants for ALD Al_2O_3 are typically 7-8.5 but usually only with thicknesses exceeding 40 nm [115-120]. This reported ε_r of 8.9 is higher than the previously reported highest value of 4 for a 3-4 nm ALD Al_2O_3 film [69].

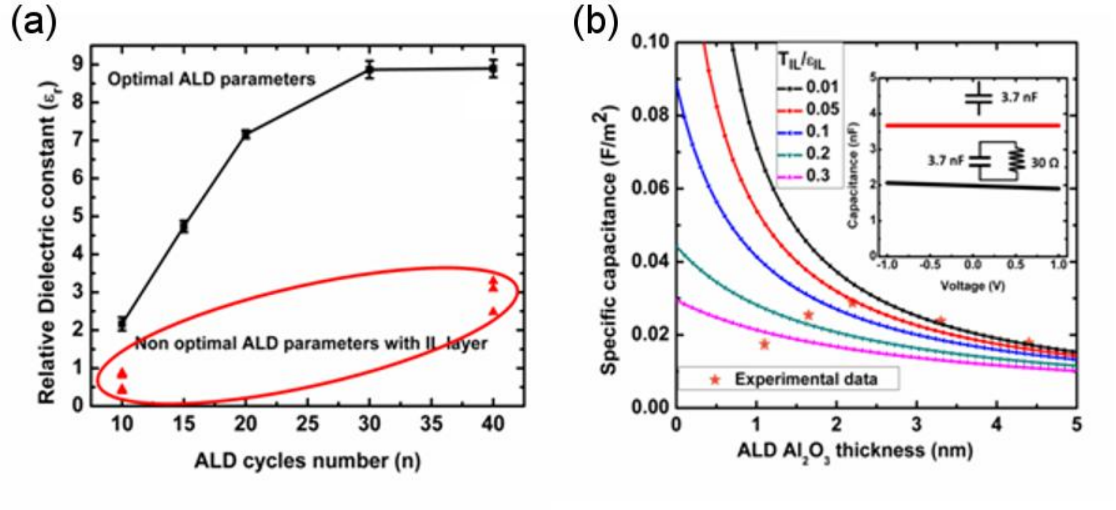

Figure 4.12: (a) Variation of dielectric constant for both optimal and non-optimal ALD condition. (b) Modeling of specific capacitance for ALD Al_2O_3 using interfacial layer capacitance Inset shows decrease in measured capacitance for standard 3.7 nF capacitor connected in parallel with 30 Ω resistor

However when the ALD Al_2O_3 thickness is decreased below 3 nm, this high ε_r drops sharply to a value of 2.2 for a 1.1 nm thick ALD Al_2O_3 tunnel barrier. Since the IL contributes more significantly to the composite film when the ALD Al_2O_3 thickness is small, an IL may explain this reduced ε_r. To examine this possibility, the IL-Al_2O_3 system was modeled as two capacitors in series with the specific capacitance (C_T/A) given by Eq. 4.5.

$$\frac{C_T}{A} = \frac{\varepsilon_o}{\left(\frac{T_{IL}}{\varepsilon_{IL}} + \frac{T_{ALD}}{\varepsilon_{ALD}}\right)} \qquad \text{Eq. 4.5}$$

where T_{IL} and T_{ALD} are thickesses of the IL and ALD Al_2O_3 film, and ε_{IL} and ε_{ALD} are the dielectric constants for the IL and ALD Al_2O_3 dielectric film respectively. Since T_{IL} and ε_{IL} are unknown parameters, the ratio $\frac{T_{IL}}{\varepsilon_{IL}}$ was varied from 0.01 to 0.3. This model for the specific capacitance was plotted in Figure 4.12b using known/measured $\frac{T_{ALD}}{\varepsilon_{ALD}}$ values along with the specific capacitance calculated from the data. The ratio $\frac{T_{IL}}{\varepsilon_{IL}} = 0.01$ curve (black) provides the most reasonable parameters for the specific measured capacitance in the 4.4, 3.3 and 2.2 nm thick ALD Al_2O_3 films. If a low dielectric constant of $\varepsilon_{IL} = 1 \text{ or } 2$ is assumed for a defective IL, than T_{IL} can be estimated to be in the range of 0.1-0.2 Å. This value for the IL thickness is extremely small with a thickness corresponding to the sub-monolayer range, meaning that the IL only exists in certain places on the Al surface.

One can note from Figure 4.12b that the model for two capacitors in series does not match with the data very well when the Al_2O_3 thickness is below about 2 nm. This reduced capacitance may be due to an increased leakage current from quantum tunneling which lowers ε_{ALD} and increases $\frac{T_{ALD}}{\varepsilon_{ALD}}$. To show this effect, a bulk 3.7 nF capacitor (comparable to the measured capacitance of the 1.65 nm ALD Al_2O_3 film) was measured in parallel with a resistor (Figure 4.12b insert). A 30 Ω resistor was able to decrease the capacitance to 2 nF, which is comparable to the difference between the measured capacitance value and the one predicted by this model in Eq. 4.5.

4.8 The ALD Al_2O_3 uniformity

The capacitor study suggests that the IL is sub-monolayer. To shed some additional light on the significnace of the interfacial Layer after optimizing ALD heating conditions, HV *in situ* non-contact Atomic Force Microscopy (NCAFM) meassured the topgoraphy of the Al surface before and after 1 cycle of ALD; shown in Figure 4.13. The scan area was 30 nm x 30 nm with a -14 Hz dF setpoint and a scan speed of 30 nm/s. The bare Al surface, shown in Figure 4.13a, was scanned immediately after 7 nm of Al was sputtered onto an Si/Au(50nm)/Nb(20nm) substrate. This surface is highly uniform with a roughness of 0.212 nm. Mechanical vibrations, due to the large, connected PVD-ALD system, produced nearly horizontal bands in the AFM image which were inverted in the backward scan image. The Al surface after 1 cycle of ALD, shown in Figure 4.13b, is nearly identical with a surface roughness of 0.210 nm. This surface is extememly conformal with no visible varriance in the Al_2O_3 thickness.

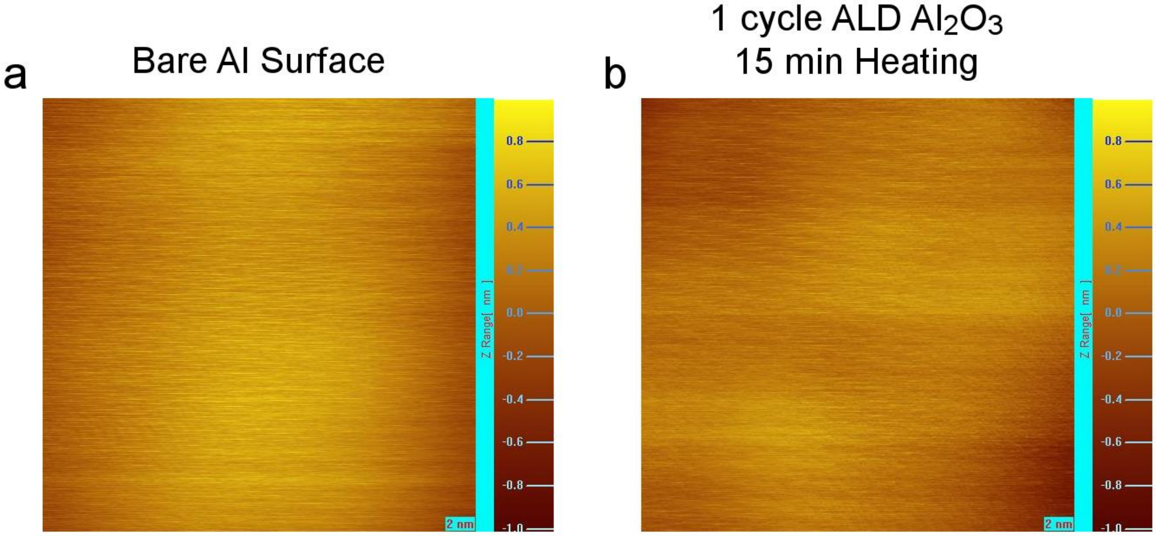

Figure 4.13: *In situ* Non-contact Atomic Force Microscopy topographic images are shown for (a) the Al surface immediately after sputtering and (b) the surface after 1 cycle of ALD Al_2O_3 which was deposited using the optimal ALD heating condition. The images are 30nm x 30nm and the color scale is +/- 1 nm.

For ALD Al_2O_3 to be useful for MIMTJ applications, E_b must also be uniform as pinholes (or low barrier height regions) will dominate tunneling. To examine the E_b uniformity, the STM tip was scanned over a small area of 32 nm x 28 nm. At each pixel in Figure 4.14 the STM recorded the topography (Figure 4.14a), paused briefly, and ramped the bias voltage up-down several times to produce *I-V* and *dI/dV* spectra. The *dI/dV* spectra were analyzed to extract E_b shown at each pixel in Figure 4.14b. In some regions of the scanned area, the surface roughness is very low, on the order of 1 nm. This value for the ALD Al_2O_3 surface roughness is higher than the comparably sized NCAFM image in Figure 4.13b, however this high value may be reasonable given the limited number of pixels in Figure 4.13a (just 224). Unphysical height variations on the order of 10 nm were also observed and are mostly likely due to the convolution of topography with the local electronic properties in STM imaging.

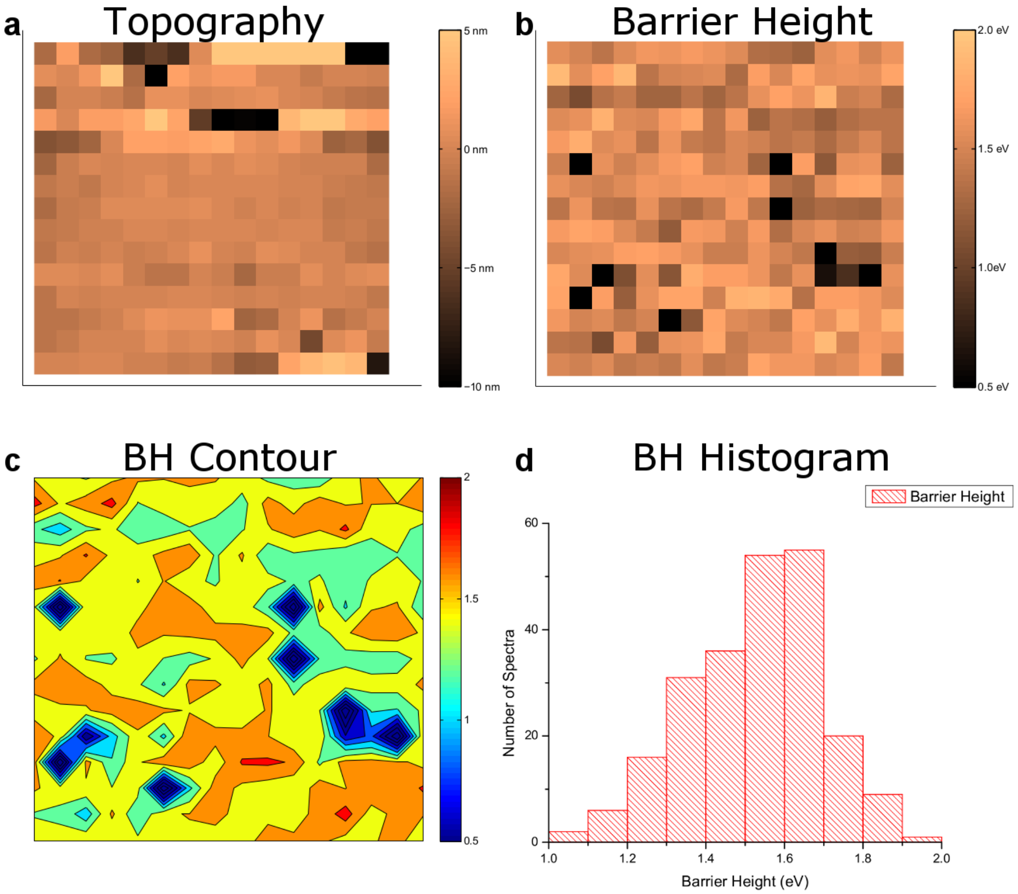

Figure 4.14: Scanning Tunneling Spectroscopy imaging of a 32 nm x 32 nm Area is shown for a 1-cycle ALD Al_2O_3 tunnel barrier. At each pixel (2 nm in size), the STM records the (a) topography and then ramps the bias voltage up-down to generate *dI/dV* spectra. (b) The barrier height, calculated from the *dI/dV* spectra, is shown for these locations. (c) A contour plot was generated from the E_b image in order to better visualize the spatial uniformity of E_b. (d) A histogram for these E_b values is also shown to illustrate the uniformity

About 3-4% of the spectra in Figure 4.14 had an E_b value which was < 0.5 eV. These low E_b locations can be explained by either pinholes in the ALD Al_2O_3 tunnel barrier or locations which broke down prior to the 1st STS spectra as the STM tip was stabilized. This "pinhole" percentage of 3-4% agrees fairly well with our coverage of ALD Al_2O_3 of ~ 93%. However this ALD coverage was about constant with the Al_2O_3 thickness from 1-10 ALD cycles, implying that the "pinhole" density should be constant as well. Since 10 ALD cycle capacitors with areas in excess of 0.04 mm^2 did not show shorts, pinholes are unlikely to be the cause for ***all*** of these low E_b spots. Therefore the second possibility of dielectric breakdown is significantly more likely since the BD frequency observed in STS spectra for 1 cycle ALD Al_2O_3 tunnel barrier was around 70 %.

If a sub-monolayer IL exists, then the E_b values in Figure 4.14b should show spatial variations. To help visualize the overall E_b uniformity in this small scanned area, a contour plot and histogram of the E_b values was generated in Figure 4.14c and Figure 4.14d respectively. A slight grouping of E_b is observed in Figure 4.14c with lower and higher values clustered together, indicating that a very minor IL is present is some areas more than other areas. A fairly wide E_b range is also observed in Figure 4.14d. This spatially non-uniform E_b is consistent for a sub-monolayer IL, as discussed in Figure 4.12b, although non-uniformity of the ALD Al_2O_3 density is an alternate explanation.

4.9 Conclusions

In conclusion, several important insights have been obtained in this investigation. First, pre-ALD Al oxidation can occur through exposure to trace O_2 in the vacuum or though dissociation of $\mathrm{H_2O_{ads}}$ into $\mathrm{O_{ads}}$ on the Al surface, resulting in a defective AlO_x IL. Quantitatively, more serious IL formation occurs at elevated sample temperature and prolonged pre-ALD heating time in the ALD chamber. Secondly, any pre-ALD IL that does form will reduce the $\mathrm{OH_{ad}}$ density on the Al surface which in turn reduces the number of horizontally aligned $\mathrm{OH_{ads}}$ on the Al surface. Consequently TMA nucleation is impaired, resulting in defective ALD Al_2O_3 growth. Thirdly, based on this understanding of the IL formation mechanisms, optimal pre-ALD processing conditions were developed to dynamically heat the sample to the optimal growth temperature window of 150°C-190°C. Temperatures below this range led to $\mathrm{H_2O_{ads}}$ on the Al surface which impaired the TMA nucleation and temperatures above this range led to a rough Al surface through $\mathrm{OH_{ads}}$ dissociation into $\mathrm{O_{ads}}$ and H. In addition, reducing the dynamic heating time down to about 15 min led to ALD Al_2O_3 growth on the Al surface with negligible IL formation.

STS revealed the distinctive effect the IL had on electron tunneling including a reduction in E_b and soft-type dielectric breakdown. Both effects indicate the presence of a defective IL and a defective ALD Al_2O_3 grown on top. As the IL formation was suppressed with optimal pre-ALD processing conditions, a thickness-independent E_b in the range of 1.42-1.56 eV and hard-type dielectric breakdown was achieved. This IL suppression was confirmed with fabricated capacitors with thicker ALD Al_2O_3 tunnel barriers on the order of 1.1-4.4 nm. The ALD Al_2O_3 dielectric constant after IL minimization was extraordinarily high with a value of 8.9. This is the highest measured ALD Al_2O_3 dielectric constant in this thickness range of a few nanometers. Un-optimized ALD heating conditions led to a low dielectric constant of just 0.5 to 2; illustrating the importance of the controlling the IL. The simple model for the specific capacitance found that the IL which remains after optimizations has a thickness on the order of 0.1-0.2 Å. This low value suggests that the IL is sub-monolayer. This sub-monolayer thickness was supported by *in* *situ* AFM and STS images which show an extremely uniform surface topography and a slight clustering of E_b values. This level of M-I interface control is extraordinary. Through carful engineering a high quality insulator has been achieved, for MIMTJ devices, which is atomically-thin.

5 MIMTJ Devices with ALD Al_2O_3 Tunnel Barriers

5.1 Chapter Overview

The ultimate test for any material lies in how it performs in fabricated devices. In this Chapter Josephson Junctions are fabricated and characterized. In addition a preliminary study was done to adapt this *in situ* ALD Al_2O_3 process to be suitable for MTJ devices. In particular, the 7 nm Al layer is deposited on a Fe film and then systematically reduced in thickness as the quality of the ALD Al_2O_3 is monitored. The possibility of Fe-Al intermetallic formation and hydroxylation of Fe with a pre-ALD H_2O pulse is examined with additional AIMD simulations. Finally the possibility of growing ALD Al_2O_3 directly on Fe using this *in situ* ALD process is examined.

5.2 Josephson Junctions

To demonstrate how this ALD Al_2O_3 tunnel barrier performs in a demanding MIMTJ application, JJs were fabricated and their I-V curves (IVCs) were measured at 4.2 K. The IVC of a 5-cycle junction with a designed area of 10 µm x 10 µm is shown in Figure 5.1a. This IVC has a low subgap leakage current and is highly nonlinear-as expected for Superconductor-Insulator-Superconductor tunnel junctions. The small current step at $V = \Delta/e$ of the IVC is most likely caused by Andreev reflection at the interface between the bottom Nb electrode and the 7-nm Al wetting layer of the Nb-Al-Al_2O_3-Nb structure [121] and not due to transport through pinholes-as discussed in [122]. The superconducting gap voltage was $V_g \equiv 2\Delta/e \cong 2.6$ mV and did not depend on the ALD cycle number. In addition, IR_n versus voltage, where R_n is taken to be the dynamic resistance at 5 mV, is nearly identical for JJs with different ALD cycle numbers; indicating good reproducibility in the junction fabrication process. Even through these JJs were fabricated with ALD Al_2O_3 tunnel barriers under the un-optimized heating conditions (75 min at 156 W), they are of considerably higher quality than prior *in situ* ALD Al_2O_3 JJs fabricated in a previous work which used a low vacuum *in situ* ALD process [56].

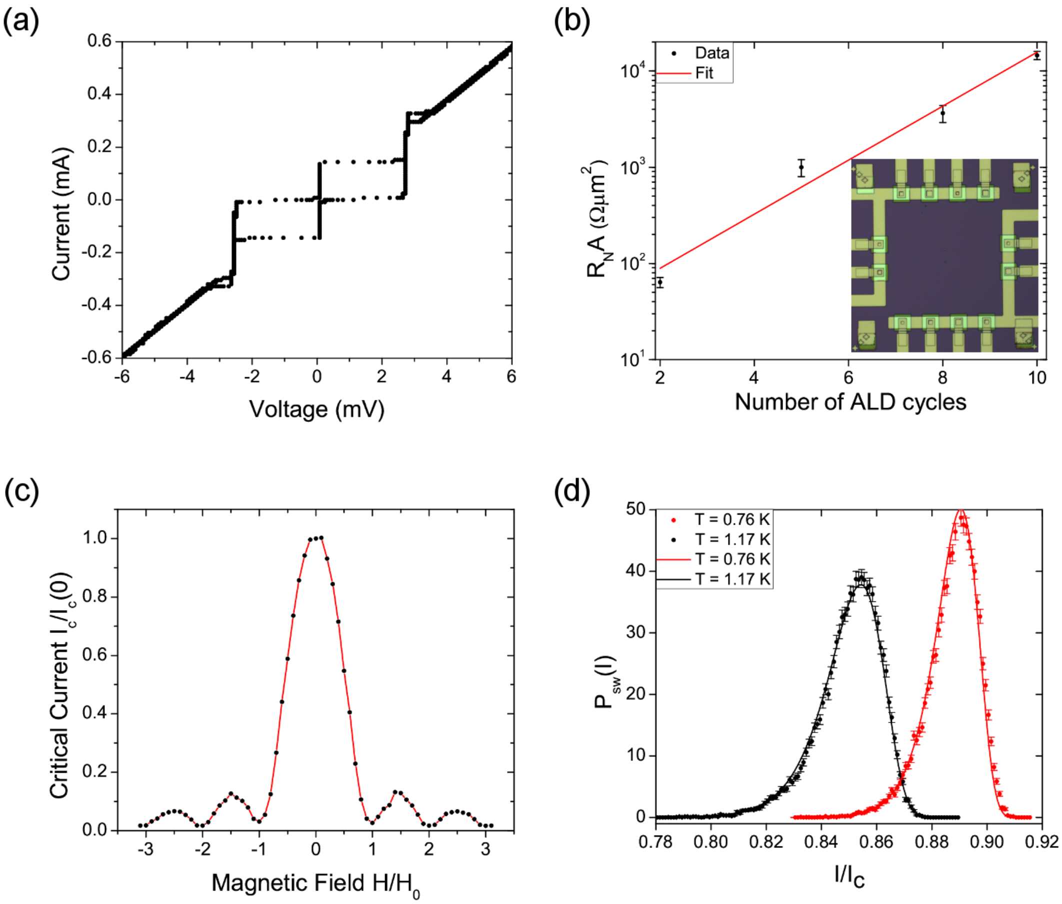

Figure 5.1: Nb/Al/Al_2O_3/Nb Josephson Junctions with an ALD Al_2O_3 tunnel barrier were measured. (a) The I-V characteristics of a 5 ALD cycle 10 µm x 10 µm Josephson Junction at T = 4.2 K is shown which displays a very low leakage current. The bias current waveform was triangular at 5 Hz and was ramped up linearly from zero to 0.6

mA, then from 0.6 mA to -0.6 mA, and finally from -0.6 mA to zero. (b) The critical current density, J_c, as a function of ALD cycle, or equivalently thickness, which follows the expected exponential dependence (solid line). The insert shows a chip with 12 JJs with areas ranging from 5 µm x 5 µm to 10 µm x 10 µm (c) The magnetic field dependence of the average switching current is shown for a similar 5-cycle JJ processed from the same batch. The Magnetic field and switching current have been normalized to the field at the 1st minimum (12 Oe) and the switching current at the central maximum (76 µA). (d) The measured switching current distributions of a 10-cycle junction at T = 0.76 K and 1.17 K. The lines are calculated switching current distributions based on thermal activation theory.

Recently, by measuring the dependence of the JJ's critical current density on oxygen exposure, a proxy for tunnel barrier thickness d, the thermal AlO_x tunnel barrier E_b was found to be ~0.64 eV [41]. Notice that it is very difficult to calibrate the relationship between thickness, d, and oxygen exposure. In contrast, due to the self-limited, layer-by-layer growth nature of ALD, the growth rate of the ALD Al_2O_3 tunnel barrier has been precisely calibrated as $d_{\mathrm{ALD}} = 0.115 \pm 0.005$ nm/cycle [65]. To confirm the ALD JJ E_b values from our *in situ* STS measurement, the measured critical current density, $G_n = (R_n A)^{-1} \propto J_c$ was plotted against d_{ALD} in Figure 5.1b. Because thermal and magnetic field fluctuations have a strong effect on the switching current but have essentially no effect on the normal-state resistance, R_n, especially for JJs with small critical currents, it is much more reliable to extract E_b by fitting the exponential dependence of G_n versus d_{ALD} as shown in Eq. 5.1.

$$G_n = G_0 e^{-d_{ALD}\sqrt{\frac{2mE_b}{\hbar^2}}} \qquad \text{Eq. 5.1}$$

where m_e is the electron mass, $\hbar$ is the Planck constant, and G_0 is the specific conductance for d_{ALD} = 0. The tunnel barrier height determined from the best fit was E_b = 1.10 ± 0.06 eV. This E_b value agrees well with our STS measurements for our un-optimized ALD process.

Ideal tunnel junctions require a uniform tunnel barrier with no microscopic pinholes as pinholes lead to subgap leakage current and a distorted magnetic field dependence on I_c. The magnetic field dependence of the critical current, $I_c(H)$, for a 5-cycle junction is shown in Figure 5.1c. Complete I_c suppression at the first minimum and a symmetric shape was observed. The applied magnetic field H was in the plane of the junction (x-y plane) and parallel to the vertical edges of the 7 µm x 7 µm junction (although a small misalignment cannot be ruled out). This symmetric behavior is consistent with a uniform insulating tunnel barrier with negligible leakage current and pinholes [26].

A denser tunnel barrier should have fewer atomic-scale TLDs. TLDs lead to distortions in the junction's switching current distribution $P_{sw}(I)$ [32, 123, 124]. Therefore, $P_{sw}(I)$ can be used as a diagnostic tool for the detection of TLDs in tunnel barriers which couple strongly to the junction. Figure 5.1d shows the experimental $P_{sw}(I)$ which was obtained using the conventional time-of-flight technique [125-127] with a constant current sweeping rate of 5 mA/s in a very well filtered and shielded cryostat suitable for coherent quantum dynamics of Josephson qubits [127, 128]. In order to reduce the effect of self-heating, a 7 µm x 7 µm, 10-ALD cycle junction with a very low critical current density of J_c = 9.7 A/cm^2 was selected for the $P_{sw}(I)$ measurements. The critical current of the junction, I_c = 4.757 ± 0.003 µA, was determined by fitting the measured $P_{sw}(I)$ to the prediction from thermal activation theory with the critical current as the adjustable parameter [125-127]. The junction's shunt capacitance was estimated to be, $C \approx 2.2$ pF, from the 45 fF/μm^2 specific capacitance of low-J_c Nb JJs and the junction's nominal area [129]. Typical $P_{sw}(I)$ curves obtained at T = 0.76 K and 1.17 K are shown in Figure 5.1d. The measured distributions agree very well with those calculated from thermal activation theory. The absence of anomalies in the $P_{sw}(I)$ distributions is consistent with a lack of TLDs which couple strongly to the junction in the tunnel barrier and/or at the superconductor-insulator interface.

5.3 Adapting ALD Al_2O_3 for Magnetic Tunnel Junctions

An atomically-thin, low defect density ALD Al_2O_3 tunnel barrier has excellent potential as an insulator for MTJs. Current state of the art MTJs have epitaxial MgO tunnel barriers with excellent TMR values ranging from 220-410% [130-132]. In comparison, the best know TMR value for MTJs with Al_2O_3 tunnel barriers is only 70% [133]. While this Al_2O_3 TMR value is significantly lower than the best MgO TMR values, Al_2O_3 has the significant advantage of not requiring high temperature anneals. In addition, the MgO thickness is limited to about 1- 2 nm due to the high risk of defective grain boundaries within the tunnel junction. *In situ* ALD Al_2O_3 may be competitive with MgO MTJs due to an order of magnitude reduction in the tunnel barrier thickness down to the atomic-scale.

However, there is one significant challenge that must be overcome for our ALD Al_2O_3 tunnel barrier to be used in MTJs. That is the 7 nm thick aluminum layer which can scatter the spin-polarized current, reducing the TMR. This scattering will be strongly dependant on the aluminum thickness. Therefore, the first step towards adapting our ALD Al_2O_3 process for MTJ devices is to reduce the thickness of the Al layer on Fe and to examine the resulting ALD Al_2O_3 quality. In Figure 5.2a, 1 cycle of ALD Al_2O_3 was grown on this Fe/Al structure (see Figure 5.2a insert schematic) with various Al thicknesses. After Al_2O_3 deposition, *in situ* STS measured the E_b and ALD coverage on the surface. One cycle of ALD was chosen because it is the most sensitive to any issues with IL growth or poor ALD nucleation. The ALD Al_2O_3 E_b value is identical to the case without the Fe layer when the Aluminum layer is greater than about 4 nm in thickness. However when the Al thickness is reduced below 4 nm, the E_b value decreases significantly from ~1.63 eV (7 nm Al) to ~1.44 eV (1nm Al).

To eliminate this possibility that this E_b reduction is due to the development of an FeO_x IL, the ALD cycle number was varied with the Al thickness held constant at 1 nm. The resulting E_b and ALD coverage is shown in Figure 5.2b. If an FeO_x IL formed, E_b should increase with Al_2O_3 thickness, as was the case in Figure 3.6b and Figure 4.9d for the un-optimized ALD heating conditions which had an IL. Instead, a constant E_b and ALD coverage was observed as a function of Al_2O_3 thickness which indicates that the ALD Al_2O_3 density was reduced instead of IL formation. As discussed earlier, a rough topography leads to the formation vertically-aligned $\mathrm{OH_{ads}}$ which have a steric hindrance for TMA nucleation, possibly resulting in a reduced ALD Al_2O_3 density.

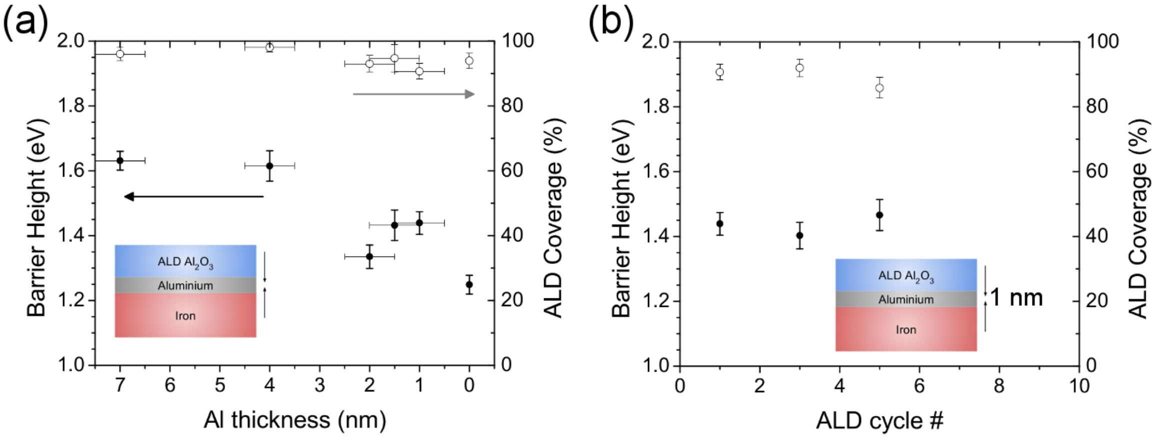

Figure 5.2: Al_2O_3 was deposited using our *in situ* ALD process onto an Al/Fe structure. STS measured E_b and the surface coverage of ALD for (a) 1 cycle of ALD Al_2O_3 deposited on Al with varying thickness (b) ALD Al_2O_3 of varying thickness deposited on a 1 nm Al layer. The inserts depict the layered structure which was deposited.

One important question to ask whenever ultrathin metal layers are deposited on one another is if there are any issues with the metal-metal interface. Diffusion of one metal into the other is a strong possibly, especially when the metal layers are exposed to elevated temperatures. These intermetallic layers can by micrometers thick depending on the metals used and the sample temperature during or after deposition. Al-Au intermetallics such as Al_2Au_5 wreaked havoc in our early attempts to measure ALD Al_2O_3 samples with STS. Al-Fe intermetallic layers may also be possible. Molecular dynamics simulations have shown that the thickness of the Al-Fe intermetallic layer depends strongly on the Fe orientation; Fe(111) being the most severe with an intermetallic layer thickness of around 0.5 nm [134]. However these simulations were run at room temperature for simulated e-beam evaporation. Aluminum deposited by magnetron sputtering will have additional kinetic energy which may extend this intermetallic layer thickness into the 1 nm range. This Al-Fe intermetallic may significantly increase the surface roughness. Additional investigations will be needed to confirm if this is the case. Overall though, while some ALD Al_2O_3 quality was lost going from 7 nm to 1 nm Al on Fe, the resulting ALD Al_2O_3 tunnel barrier is still of excellent quality and is quite promising for MTJ devices.

What is particularly interesting about Figure 5.2is that it appears ALD Al_2O_3 can still be grown in the absence of Al on Fe. In fact the E_b value for ALD Al_2O_3 grown directly on Fe is not too bad with a value of 1.25 eV. Achieving ALD Al_2O_3 growth directly on Fe would be a game changer as there will no longer be spin-current scattering though a thin Al layer. Even though the barrier height is smaller, the barrier thickness may still be atomically-thin. To further examine the possibility that ALD Al_2O_3 can be grown directly on Fe for MTJs, AIMD simulations were run in Figure 5.3 to simulate the pre-ALD H_2O pulse on different orientations of Fe. We find that a hydroxylated Fe surface is possible with a pre-ALD H_2O pulse; however the effectiveness in generating $\mathrm{OH_{ads}}$ without dissociation into $\mathrm{O_{ads}}$ is dependent on the Fe surface orientation. The Fe (110) and Fe (100) surfaces both result in $\mathrm{OH_{ads}}$ creation without much $\mathrm{O_{ads}}$ formation whereas the Fe (111) surface leads to a high amount of $\mathrm{O_{ads}}$. IL formation from the pre-ALD H_2O pulse is therefore expected on the Fe (111). This IL formation likely explains the reduced E_b when *in situ* ALD Al_2O_3 is grown on Fe instead of Al. Additional optimization in the ALD heating parameters may be required to minimize this possibility for IL formation.

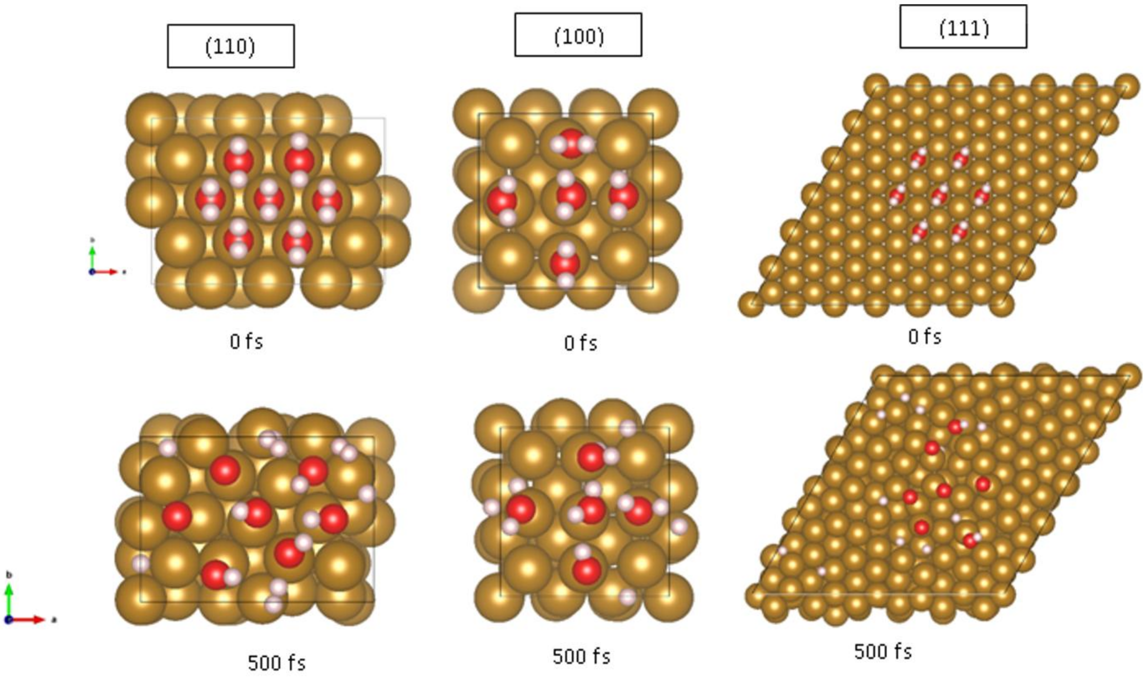

Figure 5.3: Snapshots from AIMD simulations are shown for a water pool placed on a Fe (110), Fe (100) and Fe (111) surface at 473 K for times up to 500 fs.

Since preliminary AIMD simulations and STS data suggests that ALD Al_2O_3 growth directly on Fe may be possible, however with an iron oxide IL likely resulting from the pre-ALD H_2O pulse. To confirm that IL formation occurs when *in situ* ALD Al_2O_3 is grown on Fe, ALD Al_2O_3 films were grown on Fe with varying cycle numbers. STS reveals, in Figure 5.4, a high, near constant coverage of ALD on the Fe surface with an increasing E_b as a function of ALD cycle number. This non-constant E_b supports that IL formation occurs possibly due to iron oxide formation from the pre-ALD H_2O pulse. Future work will be needed to optimize the *in situ* ALD process for the Al_2O_3 deposition on Fe. Overall though, while some Al_2O_3 quality was lost when grown on Fe, the possibility that this *in situ* ALD Al_2O_3 process may be used for MTJ devices is very exciting.

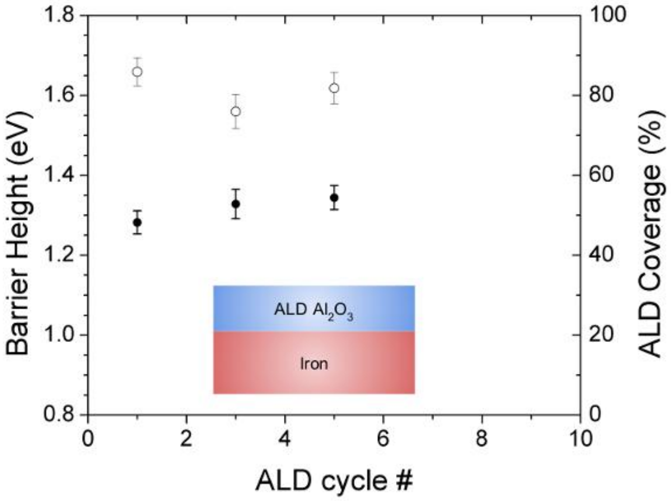

Figure 5.4: An STS study on the growth of ALD Al_2O_3 on Fe. A varying number of ALD cycles were deposited directly on the Fe in the configuration shown in the insert. The tunnel barrier height E_b is shown in the solid points and the ALD coverage in the hollow points.

5.4 Conclusions

In conclusion, this *in situ* ALD Al_2O_3 process can be utilized as in insulator for MIMTJ devices. The preliminary JJ results are quite promising. A preliminary STS study found that high quality ALD Al_2O_3 tunnel barriers can be deposited on top of an ultrathin layer of Al sputtered onto an Fe layer. An increased surface roughness, caused by an Al-Fe intermetallic < 1nm in thickness, slightly impaired the ALD Al_2O_3 density. Excitingly, we found that ALD Al_2O_3 deposition is possible directly on the Fe surface. Future works will be required to realize MTJ devices and optimize the *in situ* ALD process to reduce IL formation on the Fe surface.

6 Conclusions and Future Perspectives

As the Semiconductor industry approaches the end of Moore's law, new materials and fabrication methods are critically needed to counter exponentially increasing development costs. The next generation of MIMTJ devices demands an atomically-thin and low defect insulator. Building off of previous works, we continued the development of an *in situ* HV PVD-ALD Al_2O_3 process for MIMTJ fabrication. AIMD simulations together with *in situ* STS found that a well-controlled pre-ALD H_2O pulse can hydroxylate the Al surface in preparation for ALD. Careful control of this pre-ALD H_2O pulse is the key to enable TMA nucleation over the entire Al surface after only one ALD cycle. The quality of this *in situ* ALD Al_2O_3 tunnel barrier is significantly higher than the thermal AlO_x tunnel barrier with an E_b of 1.4-1.6 eV which is constant with thickness in the range of 0.12-1.2 nm. Furthermore, this ALD Al_2O_3 tunnel barrier has an extraordinarily high band gap of about 2.6 eV which is comparable to high-quality epitaxial Al_2O_3 thin films.

To grow any material at the atomic-scale means that it's interface with other materials must be very well controlled. In order to optimize this *in situ* ALD process to minimize IL formation, AIMD simulations explored the mechanisms of IL formation even in the HV environment. We found that a thermal AlO_x IL can form either before ALD during a prolonged exposure to trace oxygen or H_2O in the vacuum chamber or during the pre-ALD H_2O pulse. An optimal pre-ALD H_2O temperature window of 150 °C-190 °C was found. Temperatures below this range led to incomplete $\mathrm{H_2O_{ad}}$ dissociation into $\mathrm{OH_{ad}}$ and temperature above this range let to thermal AlO_x IL formation due to $\mathrm{OH_{ad}}$ dissociation into $\mathrm{O_{ad}}$ and H.

Reducing the time spent heating in the ALD chamber had the most dramatic effect towards minimizing IL formation. A dynamic heating strategy was developed to bring the sample temperature to this ideal temperature window in a varying amount of time, at the cost of a non-constant ALD temperature. Using *in situ* STS a dramatic E_b improvement was observed from 0.9 eV to 1.6 eV as the pre-ALD heating time was reduced from 75 min to 15 min. In addition, E_b becomes more constant with thickness as the heating time is reduced, indicating reduced IL formation with shorter heating times. In addition, we observed the distinctive effect the IL had on dielectric breakdown. With the long heating time of 75 min, soft-type dielectric breakdown was observed, indicating the presence of an IL, however with the short heating time of 15 min, hard-type dielectric breakdown was observed, indicating a very low defect density within the Al_2O_3 and the IL. We confirmed that the IL was significantly suppressed by fabricating capacitors with ALD Al_2O_3 layers with thicknesses in the range of 1.1-4.4 nm. With the optimal heating conditions the dielectric constant was extraordinarily high with a value of 8.9 in the 3-4 nm thickness range. Un-optimized ALD heating conditions led to a low dielectric constant of just 0.5 to 2 in the same thickness range. This sensitivity clearly illustrates the impact of the IL on the quality of the Al_2O_3 achieved with this *in situ* ALD process.

We also estimated the remaining IL thickness after optimizations to be in the range of 0.1-0.2 Å using a model for the specific capacitance. This sub-monolayer IL thickness was supported by *in situ* AFM and STS images which show an extremely uniform surface topography and a slightly non-uniform E_b distribution on the surface. Through our optimizations, we have achieved the world’s first atomically-thin Al_2O_3 dielectric which has a sub-monolayer IL while maintaining a high barrier height, band gap, and dielectric constant.

In conclusion, we have shown that this *in situ* ALD process can create extremely high quality insulators on the aluminum wetting layer at the monolayer thickness scale. We also did a preliminary STS study on the feasibility of adapting this *in situ* ALD Al_2O_3 process for MTJs. For this application, the Al wetting layer has to be reduced or eliminated. We find that high quality Al_2O_3 tunnel barriers can be grown on ultrathin Al on Fe with a slight reduction in Al_2O_3 quality most likely due to an increased surface roughness from a possible Al-Fe intermetallic layer. Excitingly, we also found that ALD Al_2O_3 deposition is possible directly on the Fe surface. However early data indicates that an IL forms on the Fe-Al_2O_3 interface. Future works will be required to optimize the heating parameters, in particular the pre-ALD H_2O pulse temperature, to improve the hydroxylation of the Fe surface without IL formation. Preliminary fabricated JJ using the un-optimized *in situ* ALD process show promise. The next step will be to fabricate JJs with our optimized ALD process and compare their characteristics to the standard thermal AlO_x JJs. No project is every complete as there will always more science and engineering that can be done. The future of this project will be to harvest the knowledge we have gained to realize the next generation of MIMTJ devices. The true beauty of this *in situ* ALD method is that with some simple optimizations, Al_2O_3 can be grown on many different substrates for various applications and given that many materials deposited using ALD processes rely on the presence of a hydroxylated surface, alternative insulators to Al_2O_3 may also be possible on various substrates. Thus we have created a highly versatile method of growing extremely thin and high quality ALD films which may help Moore’s law continue on for a little bit longer as our microelectronic devices approach the atomic-scale.

References

[1] (2015). *Technology Quarterly After Moors's Law*. Available: http://www.economist.com/technology-quarterly/2016-03-12/after-moores-law

[2] (2017). *Moore's Law*. Available: https://en.wikipedia.org/wiki/Moore%27s_law

[3] G. E. Moore, "Cramming more components onto integrated circuits (Reprinted from Electronics, pg 114-117, April 19, 1965)," *Proceedings of the Ieee,* vol. 86, pp. 82-85, Jan 1998.

[4] A. Wei. (2017). *10 nm Process Rollout Marching Right Along*. Available: http://www.techinsights.com/about-techinsights/overview/blog/10nm-rollout-marching-right-along/

[5] A. Shilov. (2017). *Samsung and TSMC Roadmaps: 8 and 6 nm Added, Looking at 22ULP and 12FFC*. Available: https://www.anandtech.com/show/11337/samsung-and-tsmc-roadmaps-12-nm-8-nm-and-6-nm-added/2

[6] "Intel Supports American Innovation with $7 Billion Investment in Next-Generation Semiconductor Factory in Arizona," ed. Intel, 2017.

[7] D. Vogler. (2015). *The Roadmap to 5nm: Convergence of Many Solutions Needed*. Available: http://www.semi.org/en/node/55926

[8] M. Lapedus. (2016). *5nm Fab Challenges*. Available: http://semiengineering.com/5nm-fab-challenges/

[9] R. P. Feynman, "There's plenty of room at the bottom," *Engineering and science,* vol. 23, pp. 22-36, 1960.

[10] S. Hassan, Humaira, and M. Asghar, "Limitation of Silicon Based Computation and Future Prospects," in *Communication Software and Networks, 2010. ICCSN '10. Second International Conference on*, 2010, pp. 559-561.

[11] S. S. BintiMdSallah, H. Mohamed, M. Mamun, and M. S. Amin, "CMOS downsizing: present, past and future," *Journal of Applied Sciences Research,* vol. 8, pp. 4138-4146, 2012.

[12] S. G. Kandlikar, "Review and projections of integrated cooling systems for three-dimensional integrated circuits," *Journal of Electronic Packaging,* vol. 136, p. 024001, 2014.

[13] P. Bright. (2016). *Intel retires "tick-tock" development model, extending the life of each process*. Available: https://arstechnica.com/information-technology/2016/03/intel-retires-tick-tock-development-model-extending-the-life-of-each-process/

[14] A. Barone and G. Paterno, *Physics and applications of the Josephson effect* vol. 1: Wiley Online Library, 1982.

[15] J.-G. Zhu and C. Park, "Magnetic tunnel junctions," *Materials Today,* vol. 9, pp. 36-45, 11// 2006.

[16] D. J. Griffiths, *Introduction to Quantum Mechanics*: Pearson Prentice Hall, 2005.

[17] A. C. Seabaugh and Q. Zhang, "Low-voltage tunnel transistors for beyond CMOS logic," *Proceedings of the IEEE,* vol. 98, pp. 2095-2110, 2010.

[18] L. A. Abelson and G. L. Kerber, "Superconductor integrated circuit fabrication technology," *Proceedings of the IEEE,* vol. 92, pp. 1517-1533, 2004.

[19] B. D. Josephson, "POSSIBLE NEW EFFECTS IN SUPERCONDUCTIVE TUNNELLING," *Physics Letters,* vol. 1, pp. 251-253, 1962.

[20] A. W. Kleinsasser, R. E. Miller, and W. H. Mallison, "Dependence of critical current density on oxygen exposure in Nb-AlO/sub x/-Nb tunnel junctions," *Applied Superconductivity, IEEE Transactions on,* vol. 5, pp. 26-30, 1995.

[21] H. Strobel, W. Muessel, D. Linnemann, T. Zibold, D. B. Hume, L. Pezzè*, et al.*, "Fisher information and entanglement of non-Gaussian spin states," *Science,* vol. 345, pp. 424-427, 2014.

[22] C. Kaiser, *High Quality Nb, Al-AlO_1tnx, Nb Josephson Junctions: Technological Development and Macroscopic Quantum Experiments* vol. 4: KIT Scientific Publishing, 2011.

[23] J. Carbotte, "Properties of boson-exchange superconductors," *Reviews of Modern Physics,* vol. 62, p. 1027, 1990.

[24] B. Antonio and P. Gianfranco, *Physics and Applications of the Josephson Effect*: Wiley and Sons Inc., 1982.

[25] T. Van Duzer and C. W. Turner, "Principles of superconductive devices and circuits," 1981.

[26] R. Dynes and T. Fulton, "Supercurrent density distribution in Josephson junctions," *Physical Review B,* vol. 3, p. 3015, 1971.

[27] D. Aharonov, "Quantum computation," *Annual Reviews of Computational Physics VI,* pp. 259-346, 1999.

[28] T. D. Ladd, F. Jelezko, R. Laflamme, Y. Nakamura, C. Monroe, and J. L. O'Brien, "Quantum computers," *Nature,* vol. 464, pp. 45-53, 2010.

[29] J. M. Martinis, "Superconducting phase qubits," *Quantum Information Processing,* vol. 8, pp. 81-103, 2009.

[30] L. Chirolli and G. Burkard, "Decoherence in solid-state qubits," *Advances in Physics,* vol. 57, pp. 225-285, 2008.

[31] S. Spilla and J. Splettstößer, "Coherence properties in superconducting flux qubits," 2014.

[32] R. W. Simmonds, K. Lang, D. A. Hite, S. Nam, D. P. Pappas, and J. M. Martinis, "Decoherence in Josephson phase qubits from junction resonators," *Physical Review Letters,* vol. 93, p. 077003, 2004.

[33] M. Khalil, M. Stoutimore, S. Gladchenko, A. Holder, C. Musgrave, A. Kozen*, et al.*, "Evidence for hydrogen two-level systems in atomic layer deposition oxides," *Applied Physics Letters,* vol. 103, p. 162601, 2013.

[34] R. McDermott, "Materials origins of decoherence in superconducting qubits," *Applied Superconductivity, IEEE Transactions on,* vol. 19, pp. 2-13, 2009.

[35] E. Tan, P. Mather, A. Perrella, J. Read, and R. Buhrman, "Oxygen stoichiometry and instability in aluminium oxide tunnel barrier layers," *arXiv preprint cond-mat/0501354,* 2005.

[36] D. Wang, C. Nordman, J. M. Daughton, Z. Qian, and J. Fink, "70% TMR at room temperature for SDT sandwich junctions with CoFeB as free and reference layers," *Magnetics, IEEE Transactions on,* vol. 40, pp. 2269-2271, 2004.
[37] M. Gurvitch, M. Washington, and H. Huggins, "High quality refractory Josephson tunnel junctions utilizing thin aluminum layers," *Applied Physics Letters,* vol. 42, pp. 472-474, 1983.
[38] L. Jeurgens, W. Sloof, F. Tichelaar, and E. Mittemeijer, "Growth kinetics and mechanisms of aluminum-oxide films formed by thermal oxidation of aluminum," *Journal of applied physics,* vol. 92, pp. 1649-1656, 2002.
[39] N. Cai, G. Zhou, K. Müller, and D. E. Starr, "Tuning the limiting thickness of a thin oxide layer on Al (111) with oxygen gas pressure," *Physical review letters,* vol. 107, p. 035502, 2011.
[40] K. Volgmann, F. Voigts, and W. Maus-Friedrichs, "The interaction of H 2 O molecules with iron films studied with MIES, UPS and XPS," *Surface Science,* vol. 606, pp. 858-864, 2012.
[41] X. Kang, L. Ying, H. Wang, G. Zhang, W. Peng, X. Kong*, et al.*, "Measurements of tunneling barrier thicknesses for Nb/Al–AlOx/Nb tunnel junctions," *Physica C: Superconductivity,* vol. 503, pp. 29-32, 2014.
[42] Y. Ando, M. Hayashi, S. Iura, K. Yaoita, C. Yu, H. Kubota*, et al.*, "Growth mechanism of thin insulating layer in ferromagnetic tunnel junctions prepared using various oxidation methods," *Journal of Physics D: Applied Physics,* vol. 35, p. 2415, 2002.
[43] O. Kurnosikov, F. de Nooij, P. LeClair, J. Kohlhepp, B. Koopmans, H. Swagten*, et al.*, "STM-induced reversible switching of local conductivity in thin Al 2 O 3 films," *Physical Review B,* vol. 64, p. 153407, 2001.
[44] J. Barner and S. Ruggiero, "Tunneling in artificial Al 2 O 3 tunnel barriers and Al 2 O 3-metal multilayers," *Physical Review B,* vol. 39, p. 2060, 1989.
[45] J. J. Åkerman, J. Slaughter, R. W. Dave, and I. K. Schuller, "Tunneling criteria for magnetic-insulator-magnetic structures," *Applied Physics Letters,* vol. 79, pp. 3104-3106, 2001.
[46] C. Dietrich, B. Koslowski, and P. Ziemann, "Ultrathin epitaxial Al 2 O 3 films grown on Nb (110)⁄ sapphire (0001) investigated by tunneling spectroscopy and microscopy," *Journal of applied physics,* vol. 97, p. 083515, 2005.
[47] P. B. Welander and J. N. Eckstein, "Strained single-crystal Al 2 O 3 grown layer by layer on Nb (110) thin films," *Applied physics letters,* vol. 90, p. 243510, 2007.
[48] S. Oh, K. Cicak, J. S. Kline, M. A. Sillanpää, K. D. Osborn, J. D. Whittaker*, et al.*, "Elimination of two level fluctuators in superconducting quantum bits by an epitaxial tunnel barrier," *Physical Review B,* vol. 74, p. 100502, 2006.
[49] H. Takeuchi, A. Wung, X. Sun, R. T. Howe, and T.-J. King, "Thermal budget limits of quarter-micrometer foundry CMOS for post-processing MEMS devices," *IEEE transactions on Electron Devices,* vol. 52, pp. 2081-2086, 2005.
[50] M. Leskelä and M. Ritala, "Atomic layer deposition (ALD): from precursors to thin film structures," *Thin solid films,* vol. 409, pp. 138-146, 2002.

[51] V. Miikkulainen, M. Leskelä, M. Ritala, and R. L. Puurunen, "Crystallinity of inorganic films grown by atomic layer deposition: Overview and general trends," *Journal of Applied Physics,* vol. 113, p. 021301, 2013.

[52] F. Werner, W. Stals, R. Görtzen, B. Veith, R. Brendel, and J. Schmidt, "High-rate atomic layer deposition of Al2O3 for the surface passivation of Si solar cells," *Energy Procedia,* vol. 8, pp. 301-306, 2011.

[53] S. M. George, "Atomic Layer Deposition: An Overview," *Chemical Reviews,* vol. 110, pp. 111-131, 2010/01/13 2009.

[54] R. L. Puurunen, "Surface chemistry of atomic layer deposition: A case study for the trimethylaluminum/water process," *Journal of applied physics,* vol. 97, p. 9, 2005.

[55] C. Rigetti, J. M. Gambetta, S. Poletto, B. Plourde, J. M. Chow, A. Córcoles*, et al.*, "Superconducting qubit in a waveguide cavity with a coherence time approaching 0.1 ms," *Physical Review B,* vol. 86, p. 100506, 2012.

[56] R. Lu, A. J. Elliot, L. Wille, B. Mao, S. Han, J. Z. Wu*, et al.*, "Fabrication of Josephson Junctions Using In Situ Magnetron Sputtering and Atomic Layer Deposition," *Applied Superconductivity, IEEE Transactions on,* vol. 23, pp. 1100705-1100705, 2013.

[57] M.-h. Chi, "FinFET technology: Overview and status at 14nm node and beyond," in *Semiconductor Technology International Conference (CSTIC), 2016 China*, 2016, pp. 1-3.

[58] S. Gieraltowska, L. Wachnicki, B. S. Witkowski, R. Mroczynski, P. Dluzewski, and M. Godlewski, "Characterization of dielectric layers grown at low temperature by atomic layer deposition," *Thin Solid Films,* vol. 577, pp. 97-102, 2015.

[59] M. Groner, F. Fabreguette, J. Elam, and S. George, "Low-temperature Al2O3 atomic layer deposition," *Chemistry of Materials,* vol. 16, pp. 639-645, 2004.

[60] D. S. Ghosh, "Basics of Ultrathin Metal Films and Their Use as Transparent Electrodes," in *Ultrathin Metal Transparent Electrodes for the Optoelectronics Industry*, ed: Springer, 2013, pp. 11-32.

[61] S. M. Moyerman, G. Feng, L. Krayer, N. Stebor, and B. G. Keating, "Atomic Layer Deposition of Tunnel Barriers for Superconducting Tunnel Junctions," *Journal of Low Temperature Physics,* vol. 176, pp. 237-242, 2014.

[62] C. Xu, T. Sritharan, and S. Mhaisalkar, "Thin film aluminum–gold interface interactions," *Scripta materialia,* vol. 56, pp. 549-552, 2007.

[63] M. Diešková, M. Konôpka, and P. Bokes, "Atomic and electronic structure of ultra-thin Al/AlO x/Al interfaces," *Surface Science,* vol. 601, pp. 4134-4137, 2007.

[64] R. Gangineni, C. Bellouard, A. Duluard, B. Negulescu, C. Baraduc, G. Gaudin*, et al.*, "Interfacial electronic transport phenomena in single crystalline Fe-MgO-Fe thin barrier junctions," *Applied Physics Letters,* vol. 104, p. 182402, 2014.

[65] A. J. Elliot, G. Malek, L. Wille, R. Lu, S. Han, J. Z. Wu*, et al.*, "Probing the Nucleation of in Atomic Layer Deposition on Aluminum for Ultrathin Tunneling Barriers in Josephson Junctions," *Applied Superconductivity, IEEE Transactions on,* vol. 23, pp. 1101405-1101405, 2013.

[66] S. D. Elliott, "Atomic-scale simulation of ALD chemistry," *Semiconductor Science and Technology,* vol. 27, p. 074008, 2012.

[67] C. L. Platt, N. Li, K. Li, and T. M. Klein, "Atomic layer deposition of HfO 2: Growth initiation study on metallic underlayers," *Thin Solid Films,* vol. 518, pp. 4081-4086, 2010.

[68] Y. Chang, F. Ducroquet, E. Gautier, O. Renault, J. Legrand, J. Damlencourt*, et al.*, "Surface preparation and post thermal treatment effects on interface properties of thin Al 2 O 3 films deposited by ALD," *Microelectronic engineering,* vol. 72, pp. 326-331, 2004.

[69] M. Groner, J. Elam, F. Fabreguette, and S. M. George, "Electrical characterization of thin Al 2 O 3 films grown by atomic layer deposition on silicon and various metal substrates," *Thin Solid Films,* vol. 413, pp. 186-197, 2002.

[70] K. Kukli, M. Ritala, T. Pilvi, T. Aaltonen, J. Aarik, M. Lautala*, et al.*, "Atomic layer deposition rate, phase composition and performance of HfO2 films on noble metal and alkoxylated silicon substrates," *Materials Science and Engineering B,* vol. 118, pp. 112-116, 2005.

[71] A. J. Elliot, G. A. Malek, R. Lu, S. Han, H. Yu, S. Zhao*, et al.*, "Integrating atomic layer deposition and ultra-high vacuum physical vapor deposition for in situ fabrication of tunnel junctions," *Review of Scientific Instruments,* vol. 85, p. 073904, 2014.

[72] S. Ernst, "Optimisation of the preparation process for tips used in scanning tunneling microscopy," *Physics, Technische Universitat Dresden,* 2006.

[73] K. Hipps, "Scanning tunneling spectroscopy (STS)," *Handbook of Applied Solid State Spectroscopy,* pp. 305-350, 2006.

[74] B. Voigtländer, *SCANNING PROBE MICROSCOPY*: Springer, 2016.

[75] N. Nilius, "Properties of oxide thin films and their adsorption behavior studied by scanning tunneling microscopy and conductance spectroscopy," *Surface Science Reports,* vol. 64, pp. 595-659, 2009.

[76] B. Naydenov and J. J. Boland, "Variable-height scanning tunneling spectroscopy for local density of states recovery based on the one-dimensional WKB approximation," *Physical Review B,* vol. 82, p. 245411, 2010.

[77] R. M. Feenstra, J. Lee, M. Kang, G. Meyer, and K. Rieder, "Band gap of the Ge (111) c (2× 8) surface by scanning tunneling spectroscopy," *Physical Review B,* vol. 73, p. 035310, 2006.

[78] S. Lounis, "Theory of Scanning Tunneling Microscopy," *arXiv preprint arXiv:1404.0961,* 2014.

[79] J. G. Simmons, "Generalized formula for the electric tunnel effect between similar electrodes separated by a thin insulating film," *Journal of applied physics,* vol. 34, pp. 1793-1803, 1963.

[80] J. G. Simmons, "Electric tunnel effect between dissimilar electrodes separated by a thin insulating film," *Journal of applied physics,* vol. 34, pp. 2581-2590, 1963.

[81] E. Luo, S. Wong, A. Pakhomov, J. Xu, I. Wilson, and C. Wong, "Tunneling current and thickness inhomogeneities of ultrathin aluminum oxide films in

magnetic tunneling junctions," *Journal of Applied Physics,* vol. 90, pp. 5202-5207, 2001.

[82] R. M. Feenstra, S. Gaan, G. Meyer, and K. Rieder, "Low-temperature tunneling spectroscopy of Ge (111) c (2× 8) surfaces," *Physical Review B,* vol. 71, p. 125316, 2005.

[83] L. Dorneles, D. Schaefer, M. Carara, and L. Schelp, "The use of Simmons' equation to quantify the insulating barrier parameters in Al/AlO x/Al tunnel junctions," *Applied physics letters,* vol. 82, pp. 2832-2834, 2003.

[84] E. Balashov, F. Dalidchik, and B. Shub, "Structure and electronic properties of imperfect oxides and nanooxides," *Russian Journal of Physical Chemistry B,* vol. 2, pp. 840-855, 2008.

[85] T. Kumagai, "Direct observation and control of hydrogen-bond dynamics using low-temperature scanning tunneling microscopy," *Progress in Surface Science,* vol. 90, pp. 239-291, 2015.

[86] N. Magtoto, C. Niu, B. Ekstrom, S. Addepalli, and J. Kelber, "Dielectric breakdown of ultrathin aluminum oxide films induced by scanning tunneling microscopy," *Applied Physics Letters,* vol. 77, pp. 2228-2230, 2000.

[87] M. M. Ugeda, A. J. Bradley, S.-F. Shi, H. Felipe, Y. Zhang, D. Y. Qiu*, et al.*, "Giant bandgap renormalization and excitonic effects in a monolayer transition metal dichalcogenide semiconductor," *Nature materials,* vol. 13, pp. 1091-1095, 2014.

[88] W. Chen, V. Patel, and J. E. Lukens, "Fabrication of high-quality Josephson junctions for quantum computation using a self-aligned process," *Microelectronic Engineering,* vol. 73, pp. 767-772, 2004.

[89] A. J. Elliot, "Josephson Junctions with Tunnel Barriers Grown Via In Situ Atomic Layer Deposition," University of Kansas, 2014.

[90] E. Tan, P. Mather, A. Perrella, J. Read, and R. Buhrman, "Oxygen stoichiometry and instability in aluminum oxide tunnel barrier layers," *Physical Review B,* vol. 71, p. 161401, 2005.

[91] P. Mather, A. Perrella, E. Tan, J. Read, and R. Buhrman, "Tunneling spectroscopy studies of treated aluminum oxide tunnel barrier layers," *Applied Physics Letters,* vol. 86, pp. 242504-242504, 2005.

[92] G. Kresse and J. Hafner, "<i>Ab initio</i> molecular-dynamics simulation of the liquid-metal–amorphous-semiconductor transition in germanium," *Physical Review B,* vol. 49, pp. 14251-14269, 05/15/ 1994.

[93] J. Hafner, "Ab-initio simulations of materials using VASP: Density-functional theory and beyond," *Journal of Computational Chemistry,* vol. 29, pp. 2044-2078, 2008.

[94] D. Sheppard, R. Terrell, and G. Henkelman, "Optimization methods for finding minimum energy paths," *The Journal of Chemical Physics,* vol. 128, p. 134106, 2008.

[95] G. Paolo, B. Stefano, B. Nicola, C. Matteo, C. Roberto, C. Carlo*, et al.*, "QUANTUM ESPRESSO: a modular and open-source software project for

quantum simulations of materials," *Journal of Physics: Condensed Matter,* vol. 21, p. 395502, 2009.

[96] M. Dion, H. Rydberg, E. Schröder, D. C. Langreth, and B. I. Lundqvist, "Van der Waals Density Functional for General Geometries," *Physical Review Letters,* vol. 92, p. 246401, 2004.

[97] C. Dietrich, H.-G. Boyen, and B. Koslowski, "Characterization of ultrathin insulating Al2O3 films grown on Nb (110)/sapphire (0001) by tunneling spectroscopy and microscopy," *Journal of applied physics,* vol. 94, pp. 1478-1484, 2003.

[98] X. Lai, C. C. Chusuei, K. Luo, Q. Guo, and D. Goodman, "Imaging ultrathin Al 2 O 3 films with scanning tunneling microscopy," *Chemical Physics Letters,* vol. 330, pp. 226-230, 2000.

[99] C. Lanthony, J. M. Ducéré, M. D. Rouhani, A. Hemeryck, A. Estève, and C. Rossi, "On the early stage of aluminum oxidation: An extraction mechanism via oxygen cooperation," *The Journal of Chemical Physics,* vol. 137, p. 094707, 2012.

[100] T. Weckman and K. Laasonen, "First principles study of the atomic layer deposition of alumina by TMA–H 2 O-process," *Physical Chemistry Chemical Physics,* vol. 17, pp. 17322-17334, 2015.

[101] D. Sheppard and G. Henkelman, "Paths to which the nudged elastic band converges," *Journal of computational chemistry,* vol. 32, pp. 1769-1771, 2011.

[102] N. Li, R. Sakidja, and W.-Y. Ching, "Ab initio study on the adsorption mechanism of oxygen on Cr2AlC (0 0 0 1) surface," *Applied Surface Science,* vol. 315, pp. 45-54, 2014.

[103] C. C. Dharmawardhana, R. Sakidja, S. Aryal, and W. Y. Ching, "In search of zero thermal expansion anisotropy in Mo5Si3 by strategic alloying," *Journal of Alloys and Compounds,* vol. 620, pp. 427-433, 2015.

[104] Q. Liu, Y. Gong, J. S. Wilt, R. Sakidja, and J. Wu, "Synchronous growth of AB-stacked bilayer graphene on Cu by simply controlling hydrogen pressure in CVD process," *Carbon,* vol. 93, pp. 199-206, 2015.

[105] G. Henkelman and H. Jónsson, "Improved tangent estimate in the nudged elastic band method for finding minimum energy paths and saddle points," *The Journal of Chemical Physics,* vol. 113, pp. 9978-9985, 2000.

[106] G. Henkelman, B. P. Uberuaga, and H. Jónsson, "A climbing image nudged elastic band method for finding saddle points and minimum energy paths," *The Journal of Chemical Physics,* vol. 113, pp. 9901-9904, 2000.

[107] W. Rippard, A. Perrella, F. Albert, and R. Buhrman, "Ultrathin aluminum oxide tunnel barriers," *Physical review letters,* vol. 88, p. 046805, 2002.

[108] A. Perrella, W. Rippard, P. Mather, M. Plisch, and R. Buhrman, "Scanning tunneling spectroscopy and ballistic electron emission microscopy studies of aluminum-oxide surfaces," *Physical Review B,* vol. 65, p. 201403, 2002.

[109] P. Mather, "ELECTRONIC STRUCTURE OF OXIDE TUNNEL BARRIERS AND GAAS – FERROMAGNET INTERFACES," Doctor of Philosophy Ph.D. Dissertation, Cornell University, 2006.

[110] A. Teverovsky, "Degradation of leakage currents and reliability prediction for tantalum capacitors," in *Reliability and Maintainability Symposium (RAMS), 2016 Annual*, 2016, pp. 1-7.

[111] B. Oliver, G. Tuttle, Q. He, X. Tang, and J. Nowak, "Two breakdown mechanisms in ultrathin alumina barrier magnetic tunnel junctions," *Journal of applied physics,* vol. 95, pp. 1315-1322, 2004.

[112] H. Lin, P. Ye, and G. Wilk, "Leakage current and breakdown electric-field studies on ultrathin atomic-layer-deposited Al 2 O 3 on GaAs," *Applied physics letters,* vol. 87, p. 182904, 2005.

[113] Y. Wu, H. Lin, P. Ye, and G. Wilk, "Current transport and maximum dielectric strength of atomic-layer-deposited ultrathin Al 2 O 3 on GaAs," *Applied physics letters,* vol. 90, p. 072105, 2007.

[114] S. K. Tolpygo and D. Amparo, "Electrical stress effect on Josephson tunneling through ultrathin AlOx barrier in Nb/Al/AlOx/Nb junctions," *Journal of Applied Physics,* vol. 104, p. 063904, 2008.

[115] G. Higashi and C. Fleming, "Sequential surface chemical reaction limited growth of high quality Al2O3 dielectrics," *Applied Physics Letters,* vol. 55, pp. 1963-1965, 1989.

[116] J.-F. Fan, K. Sugioka, and K. Toyoda, "Low-temperature growth of thin films of Al2O3 by sequential surface chemical reaction of trimethylaluminum and H2O2," *Japanese journal of applied physics,* vol. 30, p. L1139, 1991.

[117] H. Kattelus, M. Ylilammi, J. Saarilahti, J. Antson, and S. Lindfors, "Layered tantalum-aluminum oxide films deposited by atomic layer epitaxy," *Thin Solid Films,* vol. 225, pp. 296-298, 1993.

[118] K. Kukli, M. Ritala, M. Leskelä, and J. Jokinen, "Atomic layer epitaxy growth of aluminum oxide thin films from a novel Al (CH 3) 2 Cl precursor and H 2 O," *Journal of Vacuum Science & Technology A: Vacuum, Surfaces, and Films,* vol. 15, pp. 2214-2218, 1997.

[119] R. Ludeke, M. Cuberes, and E. Cartier, "Local transport and trapping issues in Al 2 O 3 gate oxide structures," *Applied Physics Letters,* vol. 76, pp. 2886-2888, 2000.

[120] H. C. Casey, *Devices for Integrated Circuits: Silicon and III-V Compound Semiconductors*: Wiley, 1999.

[121] V. Shaternik, A. Shapovalov, M. Belogolovskii, S. Döring, S. Schmidt, and P. Seidel, "Tunneling characteristics of superconducting junctions with inhomogeneous tunnel barriers," *Materialwissenschaft und Werkstofftechnik,* vol. 44, pp. 205-209, 2013.

[122] T. Klapwijk, G. Blonder, and M. Tinkham, "Explanation of subharmonic energy gap structure in superconducting contacts," *Physica B+ C,* vol. 109, pp. 1657-1664, 1982.

[123] K. B. Cooper, M. Steffen, R. McDermott, R. W. Simmonds, S. Oh, D. A. Hite*, et al.*, "Observation of Quantum Oscillations between a Josephson Phase Qubit and a Microscopic Resonator Using Fast Readout," *Physical Review Letters,* vol. 93, pp. 180401-4, 2004.

[124] Y. Yu, S.-L. Zhu, G. Sun, X. Wen, N. Dong, J. Chen*, et al.*, "Quantum Jumps between Macroscopic Quantum States of a Superconducting Qubit Coupled to a Microscopic Two-Level System," *Physical Review Letters,* vol. 101, pp. 157001-4, 2008.

[125] J. M. Martinis, M. H. Devoret, and J. Clarke, "Experimental tests for the quantum behavior of a macroscopic degree of freedom: The phase difference across a Josephson junction," *Physical Review B,* vol. 35, p. 4682, 1987.

[126] S.-X. Li, Y. Yu, Y. Zhang, W. Qiu, S. Han, and Z. Wang, "Quantitative study of macroscopic quantum tunneling in a dc SQUID: A system with two degrees of freedom," *Physical review letters,* vol. 89, p. 098301, 2002.

[127] S.-X. Li, W. Qiu, S. Han, Y. Wei, X. Zhu, C. Gu*, et al.*, "Observation of macroscopic quantum tunneling in a single Bi 2 Sr 2 CaCu 2 O 8+ δ surface intrinsic Josephson junction," *Physical review letters,* vol. 99, p. 037002, 2007.

[128] Y. Tian, H. Yu, H. Deng, G. Xue, D. Liu, Y. Ren*, et al.*, "A cryogen-free dilution refrigerator based Josephson qubit measurement system," *Review of Scientific Instruments,* vol. 83, p. 033907, 2012.

[129] R. Rouse, S. Han, and J. Lukens, "Observation of resonant tunneling between macroscopically distinct quantum levels," *Physical review letters,* vol. 75, p. 1614, 1995.

[130] S. S. Parkin, C. Kaiser, A. Panchula, P. M. Rice, B. Hughes, M. Samant*, et al.*, "Giant tunnelling magnetoresistance at room temperature with MgO (100) tunnel barriers," *Nature materials,* vol. 3, pp. 862-867, 2004.

[131] D. D. Djayaprawira, K. Tsunekawa, M. Nagai, H. Maehara, S. Yamagata, N. Watanabe*, et al.*, "230% room-temperature magnetoresistance in CoFeB⁄MgO⁄CoFeB magnetic tunnel junctions," *Applied Physics Letters,* vol. 86, p. 092502, 2005.

[132] S. Yuasa, A. Fukushima, H. Kubota, Y. Suzuki, and K. Ando, "Giant tunneling magnetoresistance up to 410% at room temperature in fully epitaxial Co⁄MgO⁄Co magnetic tunnel junctions with bcc Co(001) electrodes," *Applied Physics Letters,* vol. 89, p. 042505, 2006.

[133] D. Wang, C. Nordman, J. M. Daughton, Z. Qian, and J. Fink, "70% TMR at room temperature for SDT sandwich junctions with CoFeB as free and reference layers," *IEEE Transactions on Magnetics,* vol. 40, pp. 2269-2271, 2004.

[134] P. Süle, D. Kaptás, L. Bujdosó, Z. E. Horváth, A. Nakanishi, and J. Balogh, "Chemical mixing at “Al on Fe” and “Fe on Al” interfaces," *Journal of Applied Physics,* vol. 118, p. 135305, 2015.